OPTIMIZATION OF LASER POWDER BED FUSION PROCESS IN INCONEL 625 TOWARDS PRODUCTIVITY

Optimization of Laser Powder Bed Fusion Process in Inconel 625 Towards Productivity

By

MANAR NAZAR ABD KRMASHA, B.Eng., M.Eng.

A Thesis

Submitted to the School of Graduate Studies in the Partial Fulfillment of the Requirements for the Degree Master of Applied Science

McMaster University

McMaster University

Master of Applied Science, (2022)

Hamilton, Ontario (Department of Mechanical Engineering)

TITLE: Optimization of Laser Powder Bed Fusion Process in Inconel 625 Towards Productivity

AUTHOR: Manar Nazar Abd Krmasha

B.Eng. in Computer Techniques (Dijlah University Colloge)

M.Eng., Master of Mechanical Engineering (Sociesc University Centre)

SUPERVISOR: Dr. Mohamed A. Elbestawi

NUMBER OF PAGES: xix, 146

In memory of my father,

Nazar Krmasha (1954–2019)

To my family,

I owe you everything.

"Never give up on a dream just because of the

time it will take to accomplish it.

The time will pass anyway."

Earl Nightingale
(1921–1989)

Abstract

Laser Powder Bed Fusion (L-PBF) is a metal additive manufacturing technique that uses a laser beam as a heat source to melt metal powder selectively. Because of the process small layer thicknesses, laser beam diameter, and powder particle size, L-PBF allows the fabrication of novel geometries and complex internal structures with enhanced properties. However, the main disadvantages of the L-PBF process are high costs and a lengthy production time. As a result, shortening the manufacturing process while maintaining comparable properties is exceptionally beneficial.

Inconel 625 (IN625) is a nickel-based superalloy becoming increasingly popular in marine, petroleum, nuclear, and aerospace applications. However, the properties of IN625 parts produced by casting or forging are challenging to control due to their low thermal conductivity, high strength and work hardening rate, and high chemical complexity. Furthermore, IN625 alloy is regarded as a difficult-to-machine material. As a result, it is worthwhile to seek new technologies to manufacture complex-shaped IN625 parts with high dimensional accuracy. IN625 alloy is known for its excellent weldability and high resistance to hot cracking; thus, IN625 alloy appears to be a promising candidate for additive manufacturing.

This thesis presents an experimentally focused study on optimizing L-PBF processing parameters in IN625 superalloy to increase process productivity while maintaining high material density and hardness. This study had four stages: preliminary, exploratory, modelling, and optimization. The first stage was devoted to conducting a literature review and determining the initial processing parameters.

The second stage concentrated on determining the process window, for which single tracks were printed with two high levels of laser power (300, 400 W), five levels of scan speed (500, 700, 900, 1100, 1300 mm/s), and five levels of powder layer thickness (30, 60, 90, 120, 150 μm). Then, the process window was defined after investigating the top views and cross-sections of the tracks. Stage 3 involved printing 48 cubes ($10 \times 10 \times 10$ mm^3) with a laser power of 400 W, scan speeds of (700, 900, 1100, 1300 m/s), layer thicknesses of (60, 90, 120, 150 μm), and overlap percentages of (10, 30, 50%). As a result, the density of cubes was measured, and a statistical multiple regression analysis was used to predict it. Stage 4 involved estimating four sets of ideal processing parameters (based on statistical modelling of relative density) and printing 24 cubes ($10 \times 10 \times 10$ mm^3), six samples for each set. Finally, the relative density, hardness, and productivity of the samples were assessed, and a trade-off was determined.

Even with the thickest powder layer of 150 μm (highest process productivity), samples with a mean relative density greater than 99% (i.e., 99.31% by Archimedes principle and 99.82% by image analysis) were printed. These findings are consistent with previously published results for L-PBF IN625 samples manufactured with smaller layer thicknesses ranging from 20 to 40 μm while maintaining comparable material hardness. The findings of this study are noteworthy because IN625 parts can be printed with higher powder layer thicknesses (less production time) while retaining similar material properties to those published with typical layer thicknesses ranging from 20 to 40 μm. Reduced production time due to optimized processing parameters can lead to significant energy and cost savings.

Acknowledgements

First and foremost, I would like to express my deepest gratitude to my advisor, Dr. Mohamed Elbestawi, for his continuous support, advice, encouragement, and helpful suggestions and counsel. I would also like to thank the members of the additive manufacturing group (AMG), Mechanical Engineering, McMaster University for their cooperation, insightful conversations, and productive group meetings.

Our Brazilian collaborators from SENAI Innovation Institute in Manufacturing Systems and Laser Processing, Dr. Luís Gonzaga Trabasso, Dr. Alexandre Cunha, MSc Henrique R. Oliveira, and MSc Marcos V. Bento, deserve our deepest gratitude for their fruitful collaboration that greatly aided the research.

Last but not least, I would like to express my heartfelt gratitude to my family, who unconditionally support me in everything I do with their love, guidance, motivation, and unending encouragement; they are the ultimate role models. I owe a debt of gratitude to my son, Joud, for being the first and best incentive in my life. My heartfelt thanks go to my husband, Dr. Kassim S. Al-Rubaie, who has always been by my side, no matter how dubious my decisions have been, and who consistently shows me warmth and affection in any situation.

Manar Nazar Abd Krmasha

April 14, 2022

Contents

List of Figures

List of Tables

Chapter 1

INTRODUCTION

1.1 Background

Nickel-based superalloys are increasingly being used in marine, petroleum, nuclear, and aerospace applications due to their high mechanical strength at elevated temperatures, outstanding hot corrosion and oxidation resistance, excellent weldability, and high creep and fatigue resistance [1–5]. For example, Figure 1.1 [6] depicts the materials employed in the main components of a modern jet engine, in which nickel-based superalloys cover 47% of the total weight. These alloys are used in components that operate above 550 °C, such as turbine blades, discs, vanes, and combustion chamber.

Inconel 625 (IN625) is a nickel-based superalloy consisting of about 62 wt.% nickel and 23 wt.% chromium, solid-solution strengthened by its contents of molybdenum (8–10 wt.%) and niobium (3.15–4.15 wt.%) in a nickel-chromium matrix. Chromium

gives the alloy its excellent corrosion resistance by forming a passive thin layer of Cr_2O_3; whereas, molybdenum and niobium strengthen it [1, 4, 7] .

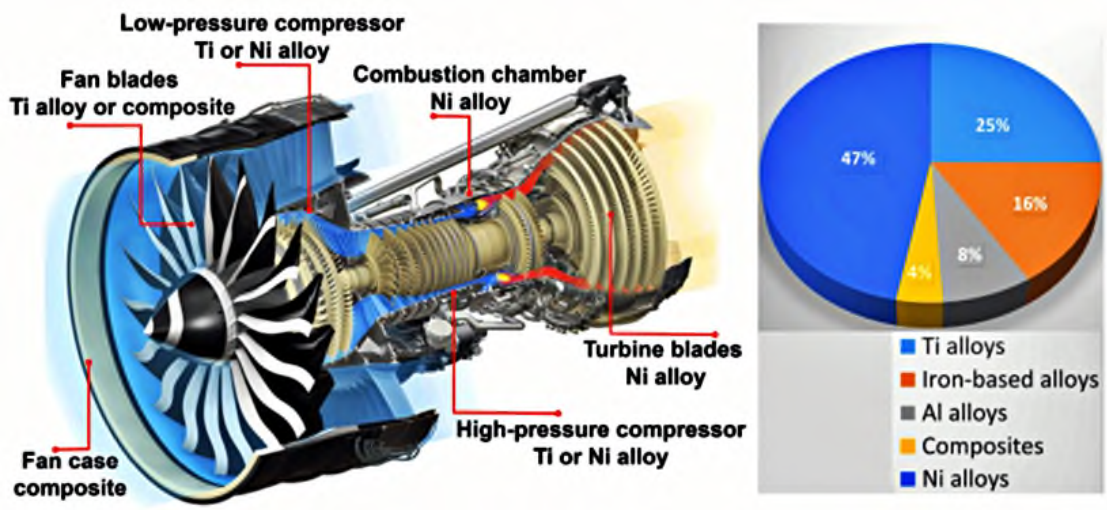

FIGURE 1.1: Materials used in the GE CF6 turbine engine of Boeing 787 aircraft [6].

However, the properties of IN625 parts produced by casting or forging are difficult to control due to their low thermal conductivity, high strength, high work hardening rate, and high chemical complexity. Furthermore, IN625 alloy is regarded as a difficult-to-machine material, resulting in extensive tool wear [8–10]. Therefore, it is worthwhile to seek out new technologies for producing complex-shaped IN625 with high dimensional accuracy. Nevertheless, it is well known that IN625 has excellent weldability [11, 12] and high resistance to hot cracking; thus, IN625 alloy appears to be a promising candidate for additive manufacturing [13–16].

Additive manufacturing (AM) is defined by the American Society for Testing and Materials (ASTM) as "a process of combining materials to produce items from 3D model data, usually layer by layer, as opposed to subtractive approaches" [17]. AM is a cutting-edge technology that opens up new avenues for creating unique shapes

and complex interior structures with enhanced properties. It differs from traditional manufacturing methods in that material is added rather than subtracted to form the desired solid shape. Furthermore, AM provides a variety of manufacturing techniques that are increasingly being used across a wide range of industries, including automotive, aerospace, and biomedical, as seen in Figure 1.2 [18].

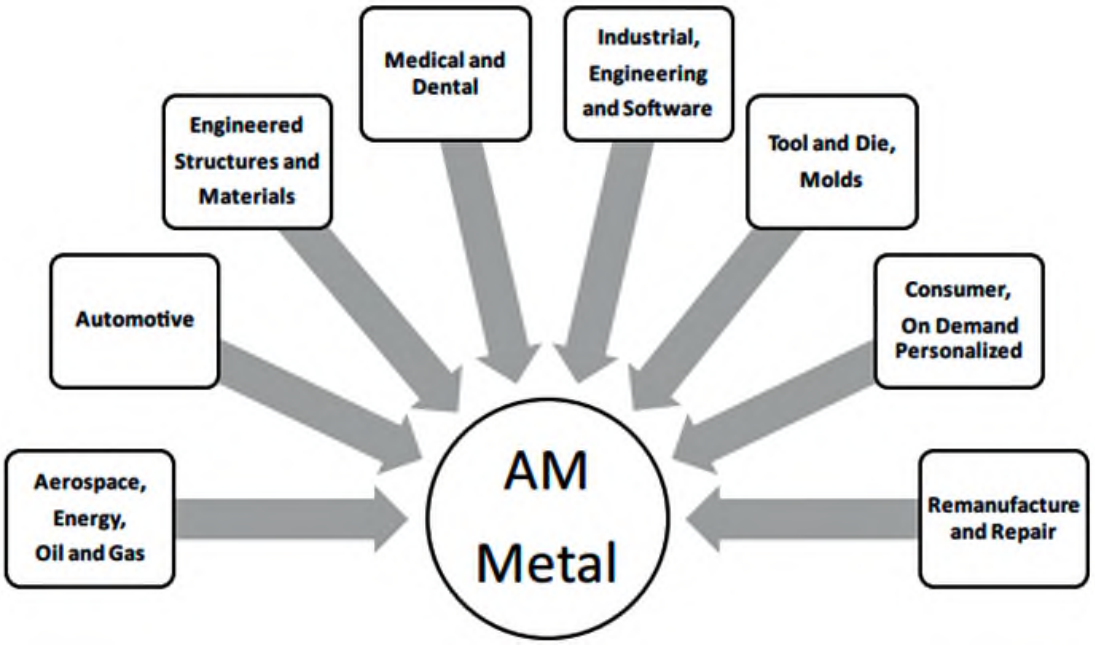

FIGURE 1.2: Applications of metal AM [18].

The stepwise nature of AM reduces complex 3D geometries into more straightforward two-dimensional manufacturing steps, enabling the fabrication of complex hollow structures, overhangs, and lattice structures that would be impossible to manufacture using traditional processes [19]. Because AM costs are primarily determined by the volume to be built and are not affected by component topology, it can help lower the prices of parts with complex geometry. As a result, additive manufacturing is essential for producing highly complex parts made of

expensive materials that require extensive machining. However, costs of traditional manufacturing techniques are primarily determined by the part's complexity.

One advantage of using AM is that it has a higher material conversion efficiency (reducing material waste). The material conversion efficiency may be expressed by the buy-to-fly ratio, which is calculated as the mass of the initially purchased stock material divided by the mass of the final finished part. For example, AM shows a buy-to-fly ratio of 1.5–2:1, whereas machined parts have a ratio of 15–20:1 [20–22].

In this context, ArianeGroup [23] has successfully manufactured a new injector head of a rocket engine of a future upper stage propulsion module from the IN718 superalloy, using the EOS laser powder bed industrial 3D printing technology, as shown in Figure 1.3 [23].

FIGURE 1.3: Injector head of a rocket engine printed from IN718 superalloy using EOS laser powder bed fusion technology [23].

The original injector head was created through a variety of manufacturing processes, including casting, brazing, welding, and drilling. This time-consuming and complex manufacturing process can result in weak points that pose risks under extreme loads. Instead of 248 elements produced by traditional methods, the new injector head is only one part, thus significantly reducing the production time, as shown in Table 1.1 [23].

TABLE 1.1: Production time comparison of traditional and 3D printing used for manufacturing the injector head of a rocket engine [23].

Production process	**Construction time for 1 injector head**
Casting and machining finishing	3 months
EOS M 400 (1 laser for 1 component)	65 h
EOS M 400-4 (4 laser for 1 component)	35 h

Among the many different AM manufacturing techniques, the most popular and mature Metal Additive Manufacturing (MAM) techniques are based on the Powder Bed Fusion (PBF) manufacturing processes [19], which are widely available commercially. These methods are distinguished by the use of a powder bed layer that is repeatedly exposed to a high-density thermal flux, causing powder particles to sinter or totally melt, and then fuse into a consolidated structure upon cooling. Laser Powder Bed Fusion (L-PBF) is one of the most widely used PBF technologies for selectively processing powder using a laser beam as a heat source to totally melt it [19, 24].

Using the L-PBF process, parts are produced layer-by-layer from CAD models according to the desired shapes. During the deposition process, each layer is created by melting separate passes from a powder feedstock, which is rapidly heated, melted,

solidified, and cooled. L-PBF allows for the fabrication of innovative geometries and complicated internal structures with improved properties due to small layer thicknesses, laser beam diameter, and powder particle size [19].

It is worth noting that the cost of a product is frequently determined by the AM build accuracy and production rate, and there is always a trade-off between the two. For example, L-PBF parts have better dimensional precision than Wire Arc Additive Manufacturing (WAAM) parts, but the L-PBF process has a slower production rate than WAAM [16].

L-PBF is a very complex process in which over 100 parameters can influence part manufacturing [19]. The most critical parameters are the laser power P (W), scan speed v (mm/s), powder bed layer thickness t (μm), hatch distance h (μm), laser spot size d (μm), powder characteristics, substrate preheating temperature, and scanning strategy. These parameters are directly related to how the layers are built up and are usually varied and optimized to produce crack-free, dense parts.

Laser power, scanning speed, hatch spacing, and layer thickness are frequently integrated into a single parameter called volumetric energy density VED (J/mm^3) [25]. As shown in Figure 1.4 [26], an accurate value of VED may be obtained using various combinations of P, v, h, and t, with some values of scan speed (v) unable to create adequate melt. As a result, producing parts with optimal properties requires a thorough understanding of the L-PBF processing parameters and how they interact.

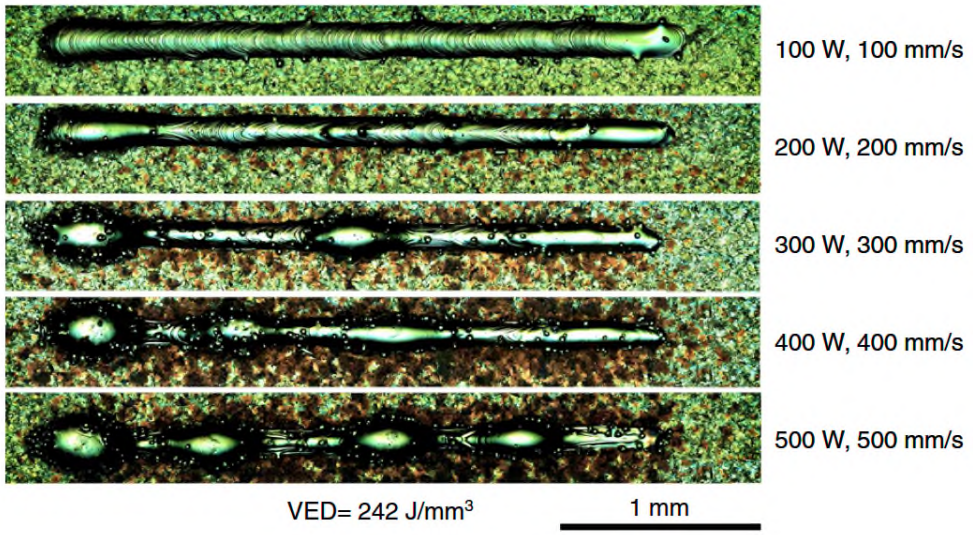

FIGURE 1.4: Single tracks of 316L SS printed with L-PBF process using the same VED value of 242 J/mm^3 but with increasing both laser power and scan speed. Laser spot size = 55 μm, and layer thickness = 75 μm [26].

1.2 Identifying Issues

With the advancement of various Metal Additive Manufacturing (MAM) techniques, interest in the L-PBF process has grown due to the improved properties of the parts compared to those manufactured by other methods, particularly for small sizes. As a result, several studies have been conducted to better understand process parameters optimization for advanced materials, which are primarily used in the aerospace, automotive, and biomedical industries [13, 27–31].

Because of its exceptional properties, IN625 alloy is widely used in the marine, petroleum, nuclear, and aerospace industries. A literature review on the optimal processing parameters for manufacturing IN625 by L-PBF, shown in Table 2.1, Chapter 2, revealed that the powder layer thickness investigated ranged from 20 μm to 60 μm. Furthermore, no systematic study on the effects of increasing the powder

layer thickness on the density and productivity of L-PBF IN625 parts at higher laser powers of 300 and 400 W was found. The main drawbacks of the L-PBF process, on the other hand, are high costs and a lengthy production time. As a result, reducing the manufacturing process while maintaining similar properties is extremely advantageous.

Changing only the powder layer thickness in the volumetric energy density formula, Equation 2.1, Chapter 2, may not result in a dense part because the heat input provided to the powder bed may not be sufficient to melt the powder completely. The input energy, on the other hand, is controlled by adjusting other process parameters such as laser power, scan speed, and hatch distance. Thus, the optimal parameters should be developed empirically to produce crack-free, dense parts with improved material properties.

Therefore, in this study, two high levels of laser power (300 and 400 W); five levels of scan speed (500, 700, 900, 1100, and 1300 mm/s); and five levels of powder layer thickness (30, 60, 90, 120, and 150 μm) were used for printing single tracks to define the process window. Furthermore, a laser power of 400 W; scan speeds of 700, 900, 1100, and 1300 mm/s; powder layer thicknesses of 60, 90, 120, and 150 μm; and overlap percentages of 10, 30, and 50% were used for printing the cubes. Relative density of the cubes was evaluated and modelled in terms of scan speed, layer thickness, and overlapping. Based on the statistical modelling, the optimal parameters were estimated, with which additional cubes were printed. Then, relative density, hardness, microstructure, and productivity were evaluated and the optimal processing parameters for increasing productivity while maintaining comparable physical and mechanical properties were established.

1.3 Aim and Objectives

The goal of this research was to optimize the L-PBF processing parameters in IN625, focusing on the effects of increasing powder layer thickness on production rate while maintaining comparable physical and mechanical properties. To achieve the research goal, the following steps were planned:

1. Printing single tracks using the following processing parameters:
   - Laser power: 300 and 400 W.
   - Scan speed: 500, 700, 900, 1100, and 1300 mm/s.
   - Powder layer thickness: 30, 60, 90, 120, and 150 μm.

   The majority of these parameters used were not investigated; thus, this study significantly contributes to the literature of L-PBF IN625 superalloy.

2. Evaluating the top views and cross-sections of the tracks to define the process windows, and estimating the processing parameters for printing the samples.

3. Printing $10 \times 10 \times 10$ mm^3 cubes with:
   - Laser power: 400 W.
   - Scan speed: 700, 900, 1100, and 1300 mm/s.
   - Powder layer thickness: 60, 90, 120, and 150 μm.
   - Overlap: 10, 30, and 50%.

4. Measuring and modelling the cubes density in terms of scan speed, layer thickness, and overlapping to define four new sets of processing parameters.

5. Printing additional IN625 cubes with the new sets of processing parameters and evaluating the relative density, hardness, microstructure, and productivity of the printed cubes.

6. Establishing a trade-off between relative density, hardness and productivity.

1.4 Main Contribution

This study investigated the effects of a wide range of processing parameters on the relative density, hardness, and productivity. It was shown that the samples printed with the greatest powder layer thickness of 150 μm had comparable physical and mechanical properties to those printed using typical powder layer thicknesses of 20–40 μm . Furthermore, because of the optimized processing parameters, the productivity in this work is between 2.58 and 8.08 times higher than that published in the literature.

Given the low productivity of L-PBF compared to other AM techniques, the findings of this study are significant because IN625 parts can be printed with higher layer thicknesses while retaining material properties comparable to those printed with typical thin powder layer thicknesses of 20–40 μm. Reduced production time due to optimized processing parameters can result in substantial energy and cost savings.

1.5 Thesis Structure

This thesis is divided into five chapters and includes a list of references used for the writing of the thesis:

- **Chapter 1, Introduction**

  The current one, it provides an overview of nickel-based superalloys, the L-PBF technique, as well as the motivations and objectives driving this research.

- **Chapter 2, Literature Review**

  It explains additive manufacturing, metal additive manufacturing, laser-based additive manufacturing, and the L-PBF process and its parameters. It also includes a literature review on the effects of L-PBF processing parameters such as laser power, scan speed, hatch distance, powder layer thickness, powder characteristics, and scanning strategy on the quality of printed parts. The L-PBF processing parameters for printing IN625 found in the literature are summarized and presented in Table 2.1. Furthermore, the L-PBF common defects and their mechanisms are explained. An overview of superalloys, nickel-based superalloys including IN625, and the microstructure and hardness of IN625 produced by L-PBF, are provided. Finally, the literature-based L-PBF processing parameters, as well as related relative density and hardness, are summarized and provided in Table 2.8.

- **Chapter 3, Materials and Methods**

  It explains the powder properties and printing parameters used for single

tracks and cubes. Furthermore, the equipment and procedures for evaluating single tracks, cubes, density, hardness, and microstructure are described.

- **Chapter 4, Results and Discussions**

  It presents and discusses the obtained results. It begins with a characterization of single tracks (top view and cross-section) to define the process window from which the estimated best processing parameters for printing the cubes can be discovered. The effect of scan speed on melt pool width is explained for varying powder layer thicknesses. The melt pool modes are discussed regarding the amount of laser energy delivered to the powder. Statistical analysis is performed to show the most significant processing parameter influencing the melt pool width. An empirical statistical model is proposed to describe the combined effect of scan speed and layer thickness on melt pool width. A nonlinear regression model relating melt pool width to surface energy density is also presented. 3D surface and contour plots are displayed to show the effects of processing parameters such as scan speed, layer thickness, overlap, and surface energy on the density of printed IN625 cubes. The effects of processing parameters on the relative density, hardness, and microstructure of printed cubes are discussed. Finally, a trade-off is established between density, hardness, and productivity.

- **Chapter 5, Conclusions and Future Work**

  It concludes the thesis and proposes some issues for future work in the field.

Chapter 2

LITERATURE REVIEW

2.1 Additive Manufacturing

Additive Manufacturing (AM) is a cutting-edge, innovative technology that allows for the creation of novel shapes and complex interior structures with improved properties. The correct AM technology combined with the right post-processing approach can result in significant savings by lowering overall weight, material waste, lead-time, energy, and cost.

In this regard, Tomlin and Myer [32] from EADS Innovations works presented a study on the benefits of AM technology for an Airbus A320 nacelle hinge bracket component using the Arcam Electron Beam Selective Melting (EBSM) process, incorporating the topology optimization method for design. The original nacelle bracket is constructed of HC101 steel, which was cast in a near-net-shape and then machined to tolerance. The steel employed has a density of 7.7 g/cm^3, while

the suggested new material (Ti6Al4V) has a density of 4.42 g/cm^3. Therefore, weight savings can be expected just by changing the density of the material [32]. The optimized new component weighed only 326 g, compared to 920 g for the original one, as illustrated in Figure 2.1 (a), thus giving a 64% reduction in weight. Furthermore, stress analysis in Figure 2.1 (b) revealed substantially more efficient material use in the optimized part.

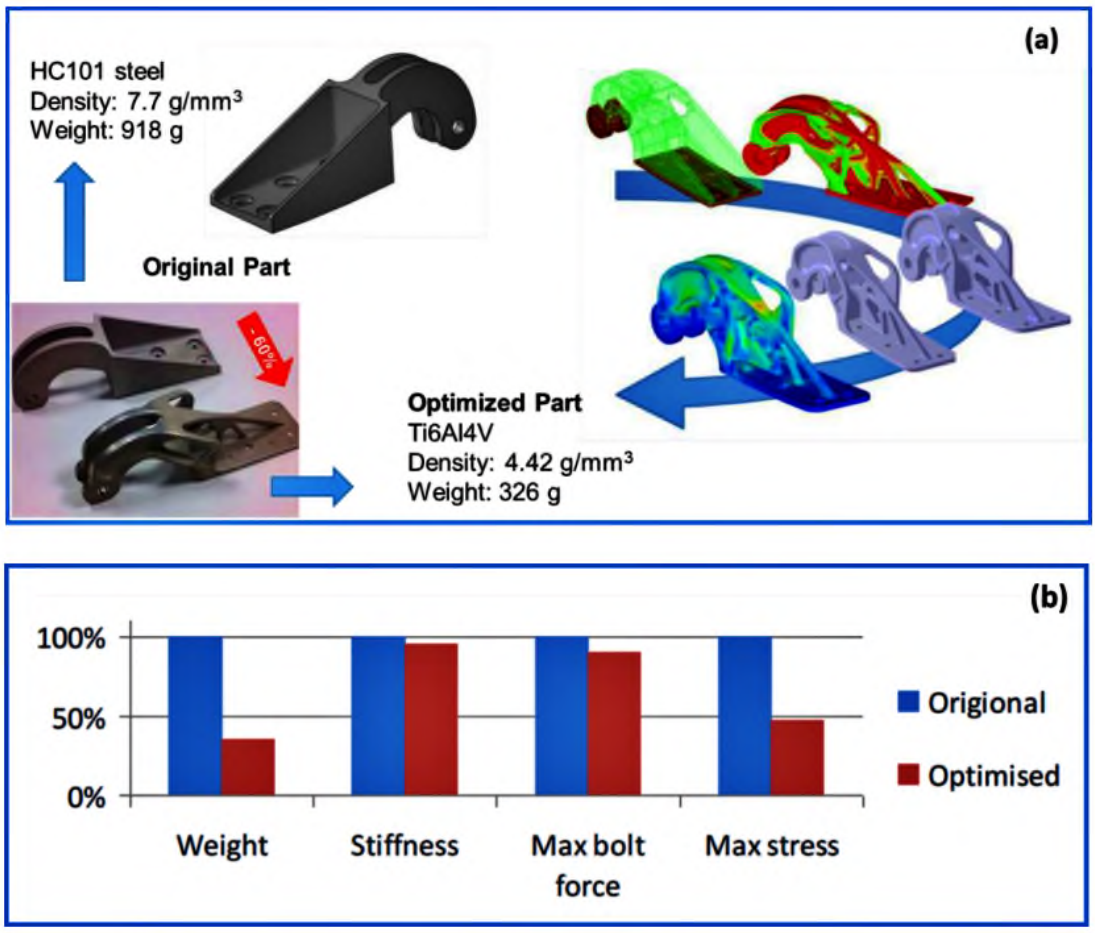

FIGURE 2.1: Airbus A320 nacelle hinge bracket component, (a) original part and optimized Ti6Al4V design for AM manufacturing, (b) performance comparison of the original cast and machined HC101 steel to the new designed Ti6Al4V with AM [32].

Additive manufacturing is being used on a variety of materials, including polymers, ceramics, and metals [33]. There is a growing demand in using AM techniques to manufacture high-performance metallic materials for aerospace, automotive, and medical applications [34–37]. That is owing to higher freedom in complex design, higher customization, and better material utilization offered by AM when compared to traditional manufacturing processes [19, 38].

Additive manufacturing (AM), a layer-wise manufacturing technology that uses a CAD model and raw material as input, involves connecting a computer to AM machine that performs a series of operations to create the desired object. AM includes a series of steps from a virtual CAD model to a physical part. Slicing a 3D CAD model into numerous layers (STL file), generating a tool path for each layer, transferring the data to the AM machine, and building the component up layer by layer from the sliced model are the foundations of all AM operations. As a result, AM technology opens up new possibilities for creating novel geometries and complex interior structures [19, 38–40].

2.2 Metal Additive Manufacturing (MAM)

Metals have become increasingly popular in additive manufacturing. It is now possible to create high-quality components with complex structures owing to the rapid developments in AM machines, lasers, and powders. MAM systems are primarily classified by the heat source used (laser or electron beam), the feedstock used (wire or powder), the feedstock delivery method, and the dimension and quality of the component produced [40]. Powder bed fusion (PBF) is a type of fusion in which the heat source can be a laser (L-PBF) or an electron beam

(PBF-EB or EBM). Directed energy deposition (DED) is another category that can use a number of heat sources, including laser (DED-L), electron beam (DED-EB), and plasma arc (PA-DED) [18, 40]. Different MAM systems are illustrated in Figure 2.2 [41].

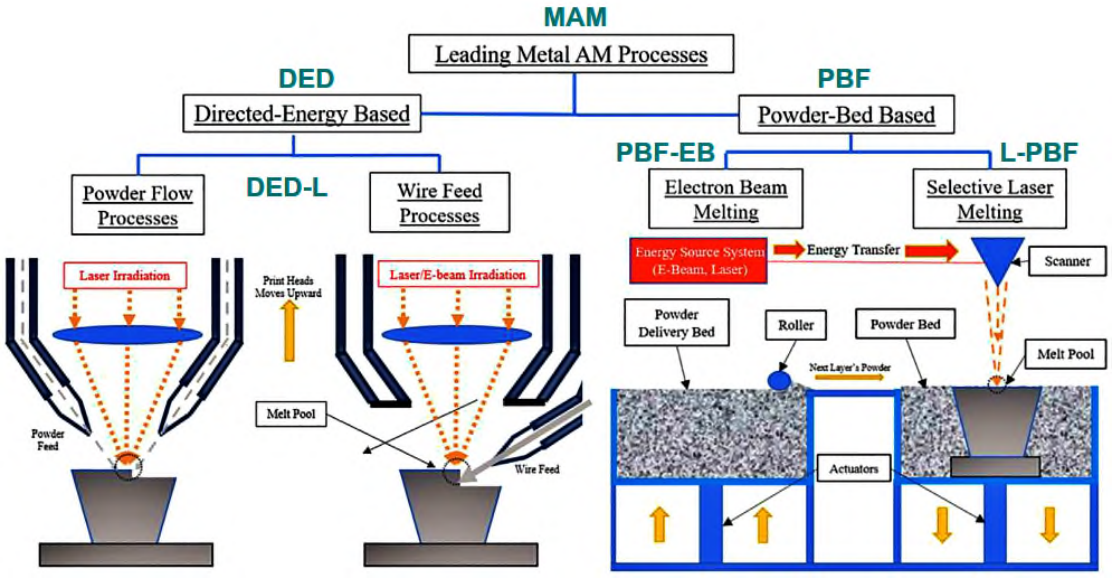

FIGURE 2.2: Schematic illustration of different MAM systems, adapted from [41].

2.3 Laser-Based AM Processes

A brief overview of Laser-based Additive Manufacturing (LAM) techniques is offered due to the topic importance. Despite the fact that LAM processes have the same material additive manufacturing (AM) concept, each LAM process has its own set of features in terms of materials that may be used, processing procedures, and environments in which they can be used. The ability of various LAM techniques to produce high-performance metallic components with tunable microstructural and mechanical properties also differs significantly.

LAM can be classified into three basic processes based on the different mechanisms of laser-powder interaction (*pre-spreading of powder in powder bed before laser scanning vs. coaxial feeding of powder by the nozzle with synchronous laser scanning*) and the different metallurgical mechanisms (partial melting vs. complete melting). Figure 2.3 [42] shows the three basic processes: laser sintering (LS), laser melting (LM), and laser metal deposition (LMD).

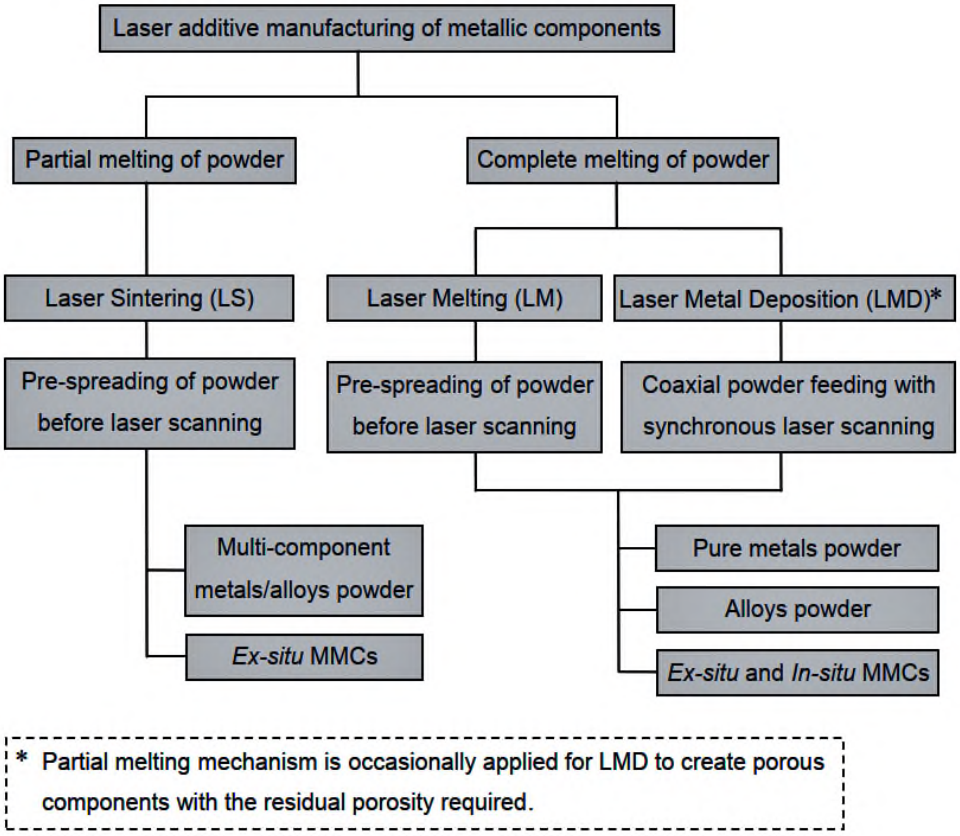

FIGURE 2.3: Classification of laser AM processes based on different mechanisms of laser-material interaction [42].

Despite the advantages of AM for producing near-net-shape components, the inherent features of AM pose significant obstacles. In MAM parts, for example, poor surface finish (i.e., uneven and rough surface profile) and inaccurate

dimensional tolerances require post-processing processes for end-use components. Hybrid additive manufacturing is based on this assumption. To attain the appropriate surface finish, dimensional tolerances, and material properties, a metal part is initially near-net manufactured using AM and then post-processed using traditional manufacturing methods such as machining, grinding, and so on.

2.4 L-PBF Process Technique

The L-PBF technique is one of the most widely utilized MAM technologies in the world. L-PBF technology has emerged as a strong alternative for producing critical components in the aerospace, energy, chemical, and biomedical industries, among others. Figure 2.4 shows how the L-PBF technique can be used to make a component 2.4 [43].

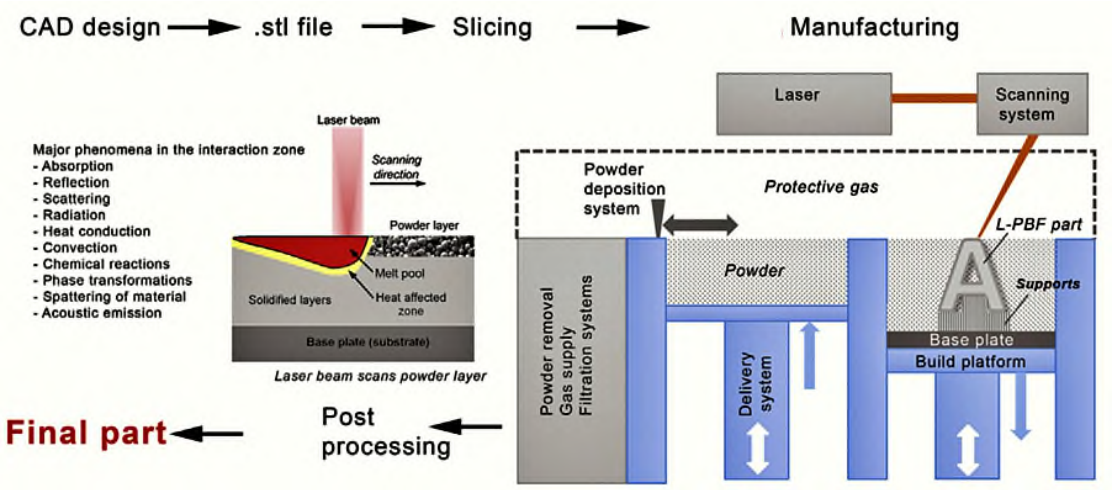

FIGURE 2.4: Schematic presentation of L-PBF process [43].

It consists of three phases that are repeated until the solid part is complete. These are as follows:

1. A bed of spherical metal powder is spread on the working platform by roller or racking mechanisms. The build platform is housed within the chamber of AM machine. During processing, it is shielded by a continuous flow of inert gas (argon or nitrogen) to prevent melt pool oxidation and aid in the removal of generated metal vapour.

2. When the powder is evenly distributed, a guided laser beam completely melts it at predefined locations to slices of a corresponding three-dimensional (3D) computer-aided design (CAD) model and fuses it to the layer below.

3. Finally, after the laser beam has scanned all of the locations, the build platform descends one layer thickness, and the process is repeated to finish printing the part.

2.5 L-PBF Processing Parameters

There are about 100 variables that might affect the L-PBF process [28]. These are laser, scan, powder, and temperature related, as shown in Figure 2.5 [19]. The most critical parameters are: laser power P (W), scan speed v (mm/s), powder bed layer thickness t (μm), hatch distance h (μm), laser spot size d (μm), powder characteristics, substrate preheating temperature, and scanning strategy. Laser power, scan speed, hatch distance, and powder bed layer thickness are frequently combined and reported as a single parameter called volumetric energy density VED, as shown in Equation 2.1 [25]. These processing parameters mostly govern the amount of heat applied to the powder bed.

$$VED = \frac{P}{v \times h \times t} \tag{2.1}$$

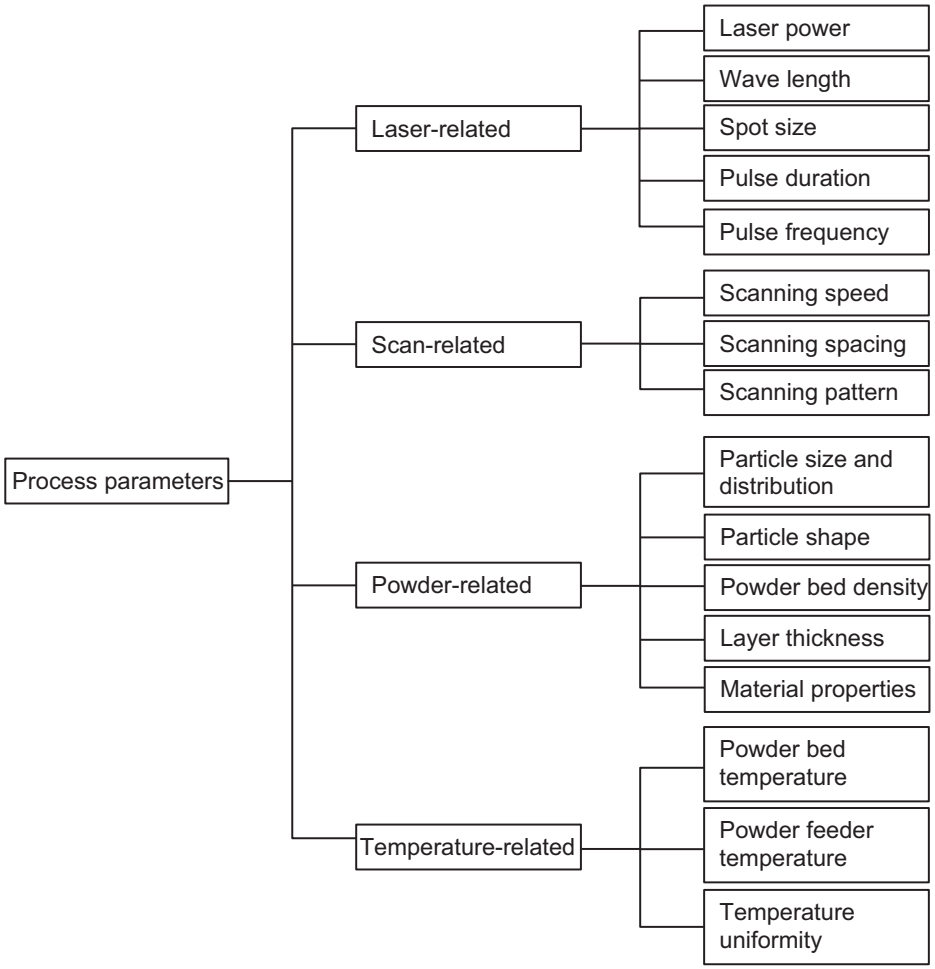

FIGURE 2.5: Principal L-PBF processing parameters [19].

Energy density can only be used as a rough guideline to calculate the energy transferred to the powder bed. It is frequently used to compare parts produced by different deposition parameters. However, it does not reveal the complex physics of the melt pool or identify the optimum energy that leads to fully dense parts [26].

For example, the same value of VED can be determined by varying P, v, h, and t, where some v values can not produce appropriate melt, as seen in Figure 1.4 [26], Chapter 1. Therefore, producing parts with optimal properties requires a thorough understanding of L-PBF process parameters and their interactions.

In addition to volumetric energy density, linear energy density E_L and surface energy density E_S can be calculated as follows [19]:

$$E_L = \frac{P}{v} \tag{2.2}$$

$$E_S = \frac{P}{v \times t} \tag{2.3}$$

or

$$E_S = \frac{P}{v \times h} \tag{2.4}$$

2.5.1 Laser Power

The main parameter is laser power, which is primarily determined by the processed materials. For example, the laser power required to process polymer is approximately 5 W, whereas ceramic requires 500 W. Lowering the laser beam spot size at a given laser power results in a higher energy input for the powder bed. Other processing parameters can be adjusted using laser power and beam characteristics. Scan speed, for example, is limited by the amount of laser power available; increasing laser power can improve scan speed. Hatch distance is limited by the laser beam spot size [19, 24, 44]. Layer thickness is limited by the ability of laser beam to penetrate the powder bed [19, 24, 44].

When the hatch distance and powder layer thickness remain constant, increasing the laser power and decreasing the scan speed can result in a high *VED*. A laser beam wit high *VED* can generate a melt pool with a high surface temperature, which improves wettability by lowering viscosity and surface tension [45]. Increasing the laser power to a certain level tends to increase the relative density of L-PBF parts and improve their mechanical properties. However, exceeding that level of laser power would degrade the properties of the parts [6].

Li et al. [46] used L-PBF with gas atomized 316L stainless steel powder to print single tracks at a constant scan speed of 200 mm/s and varied laser power values. The track breaks apart into smaller melt droplets, referred to as balling, at a laser power of 70 W, as seen in Figure 2.6. The track becomes discontinuous and balling begins to disappear when the laser power is increased to 110 W. With a laser power of 150 W, the track looks to be almost continuous. The track becomes consistent and completely continuous as the laser power is increased to 190 W. Continuous tracks appear to emerge when the laser power is increased. Only continuous tracks are desirable for printing L-PBF parts since they result in fully dense parts. The high laser power can provide enough input energy to promote wettability and further spread the molten pool. As a result, it shows that balling can be prevented by slowing down the scan speed or raising the laser power to provide enough energy to completely melt the powder [26, 46, 47].

2.5.2 Scan Speed

The scan speed at which the laser beam passes across the powder bed is another critical processing parameter. It displays the length of time the laser beam is in

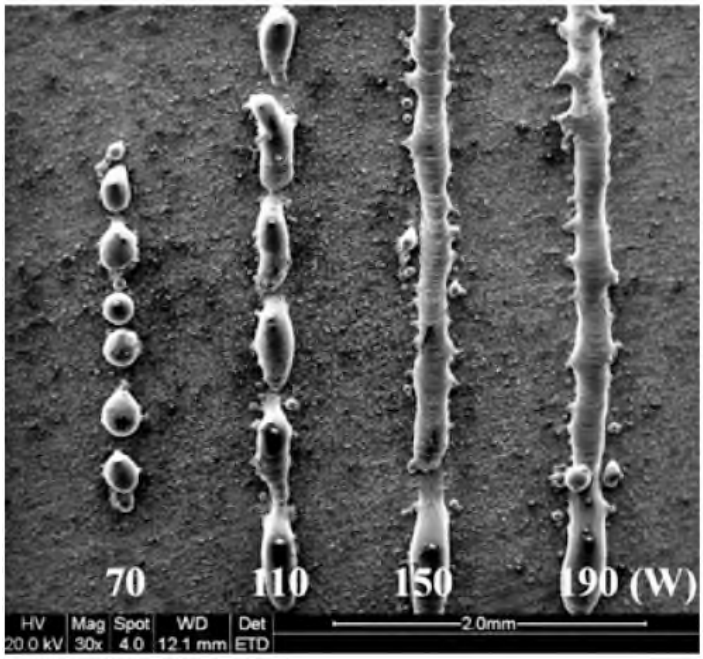

FIGURE 2.6: Single tracks of 316L SS printed with L-PBF process using the same scan speed of 200 mm/s and varying values of laser power from 70 to 190 W [46].

contact with the powder bed. Several research have been conducted to investigate the effect of scan speed on track quality and to establish the ideal conditions for effective fabrication [26, 46, 47]. Slow scan speeds give the laser more time to interact with the powder. Due to the laser concentration in a fixed location for an extended period of time if the speed is too slow, significant heating may emerge. Evaporation and material loss will occur as a result. However, if the scan speed is too fast, there will be minimal interaction between the laser beam and the powder bed, resulting in insufficient melting.

Bertoli et al. [26] investigated the effect of scan speed on the shape of L-PBF 316L stainless steel tracks. As shown in Figure 2.7, they printed the tracks at a constant laser power of 100 W and a layer thickness of 75 μm while varying the scan speed from 100 to 500 mm/s. Figure 2.7 (a) depicts a smooth, continuous

track at a suitable high *VED* level (low scan speed). At lower *VED* (high scan speed), the track is uneven, non-homogeneous, and has an irregular shape, as shown in Figure 2.7 (b). Finally, when the *VED* is too low (excessively high scan speed), the track breaks apart into smaller melt droplets, known as balling, as shown in Figure 2.7 (c).

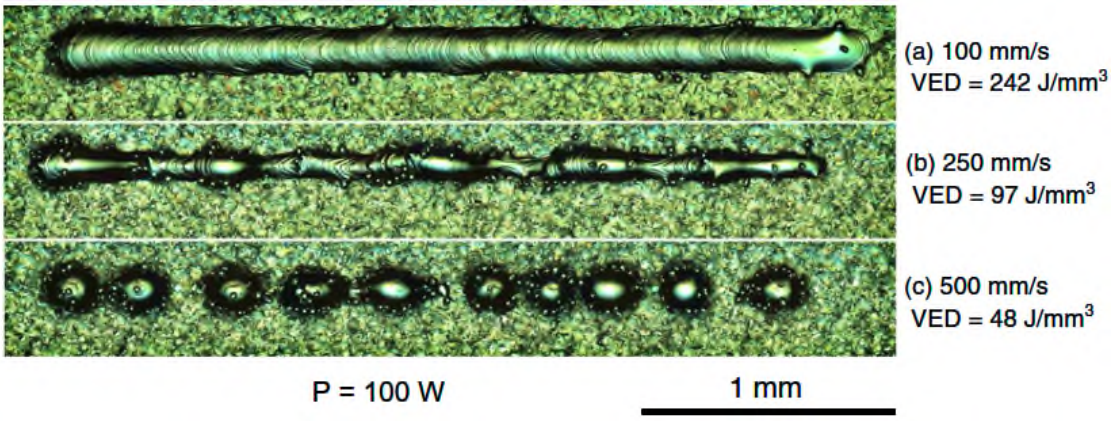

FIGURE 2.7: Single tracks of 316L SS printed with L-PBF process using the same laser power of 100 W and scan speeds from 100 to 500 mm/s, laser spot size of 55 μm and layer thickness of 75 μm [26].

2.5.3 Hatch Distance

Hatch distance (h) is the distance between the centres of two adjacent laser tracks, as shown in Figure 2.8 [48]. It determines the rate at which laser tracks overlap. The smaller the h, the more consecutive tracks overlap, signifying complete powder melting and homogeneous heat distribution. Overheating and evaporation of the molten material can occur if h is too small. A large h, on the other hand, causes significant offsetting between melt tracks, resulting in insufficient powder melting (lack-of-fusion). As shown in Figure 2.9 [49], hatch distance can affect the relative density of the parts.

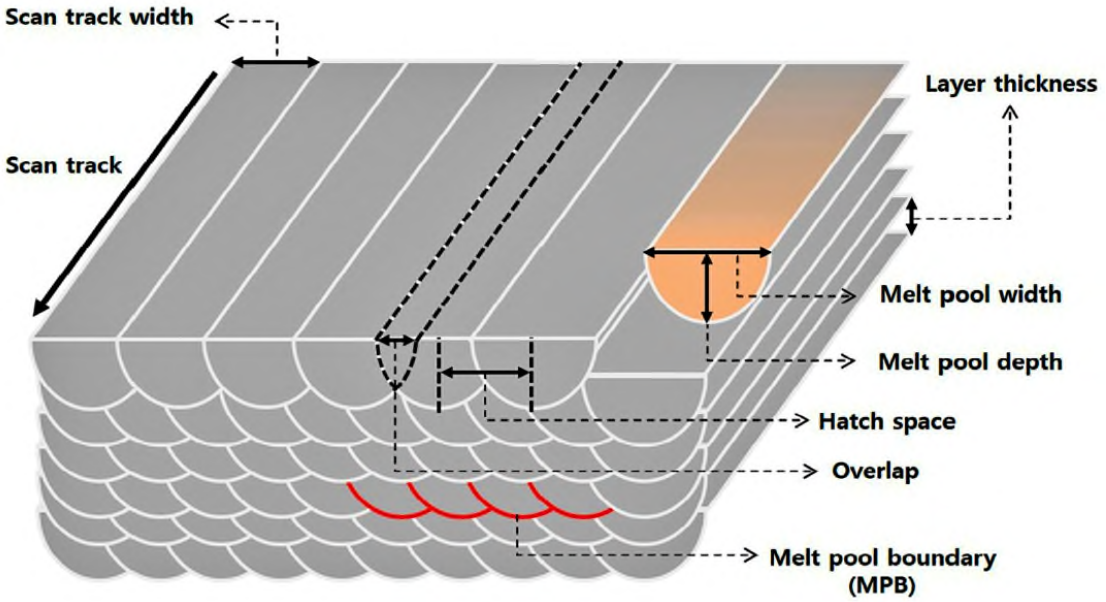

FIGURE 2.8: Terminology of L-PBF processing parameters [48].

Insufficient melt pool overlap is expected as a result of the increased hatch distance from 100 μm to 140 μm, resulting in poor bonding between adjacent scan tracks and hence lowering the relative density of printed parts (Figure 2.9). Furthermore, a hatch spacing of 130 μm may produce a relative density of roughly 99.5% for the lowest laser power and scan speed combination of 200 W and 500 mm/s. The VED of this combination is 61.5 J/mm^3, whereas the other two are 55 and 51 J/mm^3, respectively. The 500 mm/s speed allows the laser to scan the powder layer in sufficient time, resulting in improved melting and bonding. However, if a higher production rate is needed, the third combination of 300 W and 900 mm/s with a hatch distance of 120 μm is recommended. The suggested case results in a 66% improvement in production rate when compared to the first combination with a hatch distance of 130 μm.

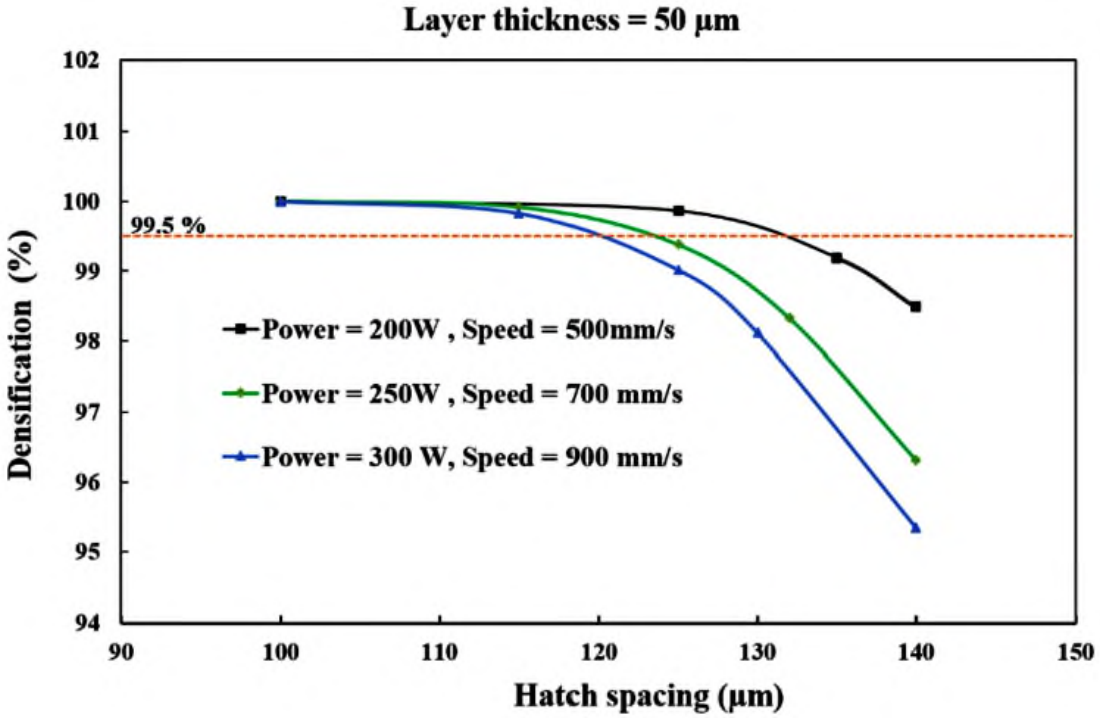

FIGURE 2.9: Effect of hatch distance on the relative density of L-PBF 316L stainless steel for various power-speed combinations [49].

According to Zhou et al. [50], a small hatch distance of 80 μm could result in a high volume energy density, causing vaporization and bubbles formation. Once the bubbles are confined within the molten pools, pores can form. A small hatch distance also leads to a large overlapping area, resulting in a rough surface. This makes powder spreading and subsequent printing difficult. As a result, additional pores may be formed. Massive irregular pores can be seen when a large hatch distance of 200 μm is used. Because of the lack of fusion, the pores may form in the gaps between adjacent melt tracks. Due to the high viscosity of the molten pool as a result of the low volumetric energy density *(VED)*, filling these gaps is challenging. These pores, in turn, deteriorate the relative density of the printed parts.

2.5.4 Powder Layer Thickness

The layer thickness of a printed part is the height of successive layers, as seen in Figure 2.8. It is usually determined by the powder particle size distribution and other process parameters like laser power. A thin layer may not be able to accommodate powder particles of various sizes, resulting in uneven powder distribution. A thick layer of powder, on the other hand, may result in bigger voids within the particles or lack-of-fusion porosity. Processing thick layers necessitates a large amount of heat input, whereas processing thin layers necessitates a little amount. A thin layer forms with small powder particle sizes. Thin layers are also required for dense parts with superior surface quality. Using thin layers, on the other hand, increases the production time.

Kempen et al. [51] evaluated the effect of increasing layer thickness on relative density and hardness of 18Ni-300 maraging steel parts manufactured by L-PBF. As the layer thickness grows from 30 μm to 60 μm, both relative density and hardness are claimed to decrease, as seen in Figure 2.10 [51]. At a high scan speed of 600 mm/s, however, a significant change in relative density and hardness was noted. This is owing to a lack of heat input to completely melt the powder, which results in greater lack-of-fusion porosity, thus lowering the relative density and hardness.

Sun et al. [52] used a multiple linear regression analysis to determine the best processing parameters for optimizing relative density in Ti6Al4V samples manufactured via L-PBF. The relative density was the output parameter, whereas linear energy density, hatch distance, powder layer thickness, and scanning strategy were the input parameters. The powder layer thickness was shown to be the most significant processing parameter on relative density.

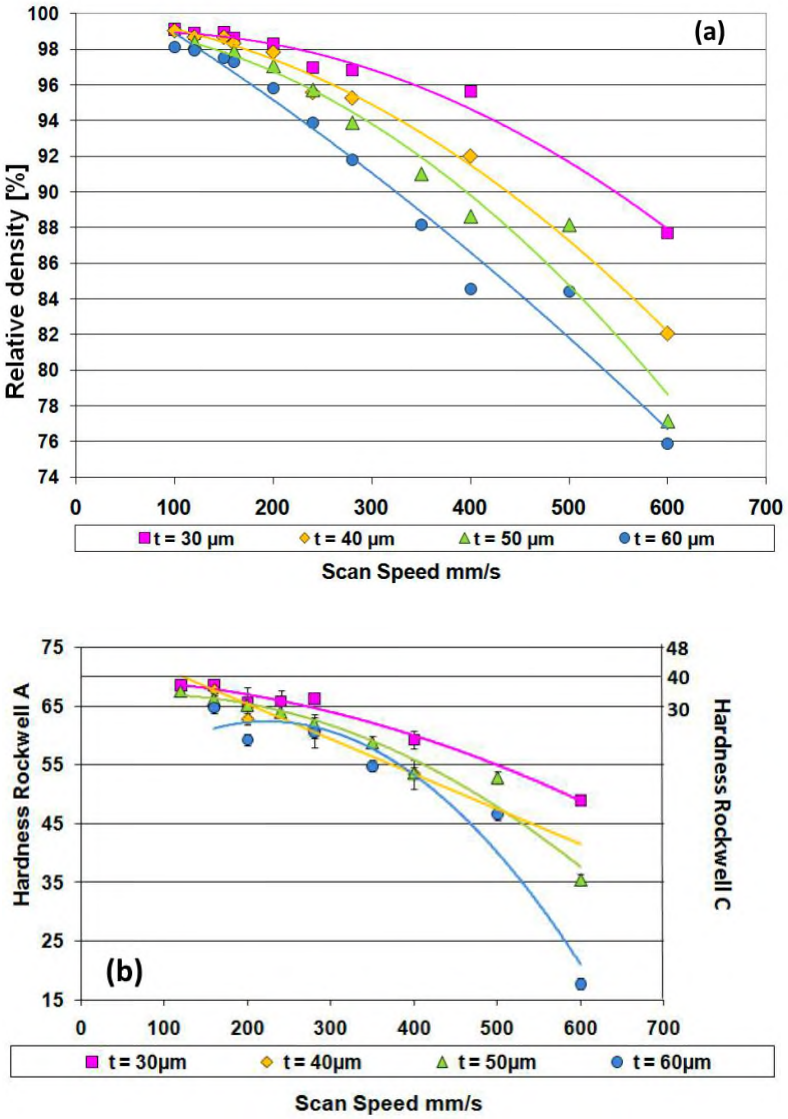

FIGURE 2.10: Effect of powder layer thickness and scan speed on (a) relative density and (b) macro-hardness of 18Ni-300 maraging steel built by L-PBF process [51].

Sufiiarov et al. [53], on the other hand, looked into the effect of the powder layer on the mechanical properties of IN718 samples produced with L-PBF. When the powder layer thickness was increased from 30 μm to 50 μm, both yield and ultimate tensile strength decreased. They linked their findings to increased porosity as a result of increasing layer thickness.

2.5.5 Powder Properties

The density, surface finish, dimensional accuracy, production rate, and mechanical properties of a part built by L-PBF are used to assess its quality. The L-PBF machine parameters chosen and the powder used affect the quality of AM parts [54]. Powder properties have a considerable influence on the quality of printed products as found in various investigations [55–59, 61].

A list of powder characteristics that influence the L-PBF process was identified by Dawes et al. [55]. The list covers the following items, in addition to the cost of powder, which is crucial for the L-PBF process:

- Particle morphology
- Particle size distribution
- Powder packing density
- Flowability
- Cohesiveness
- Particle porosity
- Optical properties
- Chemical composition

Powder production processes determine the shape of powder particles. Gas and plasma atomization are the most prevalent processes for producing metal powder. These technologies create more spherical powder particles than other methods, such as water atomization, which is cheaper and faster than the others [55]. Spherical particles flow better and faster than irregular or angular particle because of less particle interlocking. Coarse spherical particles also flow better than the fines,

which are less spherical. The percentage of fine particles within the powder directly affects powder flowability and packing density [24, 55, 56].

A certain proportion of fine particles among coarse particles is quite desirable. Fine particles accumulate in the gaps between coarse particles, increasing the powder bed packing density, resulting in decreased porosity and greater surface quality of printed parts [60]. However, because fine particles act as satellites for coarse particles, an excess of fine particles can increase adhesive and cohesive forces, substantially limiting powder flowability [60, 61]. As a result, there is a maximum allowable proportion of fine particles above which part properties may deteriorate.

Dobson et al. [56] found that 17–4 PH stainless steel powder with a particle diameter of less than 15 μm and roughly 30% of powder volume is helpful for powder flowability and powder packing density. However, a considerable percentage of about 55% drastically degrades the quality of printed objects. Furthermore, the inclusion of small particles with a wide range of particle sizes improves powder laser absorptivity, as demonstrated by King et al. [62]. When a laser beam comes into contact with a big particle, it is mostly reflected, resulting in little absorption and heat transfer. When the laser beam encounters a region of small particles, however, the laser absorptivity increases.

Powder flowability and packing density are influenced by particle size distribution (PSD). A narrow PSD enhances powder flowability while lowering packing density. A wide PSD, on the other hand, causes poor flowability while increasing layer packing density and consequently part density. L-PBF, in general, employs a finer PSD of 15–45 μm [55]. Powder with a larger PSD is also more likely to form

agglomerates and clusters, resulting in voids in the powder bed. Karapatis et al. [63] and Spierings et al. [64] proposed various relationships between fine and coarse particle sizes as well as layer thickness. They claimed that the relationships may assure good flowability and packing density, which would lead to improved part density and surface quality. The PSD may be monomodal, bimodal, or even multimodal. A monomodal distribution has just one peak, whereas a bimodal or multimodal distribution has two or more.

For the monomodal PSD, the relations are as follows [63, 64]:

$$t > D_{90} \quad typically \quad \frac{t}{D_{90}} \approx 1.5 \tag{2.5}$$

$$D_{10} \in [1.4, 2.5] \quad with \quad D_{10} \geq 5\ \mu m \tag{2.6}$$

$$\frac{D_{90}}{D_{10}} \in [2, 5] \quad typically \quad \frac{D_{90}}{D_{10}} \approx 5 \tag{2.7}$$

For the bimodal PSD, the relations are as follows [63, 64]:

$$t > D_{90,coarse} \quad typically \quad \frac{t}{D_{90,coarse}} \approx 1.5 \tag{2.8}$$

$$\frac{D_{50,coarse}}{D_{50,fine}} \geq 10 \quad with \quad D_{10,\ fine} \geq 5\ \mu m \tag{2.9}$$

$$\frac{m_{coarse}}{m_{fine}} \approx \frac{7}{3} \tag{2.10}$$

The thickness of the powder layer is indicated by the letter t. Percentile values are represented by D_{10}, D_{50}, and D_{90}. These statistical parameters can be determined using the cumulative particle size distribution. They show the cumulative particle size distribution for particles that account for less than 10%, 50%, and 90% of all particles, respectively. The powder mass is represented by the character m.

2.5.6 Scanning Strategy

The quality of printed parts is mainly influenced by processing parameters such as laser power, scan speed, hatch distance, powder layer thickness, and scanning strategy [19, 54]. Optimizing these processing parameters is an efficient way to achieve the required densification, microstructure, and mechanical properties for the printed parts. The scanning strategy, which is the geometrical pattern followed by the laser beam, has a significant impact on the temperature gradient and, in turn, the quality of the parts. Its adjusting can reduce cracks, balling, and residual stresses generated during processing [65].

Jhabvala el al. [66] proposed four scanning strategies and tested them experimentally by varying only laser power and scan speed. They used powders from high and low conductive materials. The four scanning strategies are as follows: parallel, spiral, paintbrush, and chessboard, as shown in Figure 2.11.

Figure 2.11 (a) shows the parallel scanning method, which is the easiest to apply from a CAD file. However, low scan speed causes high-temperature gradients to merge across the square surface, which is bad situation. One option to reduce the temperature gradients is to increase the scan speed. As a result, the laser power should be increased to avoid providing less heat energy to the powder. Nevertheless, the ability of the laser to boost its power is limited. Furthermore, it has been found that a combination of greater scan speed and laser power causes balling and cracking [66].

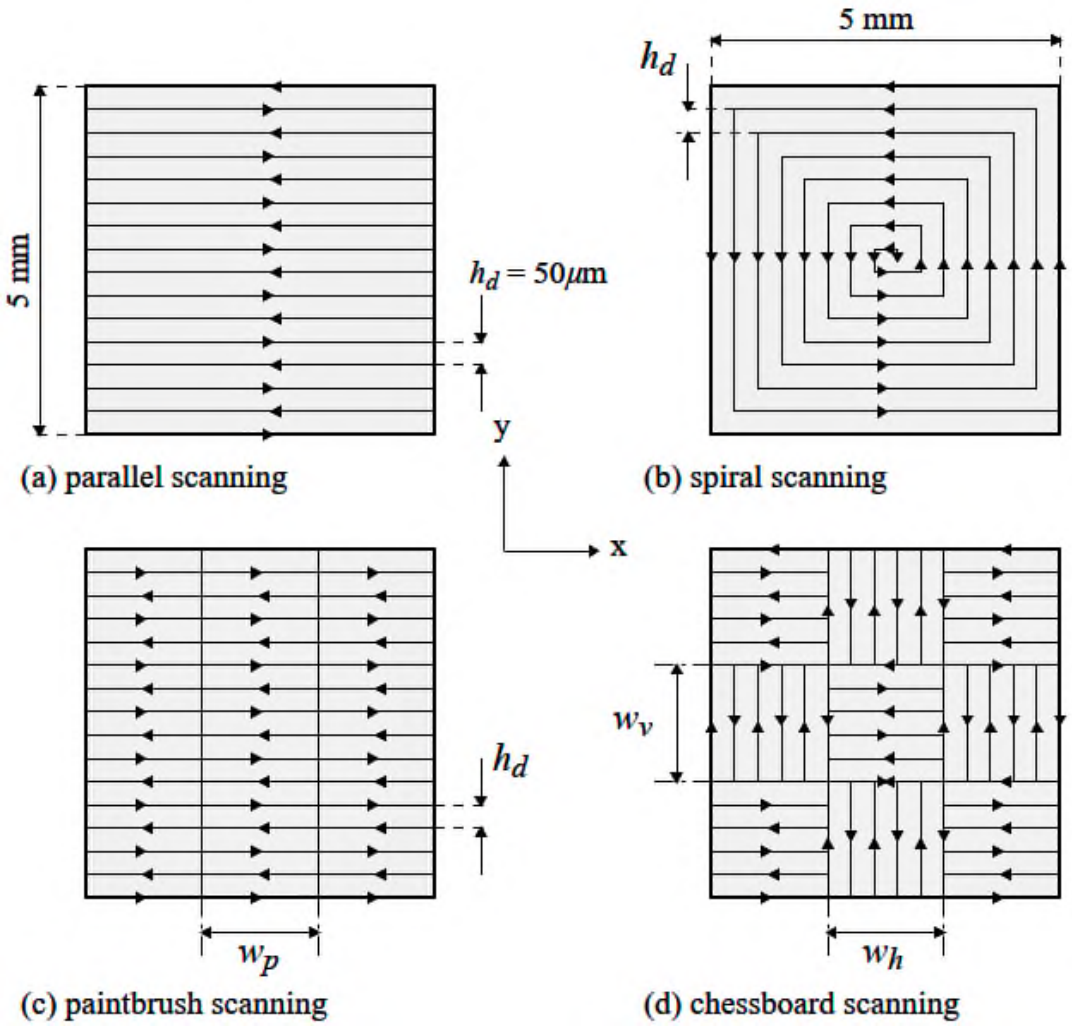

FIGURE 2.11: The four scanning strategies proposed by Jhabvala el al. [66].

For processing high-conductive powder at a greater scan speed, the spiral scanning strategy, depicted in Figure 2.11 (b), is often superior than the parallel method, resulting in strong bonds between the layers deposited. However, higher temperatures in the part centre produce overheating, resulting in a rough, porous surface. Furthermore, when processing low-conductive powder, the spiral scanning method causes balling and cracking [66].

Figure 2.11 (c) shows paintbrush scanning, which appears to be identical to parallel scanning but has a much smaller scan width (wp), which reduces temperature gradients when processing both low and high conductive particles. However, the bonding between the layers is insufficient, resulting in delamination.

Finally, in Figure 2.11 (d), the chessboard is a scaled-down version of the parallel scanning strategy. High-temperature gradients are considerably reduced when scaling down, resulting in high-quality printed parts. The scanning region in this case is divided into smaller cells. After that, parallel scanning in opposite directions is performed for each cell [66].

The effect of scanning strategy on relative density, surface roughness, residual stresses, microstructure, and mechanical properties of printed components has been investigated in several studies [65, 67–71]. Guo et al. [67] investigated the effects of parallel scanning (Figure 2.11 (a) [66]) and chessboard scanning (Figure 2.11 (d) [66]) on the relative density, microstructure, and mechanical properties of L-PBF AlSi10Mg samples. The density and mechanical properties of the samples printed using chessboard scanning were found to be superior to those of parallel scanning. Chessboard scanning, as opposed to parallel scanning, allows for faster heat dissipation and reduced temperature gradients.

Thijs et al. [68] examined the effect of scanning strategy on the microstructure and texture of L-PBF AlSi10Mg parts. They found that the scanning strategy, as shown in Figure 2.12 has no influence on the texture created during processing. The surface roughness of L-PBF Hastelloy X was improved using a contour scanning approach, according to Tian et al. [70]. When a contour scan was employed,

Figure 2.12 (c), the irregularities at the sample margins were found to be reduced. In this case, the contour scan works as a re-melting process, resulting in improved surface roughness.

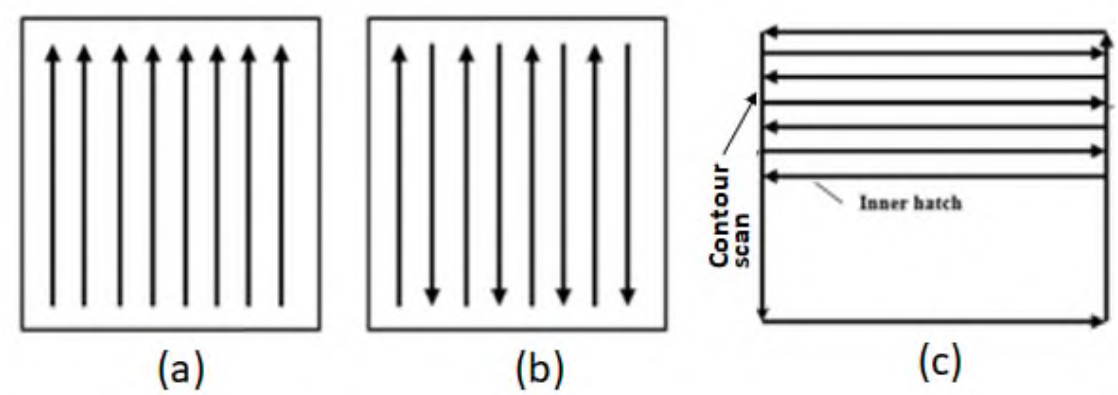

FIGURE 2.12: Schematic illustration of some scanning strategy. (a) Uni-directional, (b) bi-directional or zigzag scan, and (c) contour scan.

AlMangour et al. [72] studied the effects of four scanning strategies, shown in Figure 2.13, on the texture, grain size, and relative density of L-PBF TiC/316L nanocomposites samples. Rotating the scanning direction by 90° leads in robust layer bonding and improved relative density of the samples. On the other hand, double laser scanning, as shown in Figure 2.13 (b), produces more uniform and smoother layers, boosting relative density by eliminating pores between neighbouring layers.

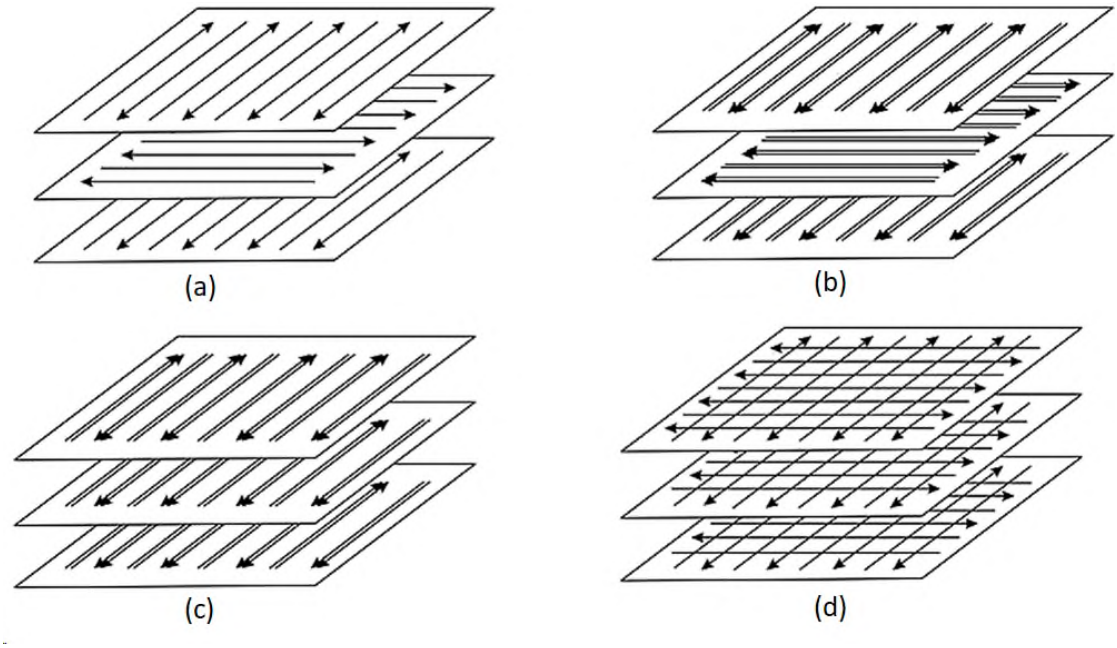

FIGURE 2.13: Schematic illustration of the four scanning strategies used by AlMangour et al. [72]. (a) Bi-directional, single pass of laser beam, 90° rotation of scan vector between layers; (b) bi-directional, double pass of laser beam, 90° rotation of scan vector between layers; (c) bi-directional, double pass of laser beam; and (d) cross scan.

2.5.7 Review of L-PBF IN625 Processing Parameters

As indicated in Table 2.1, a review of the literature on the optimal L-PBF processing parameters for manufacturing IN625 found that the powder layer thickness employed ranged from 20 to 60 μm. Throughout the literature review, the layer thickness was kept constant. There was also no systematic study on the effects of increasing the powder bed layer thickness on the density and hardness of L-PBF IN625 components.

TABLE 2.1: L-PBF processing parameters for printing IN625 reported in the literature

Laser Power (W)	**Scan Speed** (mm/s)	**Hatch Distance** (mm)	**Thickness** (mm)	**VED** (J/mm^3)	**Ref.**
160	500	0.06	0.02	267	[73]
169 182 195	725 800 875	0.09 0.10 0.11	0.02	95–140	[74, 75]
300	1000	0.10	0.04	75	[76]
140 150 175	750 850 950	0.09	0.02	90–110	[77]
175	600	0.14	0.03	69	[14]
140 170 220 270	500 550 600 650 700	0.08 0.10 0.12	0.04	42–169	[13]
195	800	0.10	0.02	122	[78]
195	1200	0.09	0.02	90	[27, 79–81]
150 200 250 300	600	0.14	0.06	30–60	[29]
200	600	0.14	0.06	40	[82]
200	500 800 1100	0.08	0.03	76–167	[83]
285	960 1440 1680 1920	0.11	0.04	34–68	[30]
253	500	0.10	0.06	84	[84]
180	1000	0.10	0.04	45	[16]

2.6 Porosity in L-PBF Parts

The porosity of parts made using the L-PBF process restricts the applications that can benefit from this technology. Porosity is a common defect that should be avoided or minimized since it may affect the mechanical properties of the parts [15, 29, 30]. Process-induced porosity occurs when the thermal energy provided to the powder bed is insufficient to completely melt the powder or when spatter ejection occurs due to too much heat delivered to the powder. These pores are often non-spherical and come in a wide range of shapes and sizes (sub-micron to macroscopic).

To avoid the mechanisms that generate the pores, processing parameters should be carefully adjusted. A bad combination of L-PBF parameters can result in a variety of defects, including lack of fusion, keyhole, and balling. Figure 2.14 depicts the combined effect of laser power and scan speed on the process output.

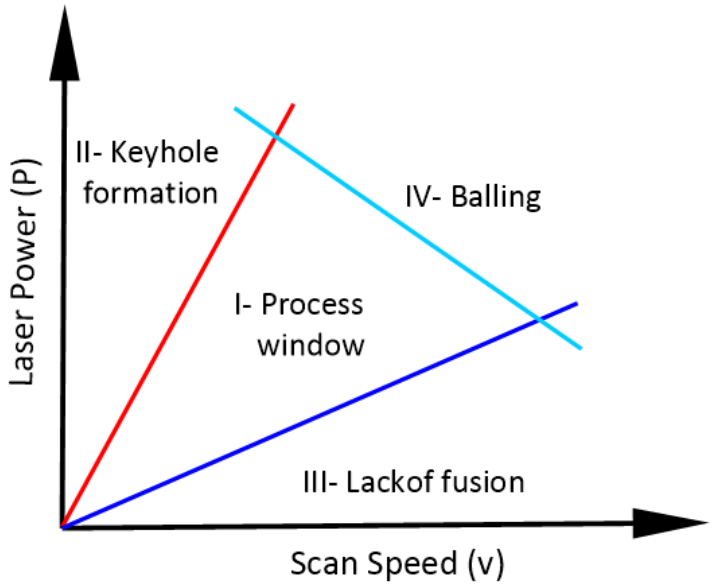

FIGURE 2.14: Schematic diagram of defect formation in relation to L-PBF processing parameters of laser power against scan speed. The diagram depicts the regions of keyhole, lack of fusion, balling, and operating window.

Physical and metallurgical phenomena including melting and remelting, wetting, metal evaporation and recoil pressure build-up, Marangoni convection as a result of surface tension gradient, solidification and re-solidification, and solid-state phase transformations occur during such a rapid laser-powder interaction and subsequent cooling [54, 85–89].

When a laser beam hits powder, photons are absorbed, converted to heat, and then dispersed through conduction. The energy delivered to the powder must be more than the energy dissipated for melting to occur. When the powder reaches its melting temperature, droplet coalescence causes a melt pool to form, which moves as the laser scan passes over it. The process condition is connected to the melt pool geometry (width and depth) and hydrodynamics. Based on laser melting mechanisms and melt pool stability, which are dependent on laser power and scan speed combinations, four zones can be identified, as illustrated in Figure **??**.

According to King et al. [90], there are two melting modes: conduction and keyhole mode. In conduction mode (Region I, Operating Window, Figure **??**), efficient laser-powder interaction occurs owing to appropriate thermal energy given to the powder. As a result, the powder layer is totally melted with little remelting of the underlying layer. Conduction mode, on the other hand, is characterized by the formation of a small depression (cavity) to establish a stable melt pool. Almost fully dense parts can be produced in this region. Figure 2.15 (a) provides a schematic representation of effective L-PBF processing with a stable melt pool demonstrating the conduction mode, while Figure 2.15 (b) depicts the cross section of a single track printed with a laser power of 150 W, scan speed of 188 mm/s and powder layer thickness of 50 μm [90].

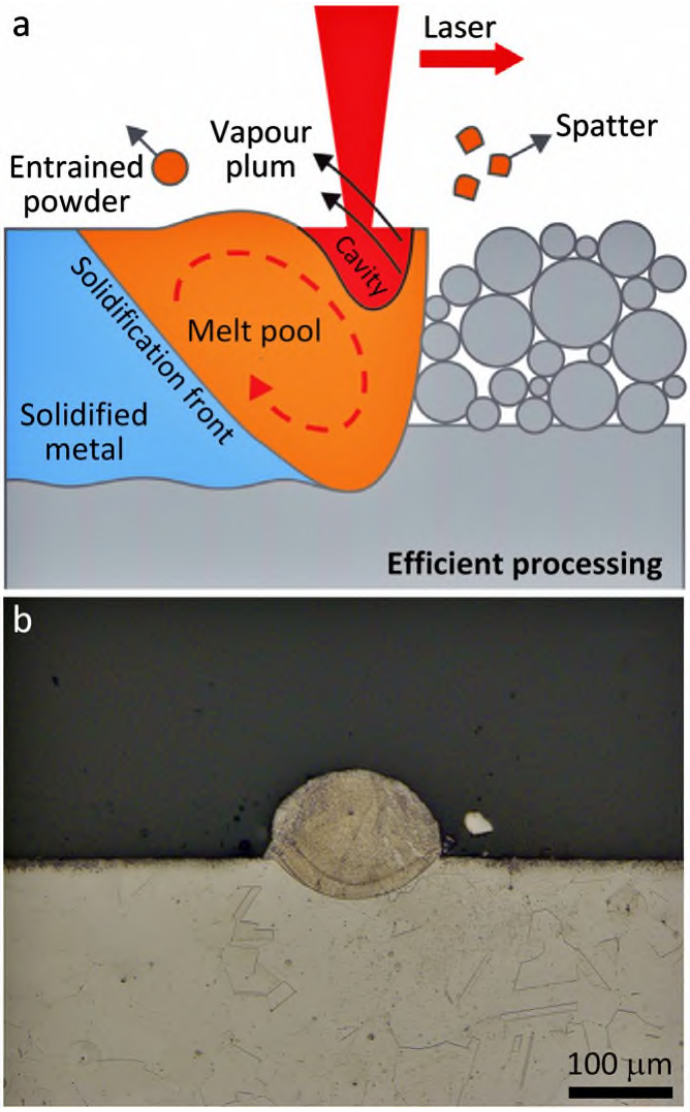

FIGURE 2.15: Efficient processing with a stable melt pool in L-PBF processing. (a) Schematic illustration showing the conduction mode melting [91]. (b) Cross-section single track printed using 316L SS powder with laser power of 150 W, scan speed of 188 mm/s and powder layer thickness of 50 μm [90].

The melt pool shifts from conduction to keyhole (Region II, Figure **??**) when the thermal energy given to the powder climbs above a threshold, which depends on the process parameters, material thermal properties, and powder characteristics. In this situation, a significant amount of material is evaporated, resulting in gas bubbles. When the recoil pressure exceeds the surface tension, the melt pool penetrates deeply into the underlying material, generating a narrow and deep cavity, as shown in Figure 2.16 (a). As the cavity cools, the Marangoni effect and surface tension accelerate its collapse, trapping gas bubbles and leaving a trail of approximately spherical pores beneath the melt pool surface, as illustrated in Figure 2.16 (b) [90].

However, lowering laser power or increasing scan speed is a common method for avoiding keyhole porosity. Melt pool dynamics regulate keyhole porosity exclusively, therefore changes in layer thickness and hatch distance have little influence. According to King et al. [90], laser power has a greater effect on keyhole porosity than scan speed. Due to extreme spatter activity as laser power increases, eliminating keyhole porosity becomes more challenging [92].

A lack of fusion (Region III, Figure **??**) is another type of process-induced porosity. Because it lowers the mechanical properties of the final parts, a lack of fusion porosity should be prevented or minimized. A combination of low laser power and high scan speed results in insufficient thermal energy to be delivered to the powder bed, leading to a lack of fusion due to inadequate melt pool penetration and incomplete melting.

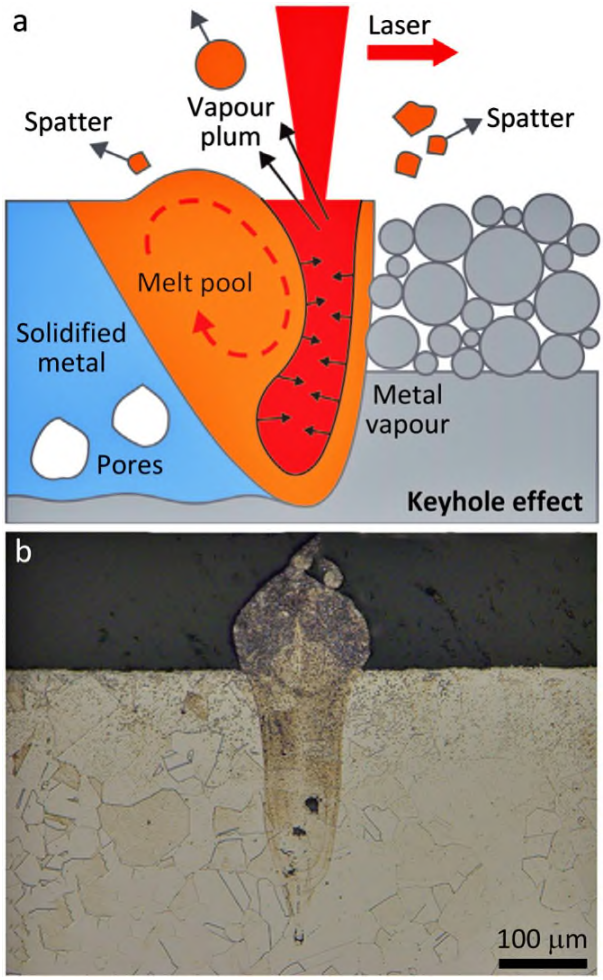

FIGURE 2.16: Keyhole mode with an unstable melt pool in L-PBF processing. (a) Schematic diagram of keyhole mode melting [91]. (b) Cross-section of a single track showing pores due to keyhole effect [90].

As a result, as shown in Figure 2.17 (a), small and shallow melt pool forms with significantly less metal evaporation and spatter. A lack of fusion porosity can also be indicated by the presence of unmelted powder particles in or around the pores. Lack-of-fusion has irregular geometries, unlike gas and keyhole porosity, and it is commonly observed between layers or along the scanned track. Furthermore, the incomplete melting yields a considerable level of porosity, partially sintered particles, and extremely rough surface, as seen in Figure 2.17 (b) [93].

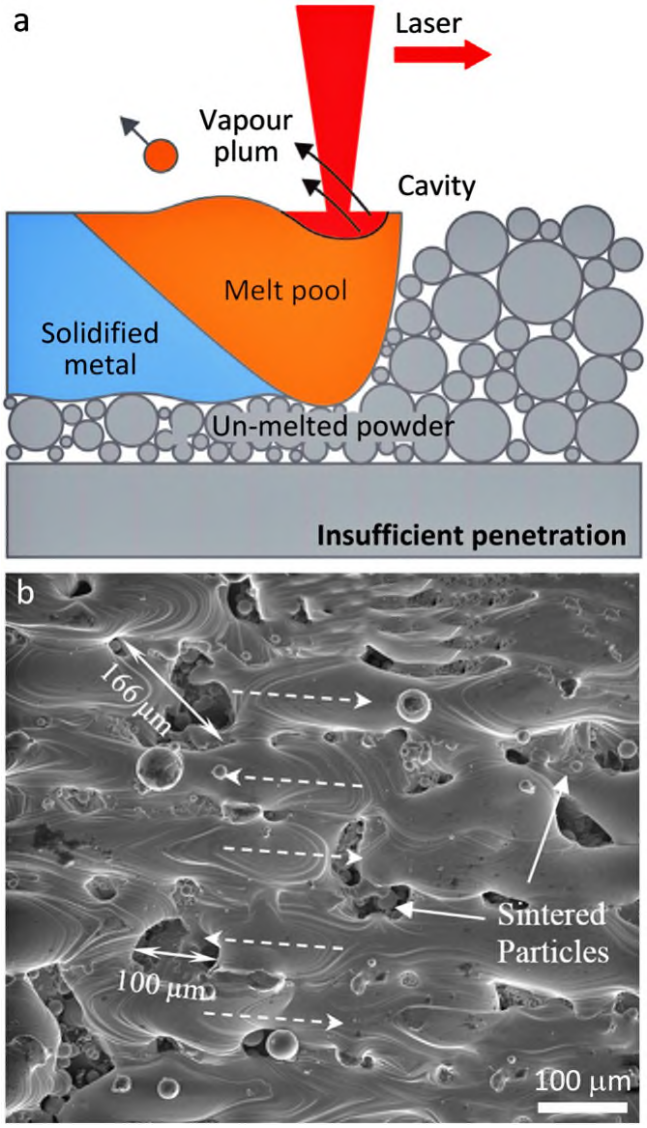

FIGURE 2.17: Lack of fusion defect in L-PBF processing. (a) Schematic illustration showing insufficient melt pool penetration [91]. (b) Top surface of a part fabricated by L-PBF using Ti6Al4V powder with laser power of 80 W, scan speed of 1080 mm/s showing the presence of lack of fusion porosity and partially sintered particles [93].

Balling (Region IV, Figure **??**) develops when a laser beam moves faster than a certain speed. As a result, the melt pool becomes unstable and divides into isolated, smaller droplets (Figure 2.18), which solidify into discontinuous metal beads [26, 46, 54].

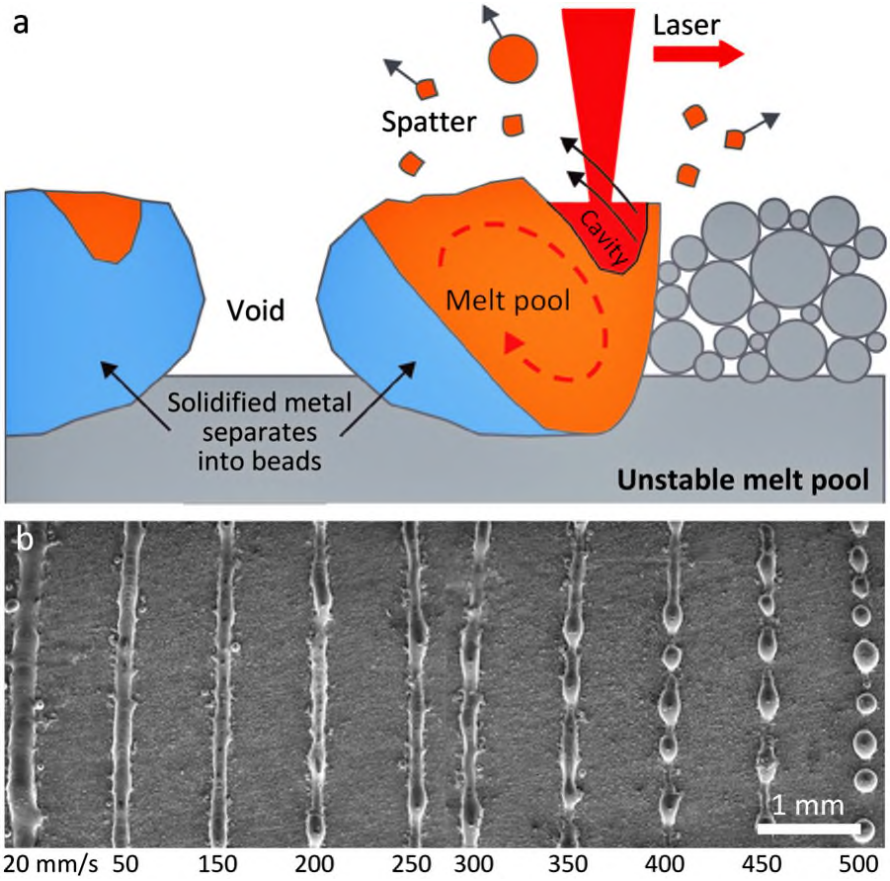

FIGURE 2.18: Balling in L-PBF processing. (a) Schematic illustration showing balling [91]. (b) Single tracks printed by L-PBF process under various scan speeds showing how scan speed induces balling [46].

Balling can be reduced by increasing the laser power at a constant scan speed to improve wetting and spreading of the melt pool. Balling, on the other hand, increases surface roughness and porosity, resulting in poor mechanical properties and, in the worst-case scenario, an incomplete process. Balling can be mitigated by lowering oxygen levels in the surrounding environment, improving linear energy density with high laser power and low scan speed, and remelting the surface for enhanced wettability [46].

Han et al. [94] investigated the effect of volumetric energy density on the relative density of L-PBF Ti6Al4V samples, as shown in Figure 2.19. As the laser energy density increased, so did the relative density, reaching a peak at around 150 J/mm^3 and then rapidly decreasing. The authors divided the relative density curve into three zones:

- Zone I had weak metallurgical bonding between adjacent laser melted tracks or layers due to very low thermal energy supplied to the powder bed.
- Zone II had maximum relative density.
- Zone III had low relative density due to excessively high energy provided to the powder bed.

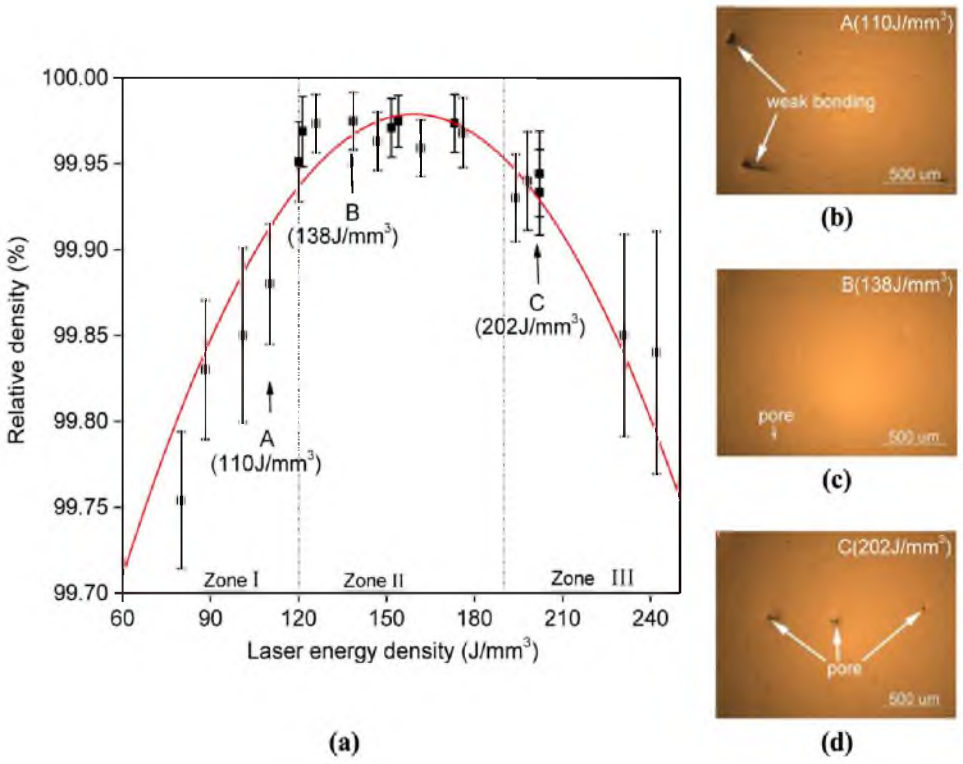

FIGURE 2.19: L-PBF Ti6Al4V, (a) relative density as a function of volumetric energy density, and (b, c, d) optical images showing some defects captured [94].

2.7 Superalloys

Superalloys are high-temperature materials that retain their properties at elevated operating temperatures above about 0.6 T_m, where T_m is the melting point. Furthermore, they are resistant to oxidation, creep, and fatigue and exhibit outstanding resistance in corrosive and harsh environments [95]. As a result, they are used in various industries, including aerospace, marine, nuclear, and chemical.

Superalloys are classified based on the major alloying elements into three types: iron-nickel-based, cobalt-based, and nickel-based superalloys. They are among the most complicated metallic alloys ever made by mankind, with over ten alloying elements influencing their properties directly [1, 95, 96]. Significant levels of Cr, Mo, Nb, Fe, Co, Al, and Ti are present in the majority of superalloys. Small quantities of B, Zr, and C are usually added as well. Depending on the alloying elements, superalloys can be strengthened by at least one of the following hardening mechanisms: solid solution hardening, precipitation hardening, and carbides precipitates [1, 95, 96].

Iron-nickel-based superalloys are developed from stainless steel and used for applications at moderate temperatures (up to about 700 °C), especially in gas turbine engines due to their low thermal expansion. These alloys are less expensive than cobalt or nickel based alloys owing to the addition of a significant amount of iron as a main element. Table 2.2 depicts the chemical composition of several iron–nickel alloys used in jet engines, the majority containing 15–60% iron and 25–45% nickel. The iron-nickel superalloys are strengthened by solid solution and precipitation hardening [1].

TABLE 2.2: Chemical composition of iron–nickel-based superalloys [1].

	Composition (%)									
Alloy	Fe	Ni	Cr	Mo	W	Co	Nb	Al	C	Other
Solid solution-hardened alloys										
Haynes 556	29.0	21.0	22.0	3.0	2.5	20.0	0.1	0.3	0.1	0.5 Ta
Incoloy	44.8	32.5	21.0	–	–	–	–	0.6	0.36	
Precipitation-hardened alloys										
A-286	55.2	26.0	15.0	1.25	–	–	–	0.2	0.04	0.3 V
Incoloy 903	41.0	38.0	<0.1	0.1	–	15.0	3.0	0.7	0.04	

Cobalt-based superalloys are commonly used in components working under low stresses and require excellent hot-corrosion resistance; they are important alloys for gas turbine engines [1]. They outperform iron-nickel and nickel-based superalloys in terms of hot corrosion resistance. Table 2.3 shows the chemical composition of some cobalt-based alloys used in jet engine components. Cobalt-based superalloys contain about 30–60% Co, 10–35% Ni, 20–30% Cr, 5–10% W, and less than 1% C. The main functions of the alloying elements are to strengthen the cobalt by solid solution or precipitation hardening [1].

TABLE 2.3: Chemical composition of cobalt-based superalloys [1].

	Composition (%)									
Alloy	Co	Fe	Ni	Cr	Mo	W	Nb	Al	C	Other
Haynes 25	50.0	3.0	10.0	20.0	–	15.0	–	–	0.1	1.5 Mn
Haynes 188	37.0	<3.0	22.0	22.0	–	14.5	–	–	0.1	0.9 La
MP35-N	35.0	–	35.0	20.0	10.0	–	–	–	–	

Nickel-based superalloys are commonly used in high-temperature applications exceeding 700 °C. They can operate at temperatures ranging from 800 to 1000 °C for an extended time. Therefore, they have found applications in the hottest components of gas turbine engines [1, 95, 96].

2.7.1 Nickel-Based Superalloys

At high temperatures above 800 °C, nickel-based superalloys are the most commonly used metallic materials in aircraft turbine engines because they exhibit high strength, excellent resistance to fatigue, creep, and stress rupture, and outstanding oxidation and corrosion resistance [1, 95, 96]. When compared to other metallic materials used in aircraft structures, nickel-based alloys provide excellent stress rupture resistance, as shown in Figure 2.20.

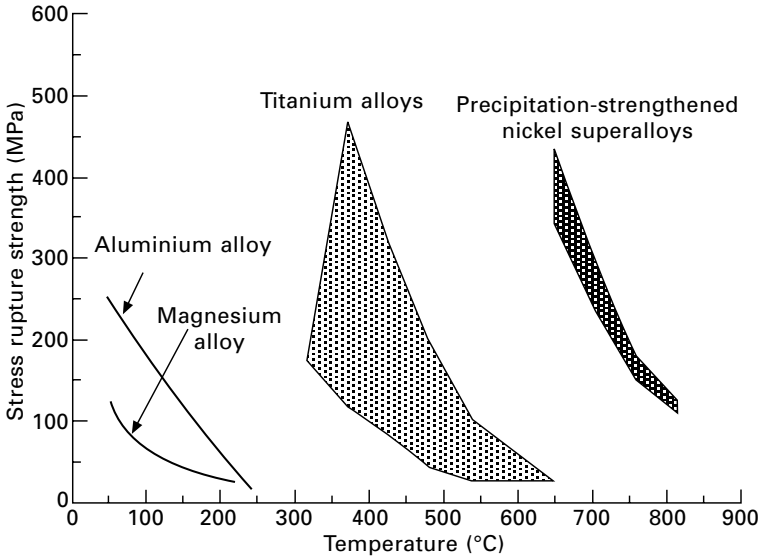

FIGURE 2.20: Stress rupture strength of aerospace materials as a function of temperature [1].

Nickel-based superalloys have a minimum Ni content of 50%. The majority of these alloys contain more than ten alloying elements, including 10–20% Cr, 5–15% Co, and up to 8% Al+Ti, as well as minor amounts of Mo, W, and C. The average chemical composition of Ni-based superalloys used in jet engine components is shown in Table 2.4. Ni-based alloys are strengthened by solid solution hardening

or a combination of solid solution and precipitation hardening, depending on the alloying elements added. Table 2.5 depicts the main functions of the alloying elements in Ni-based alloys [1, 95, 96].

TABLE 2.4: average chemical composition (wt.%) of nickel-based superalloys [1].

	Composition									
Alloy	Ni	Fe	Cr	Mo	W	Co	Nb	Al	C	Other
Astroloy	55.0	–	15.0	5.3		17.0	–	4.0	0.06	
Hastelloy X	49.0	18.5	22.0	9.0	0.6	1.5	3.6	2.0	0.1	
Inconel 625	61.0	2.5	21.5	9.0	–	–	–	0.2	0.15	<0.25 Cu
Nimonic 75	75.0	2.5	19.5	–	–	–	–	0.15	<0.08	1 V
Inconel 100	60.0	<0.6	10.0	3.0	–	15.0	–	5.5	<0.08	2.9 (Nb+Ta)
Inconel 706	41.5	37.5	16.0	–	–	–	5.1	0.2	0.12	<0.15 Cu
Inconel 716	52.5	18.5	19.0	3.0	–	–	5.2	0.5	0.05	0.1 Zr
Inconel 792	61.0	3.5	12.4	1.9	3.8	9.0	–	3.5	0.04	
Inconel 901	42.7	34	13.5	6.2	–	–	–	0.2	0.16	0.3 V
Discaloy	26.0	55	13.5	2.9	–	–	3.5	0.2	0.15	0.5 Zr
Rene 95	61.0	<0.3	14.0	3.5	3.5	8.0	–	3.5	0.14	
Rene 104	52.0	–	13.1	3.8	1.9	18.2	1.4	3.5	0.03	2.7 Ta
SX PWA1480	64.0	–	10.0	–	4.0	5.0	–	5.0		2 Hf
DS PWA1422	60.0	–	10.0	–	12.5	10.0		5.0		

TABLE 2.5: Main functions of alloying elements in nickel-based superalloys [1].

Alloying element	Function
Chromium	Solid solution strengthening; corrosion resistance
Molybdenum	Solid solution strengthening; creep resistance
Tungsten	Solid solution strengthening; creep resistance
Cobalt	Solid solution strengthening
Niobium	Precipitation hardening; creep resistance
Aluminium	Precipitation hardening; creep resistance
Carbon	Carbide hardening; creep resistance

2.7.2 Inconel 625 Superalloy

IN625 superalloy is widely used in the aerospace, chemical, petrochemical, nuclear, and marine industries. This is due to its great high-temperature strength, outstanding resistance to stress rupture, creep, and fatigue, and high oxidation and corrosion resistance [1, 4, 7]. IN625 is a nickel-based superalloy with about 62 wt.% nickel and 20–23 wt.% chromium, solid-solution strengthened by molybdenum (8–10 wt.%) and niobium (3.15–4.15 wt.%) in a nickel-chromium matrix. Chromium provides high corrosion resistance to the alloy by forming a passive thin layer of Cr_2O_3, while molybdenum and niobium strengthen the matrix [1, 4, 7].

The typical physical and mechanical properties of a conventional IN625 alloy are listed in Table 2.6 and Table 2.7 [98].

TABLE 2.6: Physical properties of conventional IN625 alloy.

Property	**Value**
Melting Point	1350 *°C*
Coefficient of Expansion	12.8 $\mu m/m.°C$ *(20–100 °C)*
Density	8.44 g/cm^3
Modulus of Elasticity	205.8 *GPa*
Modulus of Rigidity	79 *GPa*

TABLE 2.7: Mechanical properties of conventional IN625 alloy (rolled) [98].

Property	**Value**
Tensile Strength (MPa)	827–1103
Yield Strength (MPa)	414–758
Elongation (%)	30–60
Reduction of Area (%)	40–60
Hardness (Brinell)	175–240

2.7.2.1 Microstructure

L-BPF IN 625 alloy has a microstructure that is notably different from normally produced alloys. Due to very high cooling rates of about 10^6 K/s [97], the as-built IN625 alloy shows a non-equilibrium microstructure with very fine dendritic-cellular features generally less than 1 μm. Diffusion to create precipitates is hampered by the fast cooling rate, leaving the Ni matrix with the majority of strengthening elements such as Mo and Nb [73].

The as-built IN625 microstructure exhibits pronounced grain elongation along the build direction, with non-uniform crystallographic orientations within the grains [99], in contrast to the equiaxed grain structure of a conventionally fabricated IN625 alloy, as shown in Figure 2.21 [98]. The grains grow epitaxially from the substrate along the build direction (Z-axis), intersecting multiple melt pools, as shown in Figure 2.22 [79].

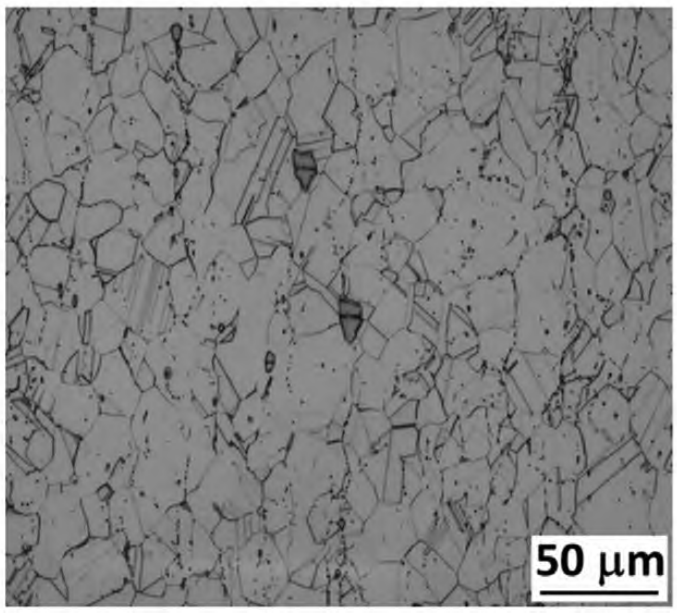

FIGURE 2.21: Optical micrograph of conventionally manufactured IN625 [98].

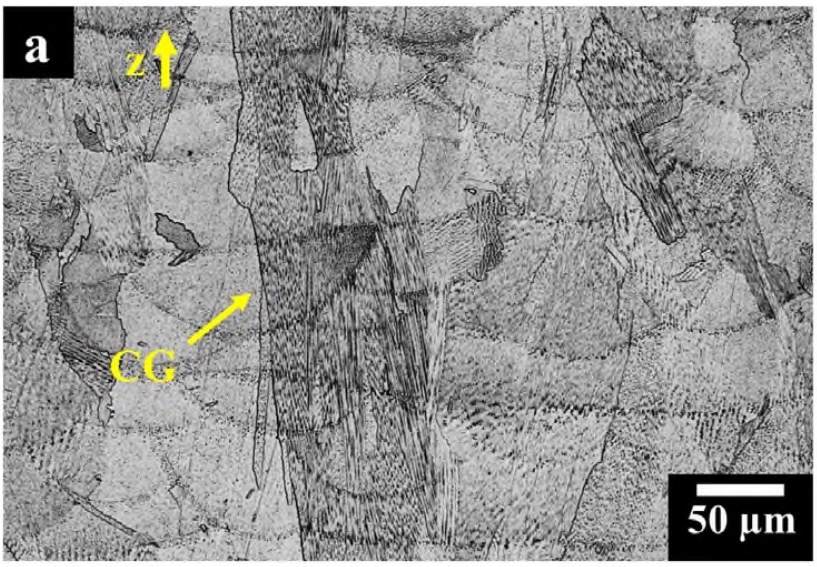

FIGURE 2.22: Cross-section optical micrograph of L-PBF IN625 superalloy along the build direction (Z-axis). The yellow arrow shows the columnar grain (CG) [79].

Moreover, the structure of the previous layer determines the columnar dendritic growth in the top layer. Partially melted grains from the preceding layer serve as pre-nuclei for dendritic epitaxial development in the newly melted layer. The change in heat flux direction near the top layer causes a change in dendrite orientation from vertical to horizontal [16, 99, 100].

2.7.2.2 Hardness

Hardness of a material is a measure of its resistance to localized plastic deformation. It is determined by pressing a small indenter into the surface of the material being tested under controlled load and time conditions. The depth or size of the indentation that results is measured and linked to a hardness number [101]. Hardness testing is one of the most often used mechanical property characterization

tests to provide an indicator of a material condition because it is cheap, non-destructive, and simple to execute. Moreover, other mechanical properties, such as tensile strength, can be easily estimated using hardness data [101].

The hardness of as-built materials is influenced by L-PBF processing parameters and powder properties [77]. Because of the very short solidification time, which is a characteristic of the L-PBF process, the hardness of as-bulit IN625 alloy is superior to that of conventional alloy. The extremely rapid solidification prevents the grains from growing (i.e. diffusion does not have enough time to work.) and results in a very fine microstructure [102].

According to the well-known Hall-Petch formula [102], a finer microstructure has a higher hardness than a coarser microstructure for a given material. This is due to the presence of additional grain boundaries in a smaller grained microstructure, which act as barriers to dislocation migration, enhancing hardnesss [102]. Furthermore, residual stresses are abnormally large due to considerable temperature gradients induced during processing. As a result of their fine microstructure and residual stresses, AM samples have a higher hardness than conventional samples.

Pleass and Jothi [77] found that, as shown in Figure 2.23, the plane XZ parallel to the build direction (Z-axis) is harder than the plane XY perpendicular to it. Dislocations must form and move beneath the surface when a hardness indentation is done. The dislocations developed in plane XZ interact with all of the grain boundaries visible in the plane XY, causing the dislocations to cease and the material hardness to rise. The dislocations in plane XY, on the other hand,

encounter larger grains and fewer obstacles as they go deeper into the plane XZ. As a result, the plane XY is expected to have a lower hardness than the plane XZ [77].

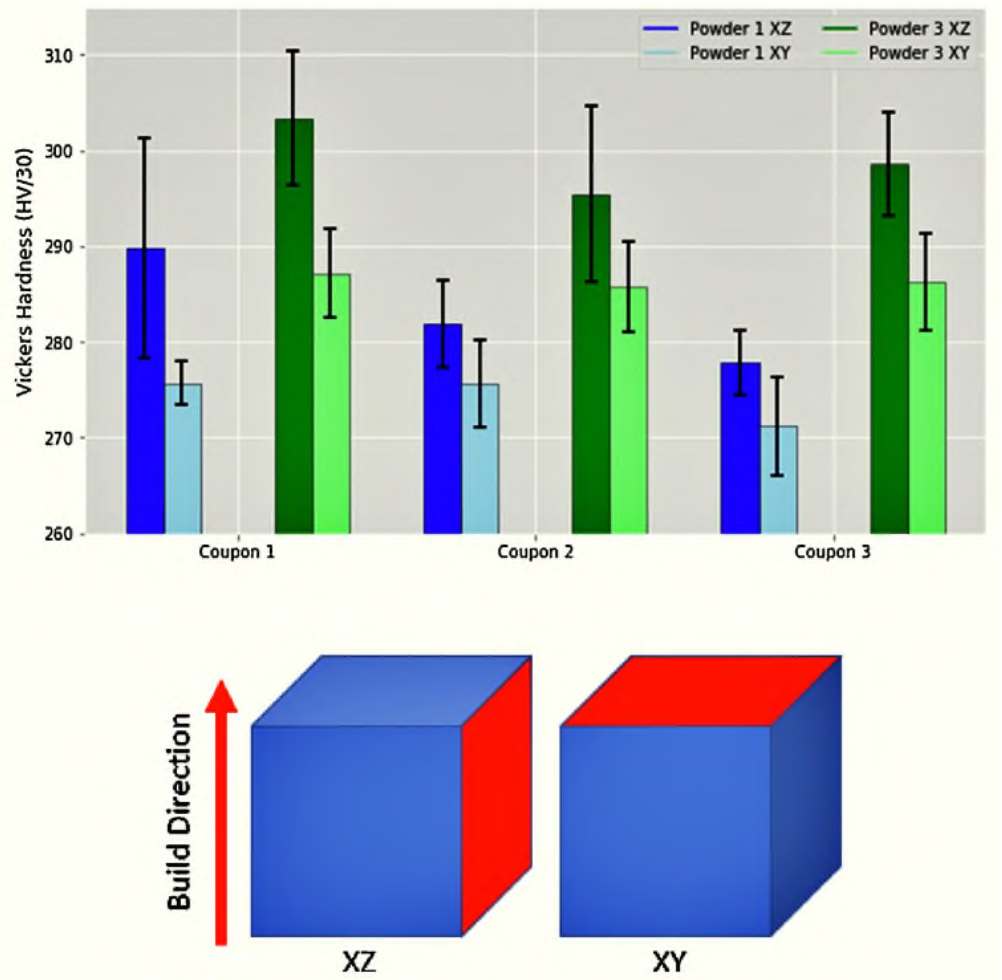

FIGURE 2.23: Vickers hardness made in the XZ and XY planes of three coupons of IN625 produced by L-PBF using two types of powder [77].

Ghodsi et al. [103] changed the laser power, scan speed, and hatch distance while keeping the layer thickness of 25 μm constant when printing IN625 samples using the L-PBF technique. They investigated the correlation between hardness

and volumetric energy density and detected a hardness peak followed by a sharp reduction in hardness, as shown in Figure 2.24.

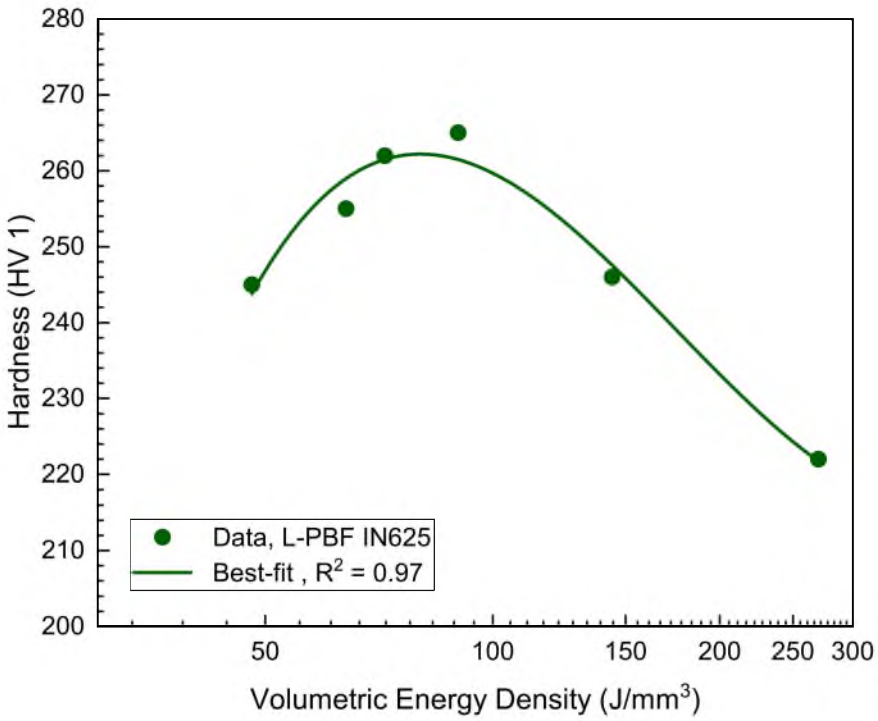

FIGURE 2.24: Hardness of L-PBF as-built IN625 as a function of volumetric energy density, adapted from [103].

A summary of mean hardness data obtained in plane XZ (along the build direction) of as-built IN625 alloy produced by L-PBF is provided in Table 2.8.

TABLE 2.8: Summary of average hardness data obtained in plane XZ of as-built IN625 alloy manufactured by L-PBF.

Laser Power (W)	**Scan Speed (mm/s)**	**Hatch Distance (mm)**	**Layer Thickness (mm)**	**Mean Hardness (HV)**	**Ref.**
160	500	0.06	0.02	343 HV 0.5	[73]
120	100	0.10	0.05	298 ± 7.0 HV 0.3	[104]
120	200	0.10	0.05	334 ± 9.0 HV 0.3	
80	100	0.10	0.05	334 ± 12 HV 0.3	
80	200	0.10	0.05	350 ± 9.0 HV 0.3	
80	1500	0.10	0.05	348 ± 24 HV 0.2	[105]
140	850	0.09	0.02	290 ± 11 HV 30	[77]
150	750	0.09	0.02	277 ± 4.0 HV 30	
175	950	0.09	0.02	281 ± 5.0 HV 30	
200	1000	0.09	0.03	262 HV 0.5	[106]
170	600	0.10	0.04	331 ± 10 HV 0.1	[13]
170	600	0.12	0.04	329 ± 12 HV 0.1	
170	700	0.10	0.04	330 ± 11 HV 0.1	
170	700	0.12	0.04	324 ± 14 HV 0.1	
270	600	0.10	0.04	319 ± 8.0 HV 0.1	
270	600	0.12	0.04	313 ± 11 HV 0.1	
270	700	0.10	0.04	334 ± 9.0 HV 0.1	
270	700	0.12	0.04	327 ± 10 HV 0.1	
247	1000	0.08	0.02	313 ± 9.0 HV 0.5	[107]
180	1000	0.10	0.04	304 ± 8.0 HV 0.3	[16]
280	950	0.11	0.03	322 ± 6.0 HV 0.2	[108]
50	1040	0.04	0.025	245 HV 1	[103]
50	520	0.06	0.025	255 HV 1	
75	1040	0.04	0.025	263 HV 1	
120	590	0.09	0.025	265 HV 1	
100	222	0.125	0.025	246 HV 1	
140	345	0.06	0.025	222 HV 1	

Chapter 3

MATERIALS AND METHODS

3.1 Introduction

The strategy for optimizing density, hardness, and productivity by modifying the processing parameters of IN625 fabricated using the L-PBF technique was divided into four stages: preliminary, exploratory, modelling, and optimization. It begins with a literature review, which provides important information about L-PBF IN625 superalloy.

As a preliminary test, IN625 parts were printed with a typical layer thickness of 30 μm using higher laser powers of 300 and 400 W. However, because cracked parts were printed, as illustrated in Figure 3.1, this layer thickness was excluded from the testing program.

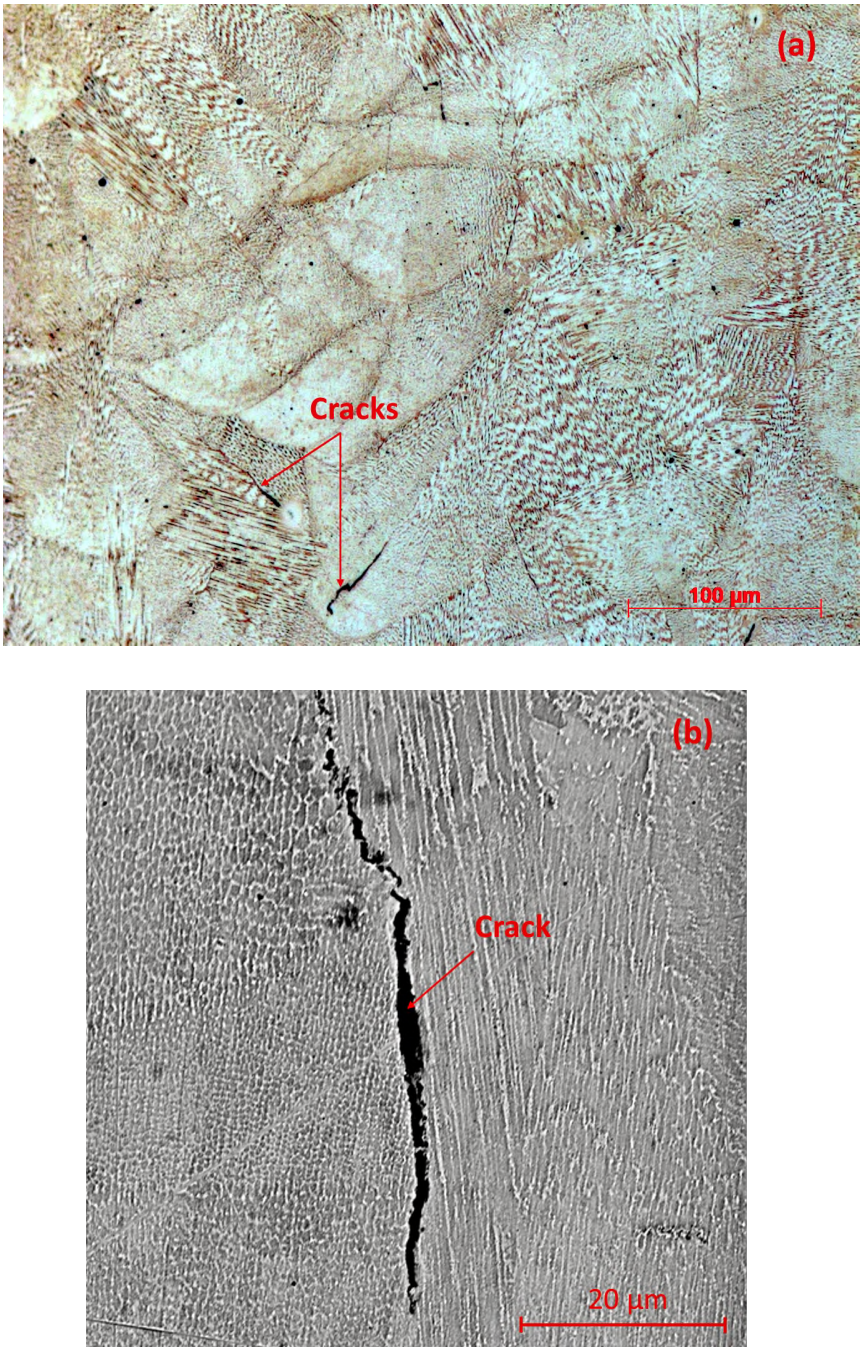

FIGURE 3.1: Cracks in L-PBF IN625 printed with $t = 30\ \mu m$. (a) $P = 300\ W$ and (b) $P = 400\ W$.

The exploratory step that follows focuses on printing single tracks to locate the process window. Nine single tracks were printed for each set of processing parameters. The top views and cross-sections of the tracks were characterized using light microscopy. As a result, common L-PBF process defects, such as lack of fusion, keyhole, and balling, were discovered. In addition, an empirical model was proposed to relate track width with surface energy density.

The third stage begins with the printing of $10 \times 10 \times 10\ mm^3$ cubes at various laser powers, scan speeds, overlaps, and powder layer thicknesses. A total of 48 cubes were printed. The relative density of printed cubes was determined using Archimedes principle. An empirical model was also developed to describe the relative density in terms of surface energy density. The most significant parameter influencing the relative density was identified. Moreover, multiple regression analysis, contour mapping, and 3D plotting were done to define the best processing parameters for maximum density. As a result, four sets processing parameters were estimated and with which 24 new cubes were printed, where six replicas for each set. Finally, the sets of processing parameters were validated by evaluating the density using both Archimedes and image analysis methods, productivity, hardness, and microstructure. Figure 3.2 depicts the work steps taken to achieve the study objective.

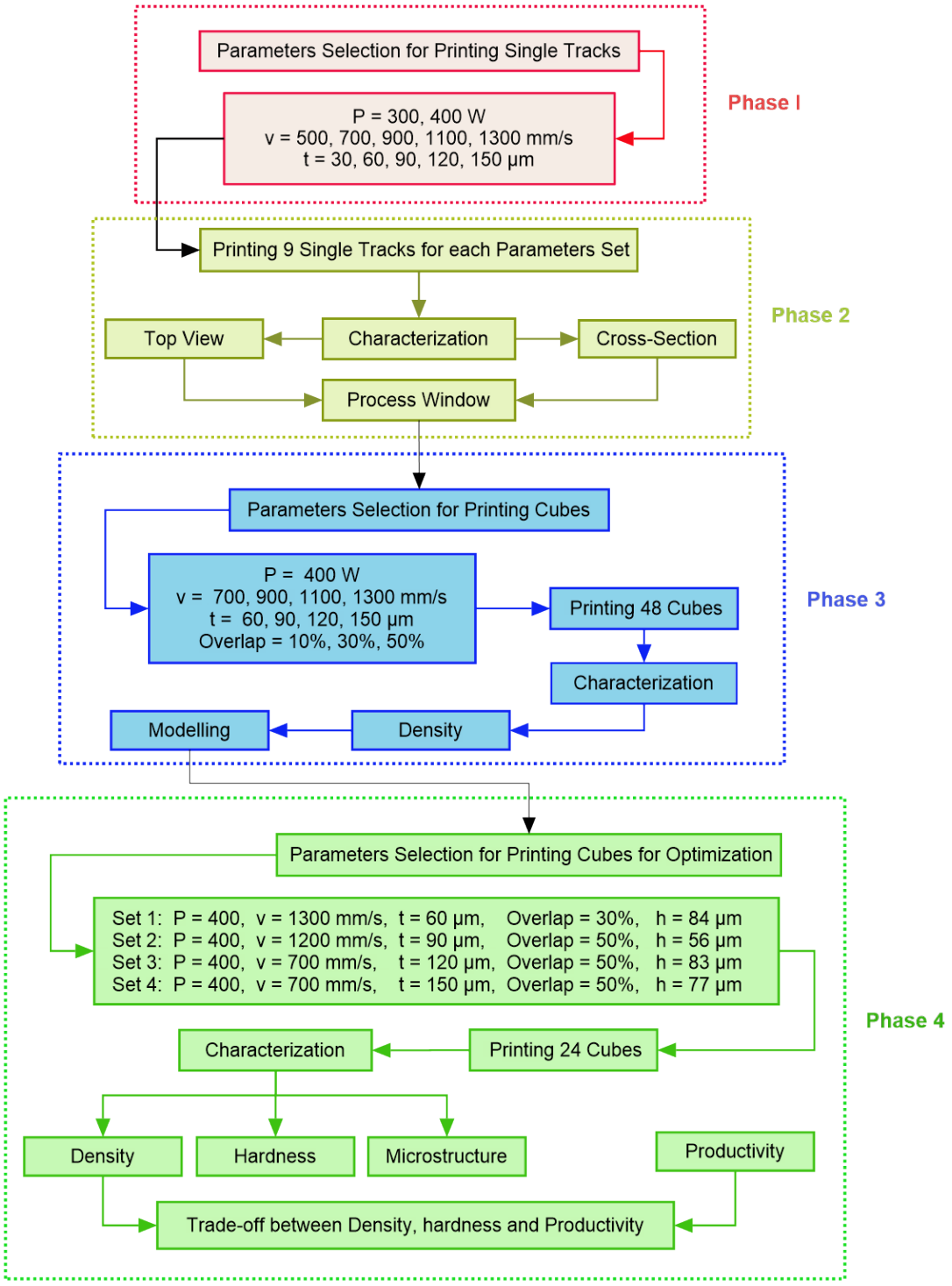

FIGURE 3.2: Flowchart depicts the work steps taken to achieve the study objective.

3.2 Printing of Single Tracks

Nine single tracks were printed for each set of processing parameters, as seen in Figure 3.3. Each track is 10 mm long, and the distance between adjacent tracks is 1.05 mm. Gas-atomized IN625 powder with particle sizes ranging from 20 to 53 μm was used as a feedstock.

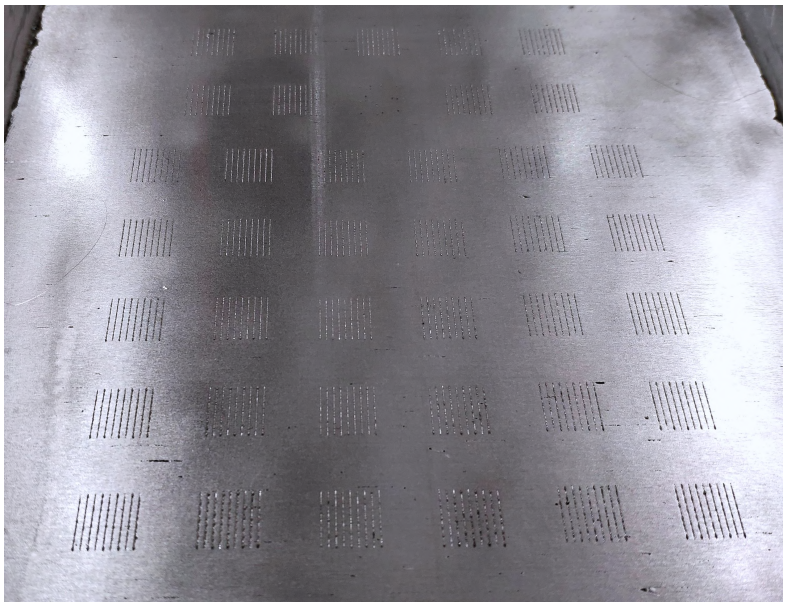

FIGURE 3.3: Single tracks of IN625 printed by L-PBF.

The apparent density and the flow rate of the powder are 4.47 g/cm^3 and 14.6 sec/50 g, respectively. The chemical composition, morphology, particle size distribution (PSD), and statistical analysis of the powder are shown in Table 3.1, Figure 3.4, Figure 3.5, and Table 3.2, respectively.

TABLE 3.1: Chemical composition (wt.%) of IN625 powder

	Ni	Cr	Mo	Nb	Fe	Mn	Si	C	O
ASTM	Bal.	20–23	8–10	3.15–4.15	1.5 max	0.2–0.5	0.3–0.5	0.03	0.07
Powder	Bal.	21.3	8.9	3.54	0.65	0.39	0.42	0.01	0.07

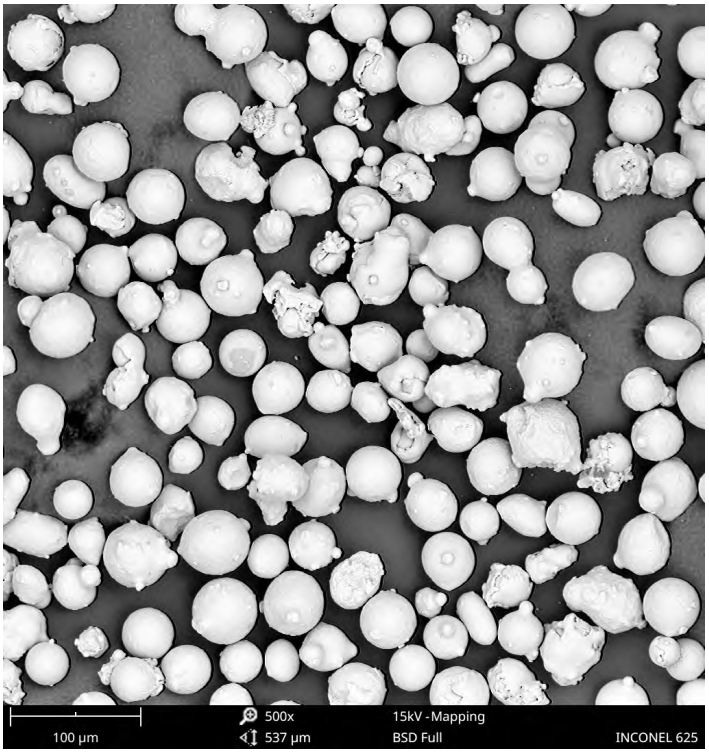

FIGURE 3.4: SEM micrograph showing the morphology of IN625 powder.

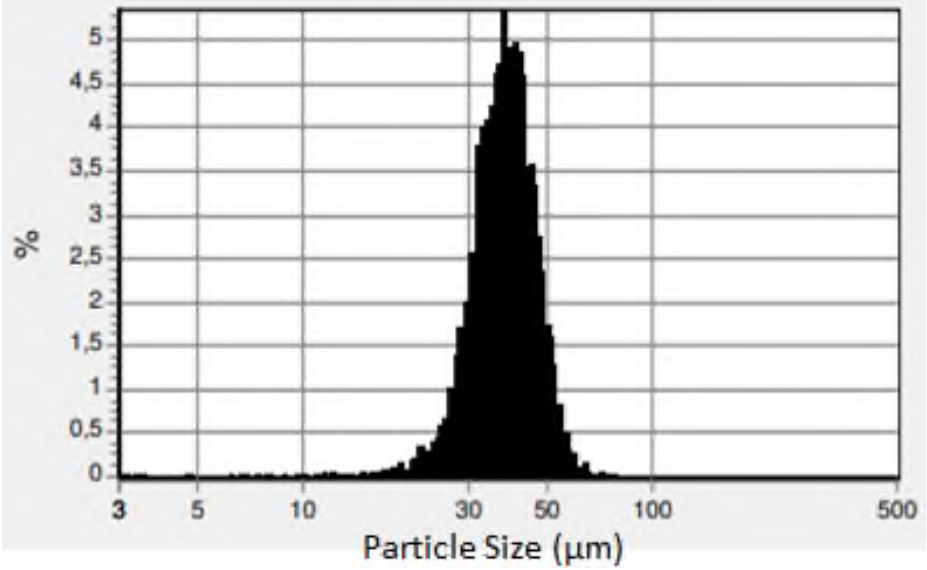

FIGURE 3.5: Particle size distribution (PSD) of IN625 powder.

TABLE 3.2: Statistical analysis of the IN625 powder, size in μm.

Count	9615	Number	Percentiles	Area	Percentiles	Volume	Percentiles
Minimum	3.0	10%	28.1	10%	31.4	10%	32.7
Maximum	105	25%	32.4	25%	35.5	25%	37.0
Mean	37.6	50%	37.4	50%	40.5	50%	42.0
Std. dev.	8.3	75%	42.6	75%	46.0	75%	47.6
Mode	37.3	90%	47.7	90%	51.3	90%	53.2

The tracks were built into the machine chamber in an argon atmosphere with less than 0.1 percent oxygen to reduce oxidation during the processing.

TABLE 3.3: L-BPF processing parameters for printing single tracks.

Process Parameter	**Value**
Laser Power, P	300, 400 W
Scan Speed, v	500, 700, 900, 1100, 1300 mm/s
Layer Thickness, t	60, 90, 120, 150 μm

3.2.1 Characterization of Tracks Top Views

The top views of the tracks were analyzed using a stereoscope ZEISS SteREO Discovery.V8 (Figure 3.6) at 10x magnification, followed by qualitative assessment and rating. This analysis aids in a rapid visualization of infeasible sets of parameters with obvious defects.

3.2.2 Characterization of Tracks Cross-sections

Using an electronic discharge machine (EDM), the single tracks were sectioned in the middle along the build direction. Then, using standard metallographic techniques, the sectioned samples were mounted, ground using SiC abrasive papers

FIGURE 3.6: Stereoscope ZEISS SteREO Discovery.V8 used for analysis the top views of the tracks.

with meshes of 320, 600, 800, 1200, and 2400, polished with diamond suspensions of 6, 3, and 1 µm, respectively. Finally, the samples were chemically etched with Kalling's No.2 reagent (hydrochloric acid + cupric chloride + 95% ethyl alcohol + distilled water) to make the geometrical and dimensional features microscopically visible. The cross-sections of the tracks were examined using an optical microscope Zeiss Axio Imager M2m (Figure 3.7) provided with a software Zeiss AxioVision SE64. As a result, the melt pool geometry and visible defects were revealed, and the material response to a specific set of parameters was inferred.

In addition, the melt pool width was measured to calculate the hatch distance, as shown in Equation 3.1.

$$x = (1 - \frac{h}{w}) \qquad \Longrightarrow \qquad h = w \times (1 - x) \tag{3.1}$$

Where: x represents the overlap, w melt pool width, and h the hatch distance.

FIGURE 3.7: Optical microscope Zeiss Axio Imager M2m.

3.3 Printing of Cubes

Based on the results of single tracks (top views and cross-sections), the process windows were estimated. Accordingly, cubes with dimensions of $10 \times 10 \times 10\ mm^3$ were printed. The processing parameters and scanning strategy (chessboard) used are displaced in Table 3.4 and Figure 3.8, respectively.

TABLE 3.4: L-BPF processing parameters for printing the cubes.

Process Parameter	**Value**
Laser Power, P	400 W
Scan Speed, v	700, 900, 1100, 1300 mm/s
Layer Thickness, t	60, 90, 120, 150 μm
Overlap	10, 20, 30%

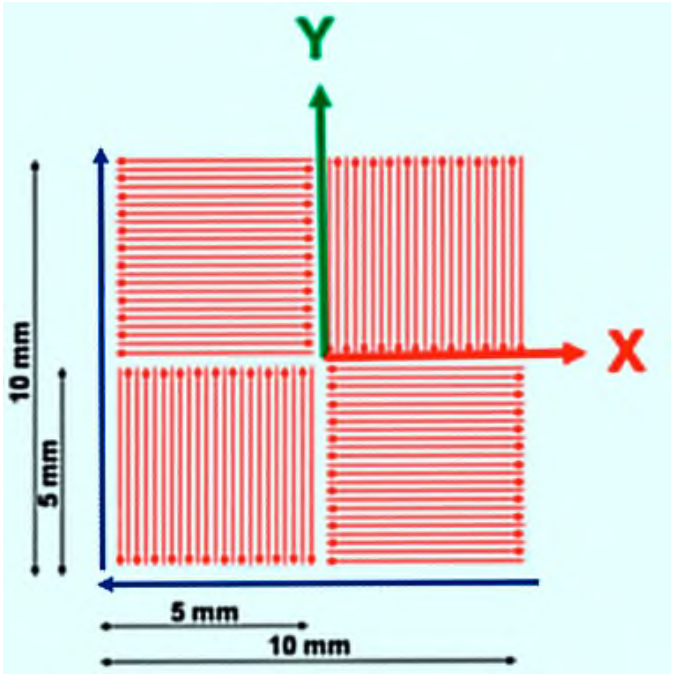

FIGURE 3.8: Chessboard scanning strategy used for printing IN625 cubes by L-PBF.

3.4 Density Measurements

The density of the cubes was measured using two different methods: Archimedes and image analysis. Applying the Archimedes principle, the mass of each cube was measured in air (m_a) and then in fluid (m_f) using an electrical balance with a resolution of $\pm$ 0.1 mg, as shown in Figure 3.9.

At room temperature, ethanol has a lower surface tension (22.10 mN/m) than deionized water, which has a high surface tension (72.75 mN/m). As a result, it is preferable to use ethanol as fluid rather than water because it forms fewer air bubbles when it penetrates the pores of the cube [109]. When using water, large amounts of unwanted air bubbles can significantly affect density measurement, resulting in lower density values. At least three measurements for each cube were carried out.

FIGURE 3.9: Digital electronic balance used for measuring the density.

The density of printed part (ρ_p) can be calculated using the following equation [109]:

$$\rho_p = (\rho_f - \rho_a)\,\frac{m_a}{m_a - m_f} + \rho_a \tag{3.2}$$

Where ρ_f is the fluid density, which varies with temperature. Therefore, a thermometer is placed into the fluid loaded in a becker inside the balance to measure the temperature. The fluid is ethanol as mentioned above; its density used for calculation is 0.79 g/cm^3. ρ_a is the air density which equals to 0.00119 g/cm^3, m_a is mass of the part in air, m_f mass of the part in the fluid, ρ_b is the bulk density of IN625, $\rho_b = 8.44\ g/cm^3$.

The relative density (RD) of the printed part can be calculated as:

$$RD = \frac{\rho_p}{\rho_b} \tag{3.3}$$

The density of the samples was also measured using an image analysis method. Using standard metallographic techniques, the samples were cross-sectioned along the build direction, ground, and polished. The porosity was measured using an optical microscope (Zeiss Axio Imager M2m) and image software (Axio Vision SE64 V4.9), which counts the number of black dots (pores) as a function of the base image colour (white, for example). At least 25 different images from each sample were analyzed at 100x magnification. Three samples from each set were considered (at least 75 images), and the density of these samples was averaged.

3.5 Metallographic Preparation

The printed samples were cut along the build direction via wire-cut EDM. The samples were then prepared using standard metallographic techniques. They were ground using SiC abrasive papers with meshes of 320, 600, 800, 1200, and 2400, then polished with diamond suspensions of 6, 3, and 1 µm, respectively. Furthermore, the samples were chemically etched with Kalling's No.2 reagent (hydrochloric acid + cupric chloride + 95% ethyl alcohol + distilled water) for microstructural characterization . An optical microscope (Zeiss Axio Imager M2m), a field emission scanning electron microscope (JEOL™ JSM-6701F) were used for investigation.

3.6 Hardness Measurements

The hardness of a material is a measure of its resistance to localized plastic deformation. It is determined by pressing a small indenter into the surface of the material being tested under controlled load and time conditions. The depth or size of the resulting indentation is measured and linked to a hardness number [101]. Vickers hardness testing was carried out conforming to ASTM E384 standard [110] on the prepared cross-section of each cube under a load of 0.5 kg_f for a dwell time of 15 *sec*, using a hardness tester (402MVD Knoop/Vickers Tester), Wilson Instruments. Ten hardness indentations were made and the average of which was used.

Chapter 4

RESULTS AND DISCUSSION

This chapter discusses the results of IN625 manufactured by L-PBF process, which are divided into three phases:

- **Phase 1:** characterizes the single tracks to define the process window.
- **Phase 2:** deals with the relative density and its modelling to estimate the best processing parameters for optimizing relative density and productivity.
- **Phase 3:** validates the estimated parameters from **Phase 2** by printing additional 24 cubes and evaluating relative density, productivity, hardness, and microstructure of the new cubes.

4.1 Single Tracks Characterization

Single track refers to laser scanning a single line in the powder bed. Single tracks are created by melting metal powder with a defined thickness spread on a substrate, creating a uniform melt pool, and solidifying together. The thickness of the powder layer appears hard to be uniform on the substrate. It may vary slightly depending on the substrate surface roughness and the powder packing density. The nature and geometry of the melt pool are determined by the processing parameters used, such as laser power, scan speed, and layer thickness. As a result, the single track characterization (top view and cross-section) provides a quick and easy way to define the process window in which the melt pool is stable.

4.1.1 Top Views of Single Tracks

Single track scan can be classified from the top view as follows [43]:

1. Stable:
   - Continuous and uniform along its length.

2. Transitional:
   - Continuous but exhibits some irregularities or necking.
   - Continuous but shows narrowing and expanding spots.

3. Unstable:
   - Track with a chain of beads (balling).
   - Track with cracks.

For a scan track to be stable, the following requirements should be met:

I. The track must be uniform and continuous along its length to prevent the possibility of any pores in the printed part.

II. The track must penetrate the previous layer slightly to bond well between the subsequent layers.

III. The track should display enough height to support the manufacturing of 3D parts, as illustrated in Figure 4.1.

IV. The connection angle between the scan track and the previous layer should be around 90° to ensure good dimensional accuracy and high density, as shown in Figure 4.1. However, larger angles demand a large overlap between adjacent tracks.

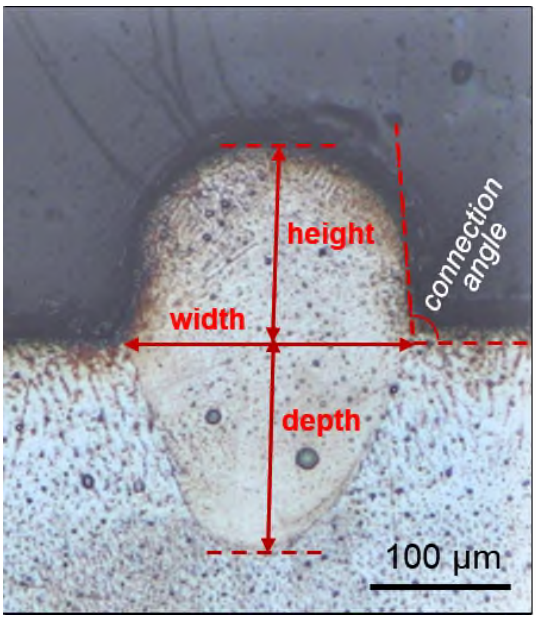

FIGURE 4.1: Track cross-section of IN625 processed with $P = 300\ W$, $v = 500\ mm/s$, and $t = 120\ \mu m$ showing the melt pool geometry.

The top views of IN625 tracks printed with layer thicknesses of 60, 90, 120, and 150 μm and scan speeds of 500, 700, 900, 1100 and 1300 mm/s are shown in Figures 4.2, 4.4, 4.6, and 4.8 for $P = 300\ W$, and in Figures 4.3, 4.5, 4.7, and 4.9 for $P = 400\ W$.

The tracks formed with a powder layer thickness of 60 μm and laser powers of 300 and 400 W are shown in Figures 4.2 and 4.3. The tracks are continuous at scan speeds of 500 and 700 mm/s, but their shape shifts to a transition mode at scan speeds between 900 and 1300 mm/s. In this mode, the tracks become irregular with some narrowing and expanding spots. This can be attributed to the lower input energy when compared to that supplied with a scan speed of 500 mm/s.

At a constant laser power of 400 W, for example, the estimated input surface energy is about 5 J/mm^2 at 1300 mm/s, while it is 13 J/mm^2 at 500 mm/s, a factor of 2.6 higher. As a result of the higher input energy at 500 mm/s, it is expected that the melt pool will penetrate sufficiently into the substrate, which will have an additional positive impact on the formation of continuous tracks.

Heat conduction causes the melt pool to penetrate the substrate when the laser energy density is sufficient to melt the powder particles. The track is stable, continuous, and uniform in this mode. According to Yadroitsev et al. [43], the stable melt pool has a semi-spherical shape with a depth-to-width aspect ratio of no more than 1:2.

However, for greater layer thicknesses and faster scan speeds (for example, $P = 300\ W$, $t = 150\ \mu m$, $v = 900, 1100, 1300\ mm/s$), Figure 4.8 (c-e), the laser energy absorbed by the powder is very low and there is less time for heating, resulting

in only a small amount of powder being melted. Because of the low melt pool temperature, flowability and wettability are poor, and a non-continuous melt track is expected.

Furthermore, thicker layers may cause a large melt pool to settle far from the substrate, resulting in a relatively small contact area between the melt pool and the substrate. As a result, the small wetting area cannot support a large melt pool, and the melt pool becomes unstable and splits into isolated, smaller droplets before solidifying into discontinuous metal beads. [26, 43, 46, 54, 111]. In this case, the track mode shifts from transition to balling, as shown in Figure 4.4 (e) or in Figure 4.8 (c-e).

The processing maps based on the observation of tracks top views are presented in Figure 4.10 (a) for a laser power of 300 W and in Figure 4.10 (b) for a laser power of 400 W. The red area denotes the stable region where the processing parameters for printing the cubes can be estimated. Because of the narrower red area (process window) at 300 W laser power, this power was not used in printing the cubes.

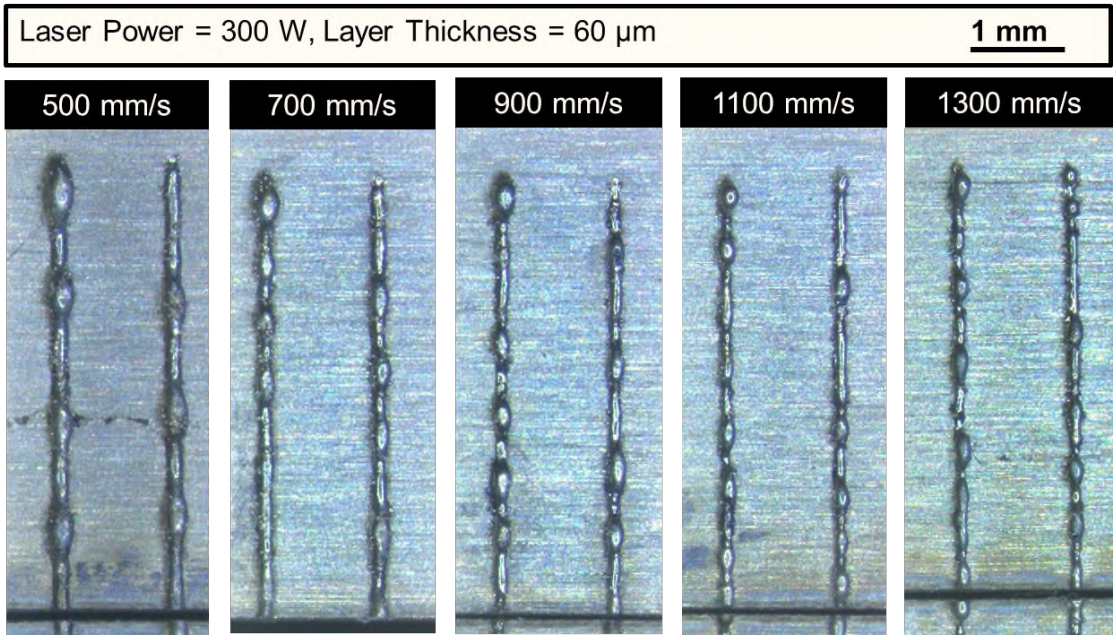

FIGURE 4.2: L-PBF IN625, top views of single tracks printed with: $P = 300\ W$, $t = 60\ \mu m$, and $v = 500, 700, 900, 1100, 1300\ mm/s$.

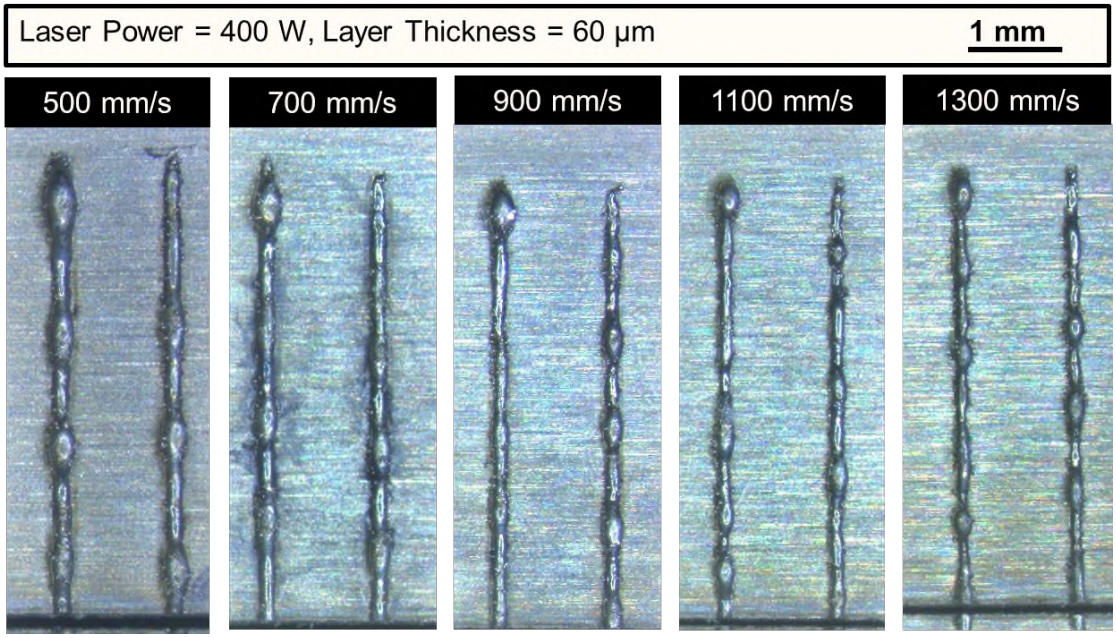

FIGURE 4.3: L-PBF IN625, top views of single tracks printed with: $P = 400\ W$, $t = 60\ \mu m$, and $v = 500, 700, 900, 1100, 1300\ mm/s$.

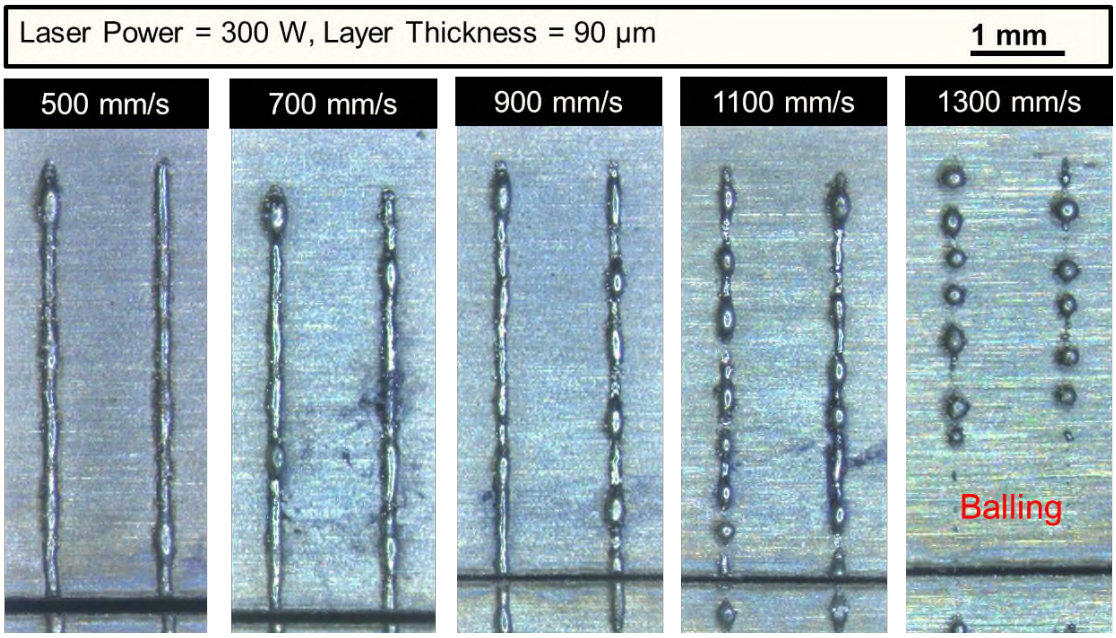

FIGURE 4.4: L-PBF IN625, top views of single tracks printed with: $P = 300\ W$, $t = 90\ \mu m$, and $v = 500, 700, 900, 1100, 1300\ mm/s$.

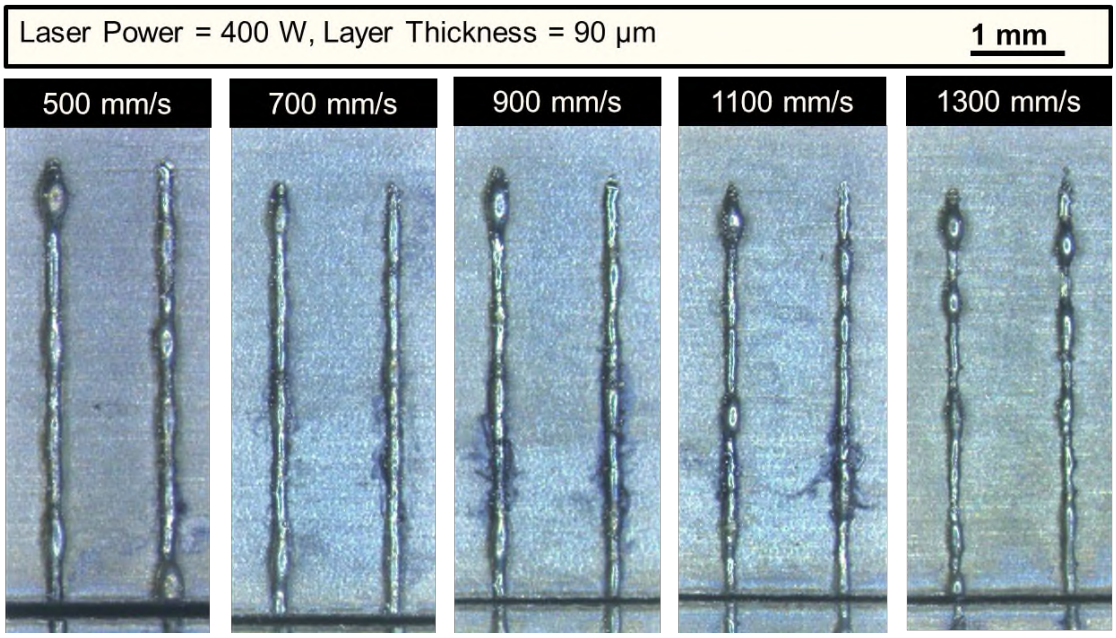

FIGURE 4.5: L-PBF IN625, top views of single tracks printed with: $P = 400\ W$, $t = 90\ \mu m$, and $v = 500, 700, 900, 1100, 1300\ mm/s$.

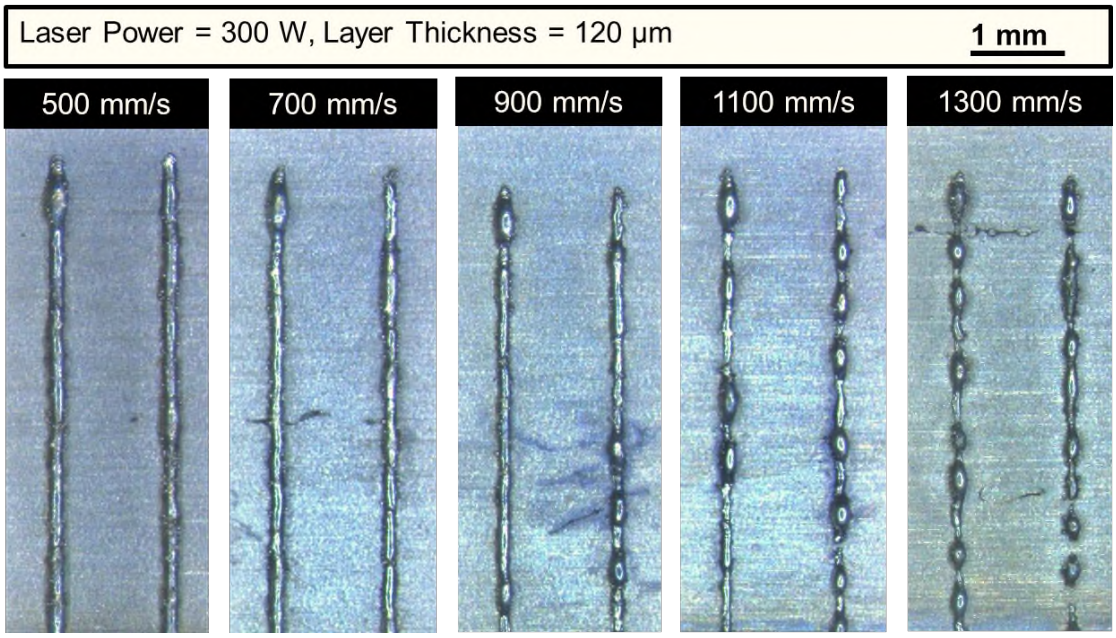

FIGURE 4.6: L-PBF IN625, top views of single tracks printed with: $P = 300\ W$, $t = 120\ \mu m$ and $v = 500, 700, 900, 1100, 1300\ mm/s$.

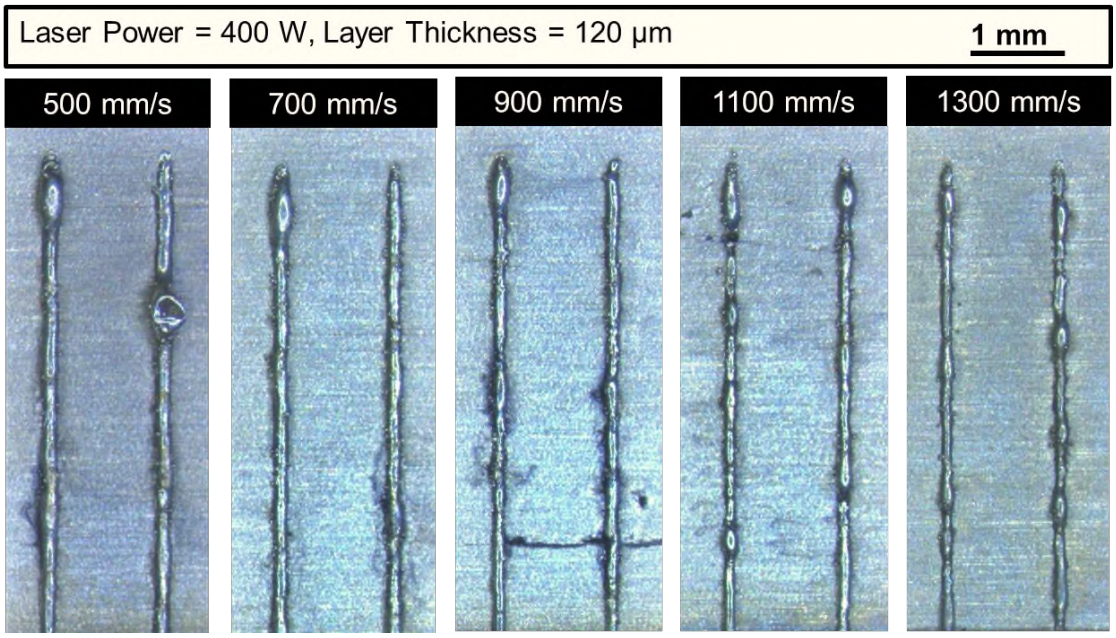

FIGURE 4.7: L-PBF IN625, top views of single tracks printed with: $P = 400\ W$, $t = 120\ \mu m$, and $v = 500, 700, 900, 1100, 1300\ mm/s$.

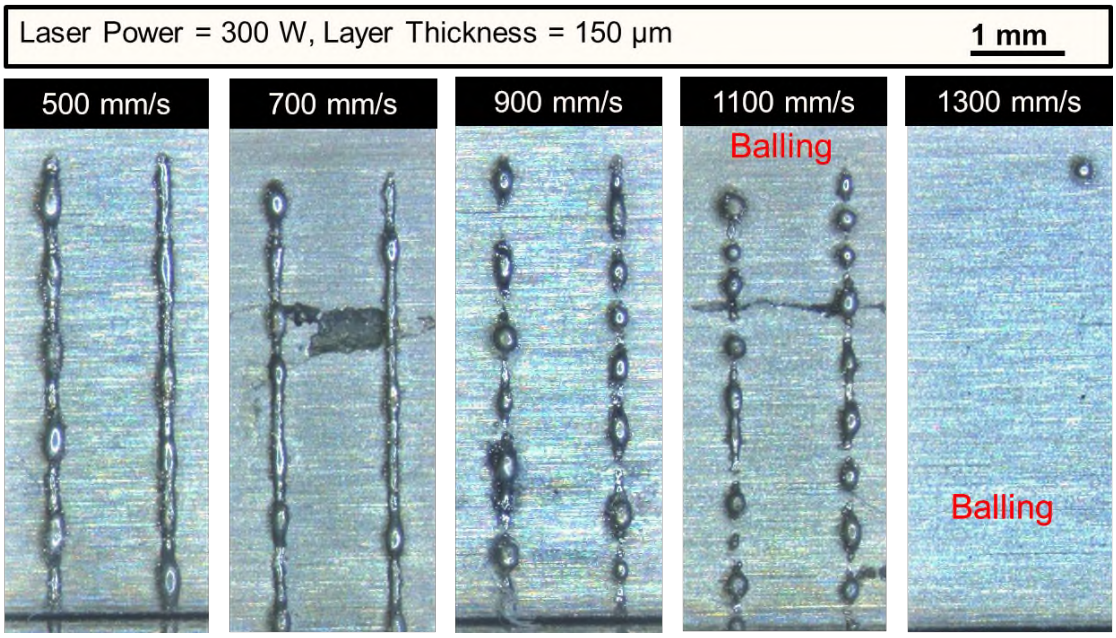

FIGURE 4.8: L-PBF IN625, top views of single tracks printed with: $P = 300\ W$, $t = 150\ \mu m$, and $v = 500, 700, 900, 1100, 1300\ mm/s$.

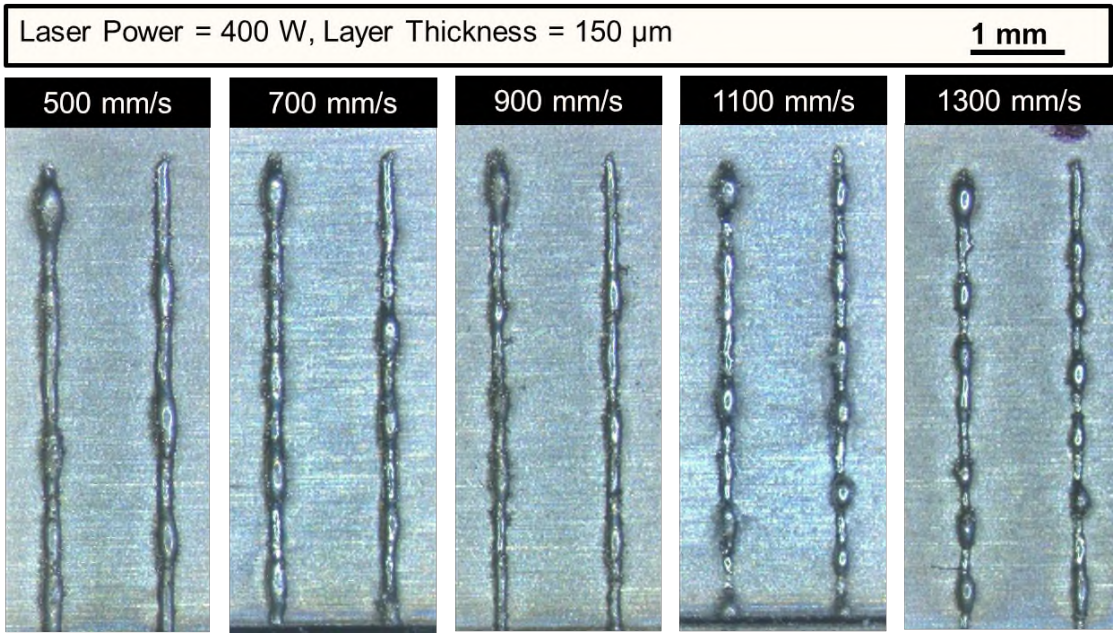

FIGURE 4.9: L-PBF IN625, top views of single tracks printed with: $P = 400\ W$, $t = 150\ \mu m$, and $v = 500, 700, 900, 1100, 1300\ mm/s$.

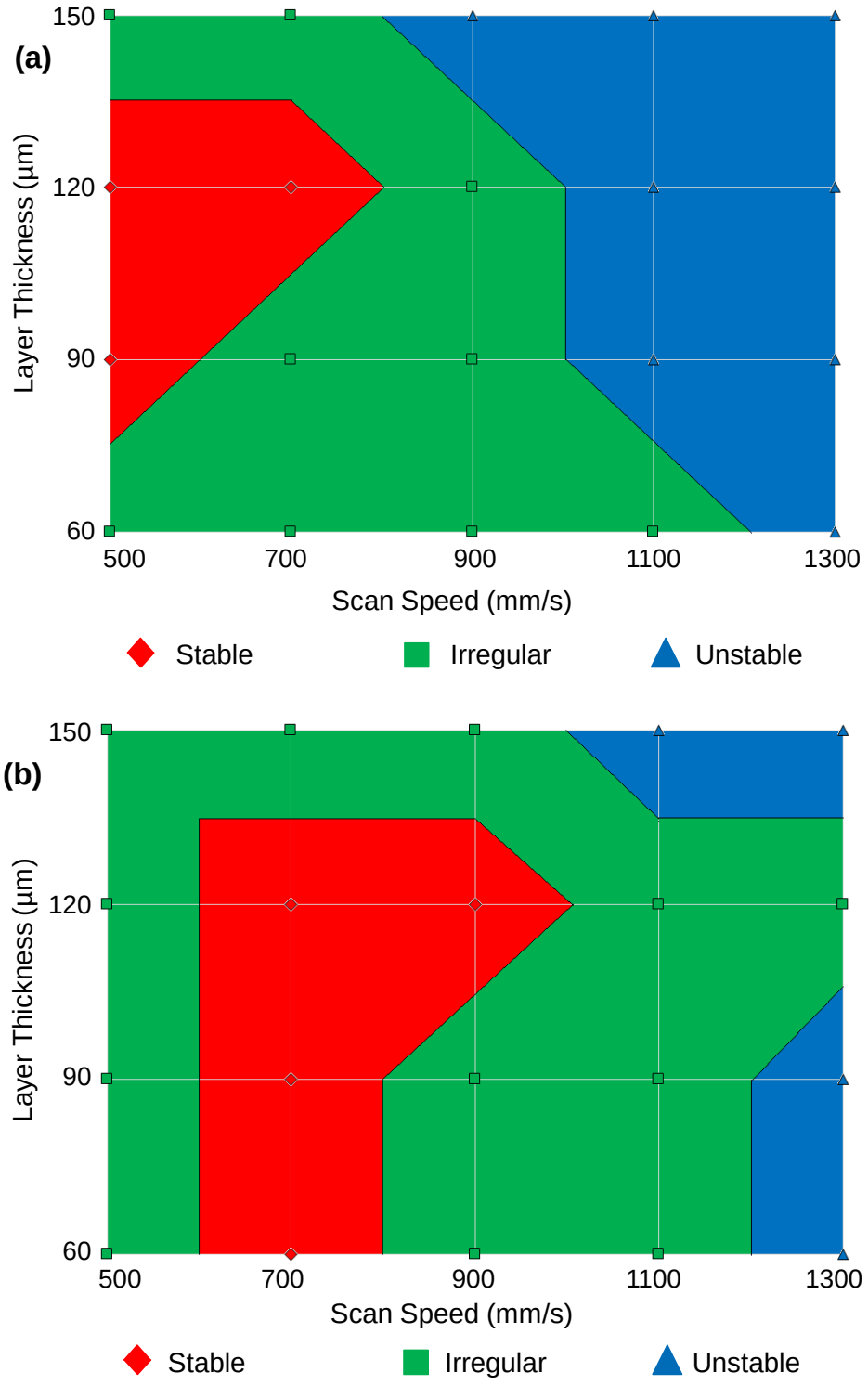

FIGURE 4.10: L-PBF IN625 processing map based on observation of tracks top views to estimate the printing parameters for cubes, (a) $P = 300\ W$ and (b) $P = 400\ W$.

4.1.2 Cross-Sections of Single Tracks

The cross-sections of IN625 tracks printed with layer thicknesses of 60, 90, 120, and 150 μm, and laser scan speeds of 500, 700, 900, 1100 and 1300 mm/s are presented in Figures 4.11, 4.13, 4.15, and 4.17 for a laser power of 300 W, and in Figures 4.12, 4.14, 4.16, and 4.18 for a laser power of 400 W.

It can be demonstrated that increasing the scan speed from 500 to 1300 mm/s for a constant laser power of 300 W or 400 W tends to reduce the melt pool width and depth. The powder layer thickness influences the melt pool dimensions; the largest dimensions were measured with a layer thickness of 60 μm, and the smallest with 150 μm. In some scenarios, no tracks were generated due to insufficient input energy delivered to the powder, as observed in Figure 4.13 (e) and Figure 4.17 (e).

On the other hand, reducing the scan speed increases the laser energy density and interaction time. As a result, the melt pool sinks into the substrate, and the transition mode is attained. Then, as the energy density increases significantly due to a combination of lower scan speed and higher laser power, more heat is expected to be transferred to the powder bed, resulting in greater melt pool penetration into the substrate. In this case, the track scan mode shifts from transition to keyhole mode, as shown in Figure 4.18 (a). The higher temperature causes substantial vaporization of alloying elements. This vaporization results in a recoil pressure acting on the melt pool that pushes the melt to the sides and allows the laser to penetrate deeply into the underlying material [90, 93, 116]. Because keyhole mode causes extensive porosity, it is unsuitable for manufacturing 3D parts [90, 93, 113].

Furthermore, the processing maps based on the observation of track cross-sections are presented in Figure 4.19 (a) for a laser power of 300 W and in Figure 4.19 (b) for a laser power of 400 W. The red area denotes the stable region where the processing parameters for printing the cubes can be estimated. Due to the narrower red area (process window) at the laser power of 300 W, this power was not used for printing the cubes.

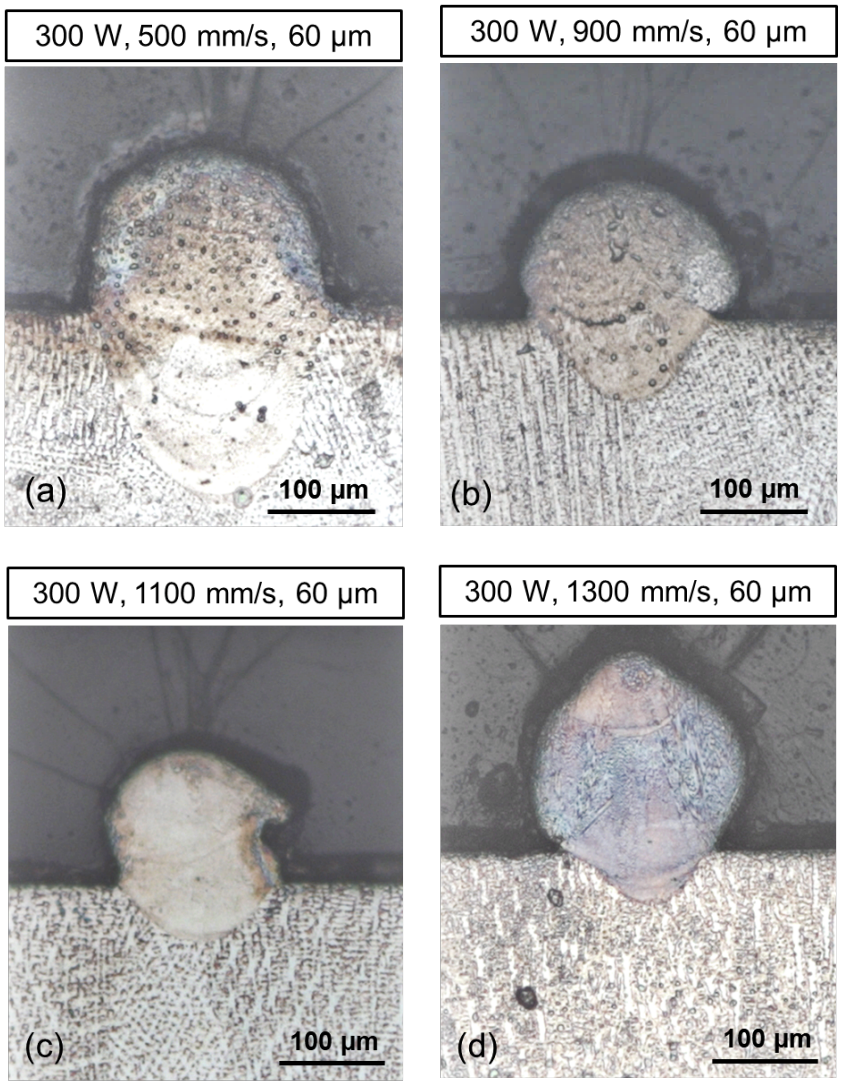

FIGURE 4.11: L-PBF IN625, cross-sections of single tracks printed with $t = 60\ \mu m$, $P = 300\ W$, and $v = 500, 900, 1100, 1300\ mm/s$.

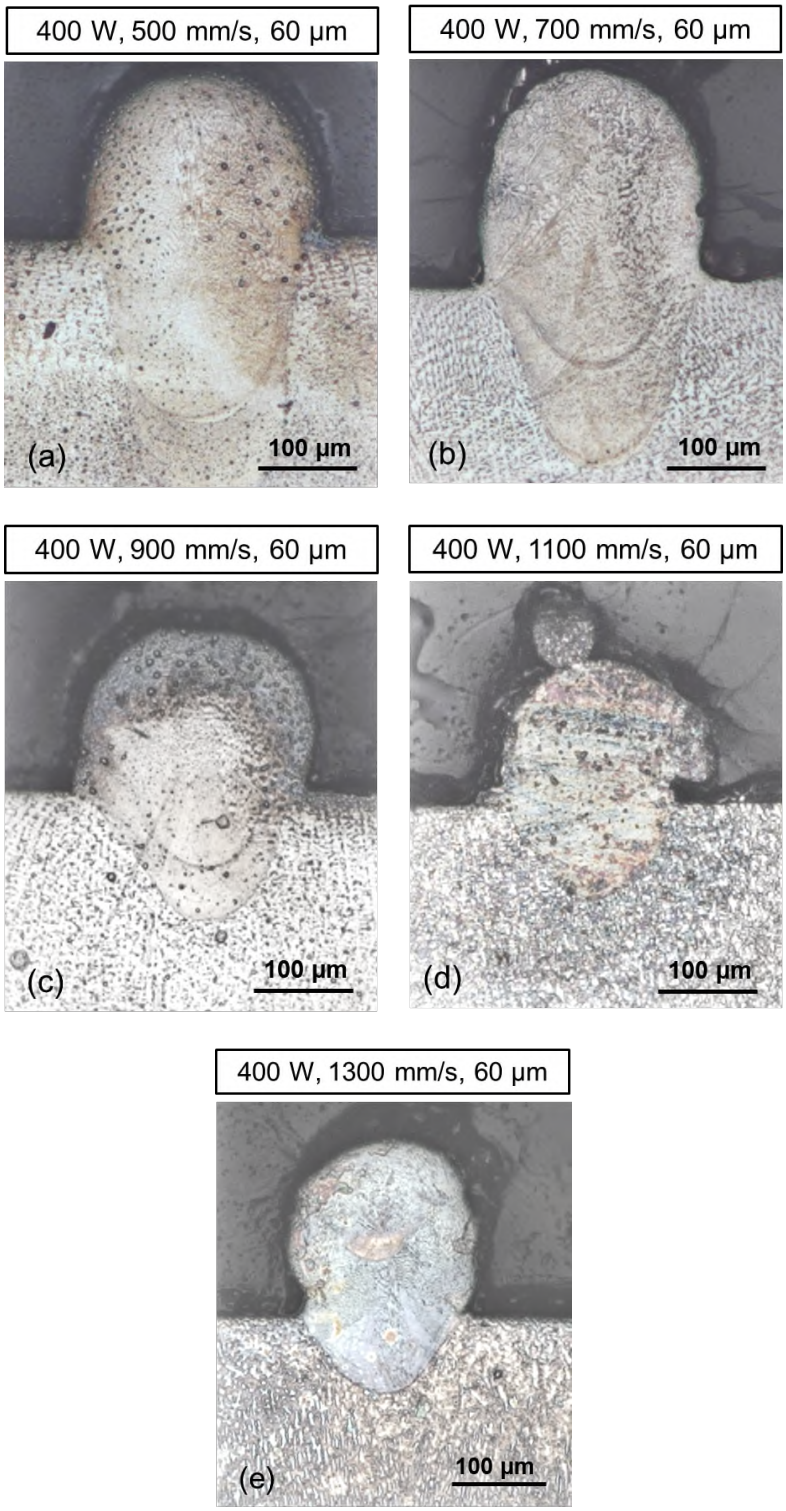

FIGURE 4.12: L-PBF IN625, cross-sections of single tracks printed with $t = 60\ \mu m$, $P = 400\ W$, and $v = 500, 700, 900, 1100, 1300\ mm/s$.

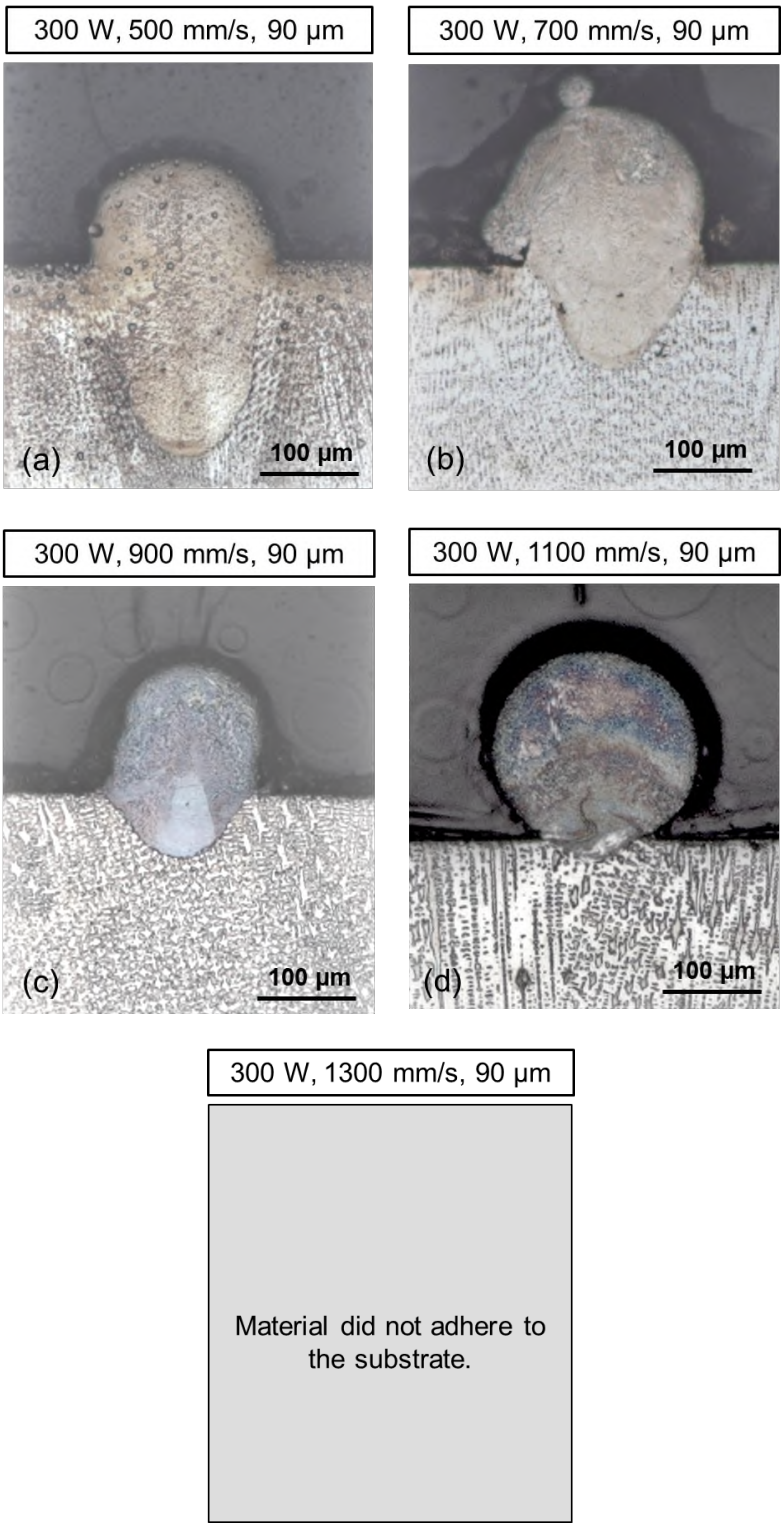

FIGURE 4.13: L-PBF IN625, cross-sections of single tracks printed with $t = 90\ \mu m$, $P = 300\ W$, and $v = 500, 700, 900, 1100, 1300\ mm/s$.

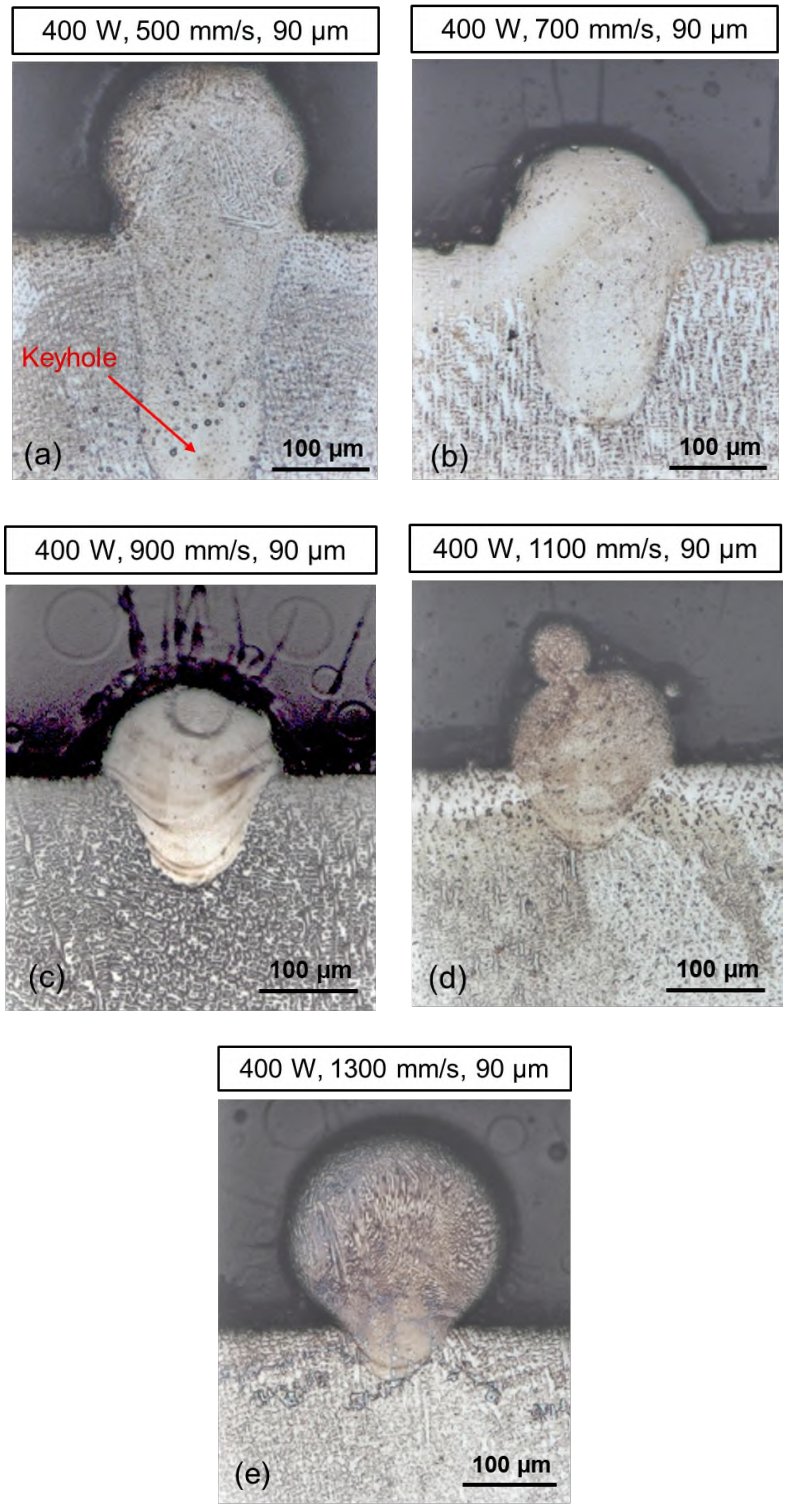

FIGURE 4.14: L-PBF IN625, cross-sections of single tracks printed with $t = 90\ \mu m$, $P = 400\ W$, and $v = 500, 700, 900, 1100, 1300\ mm/s$.

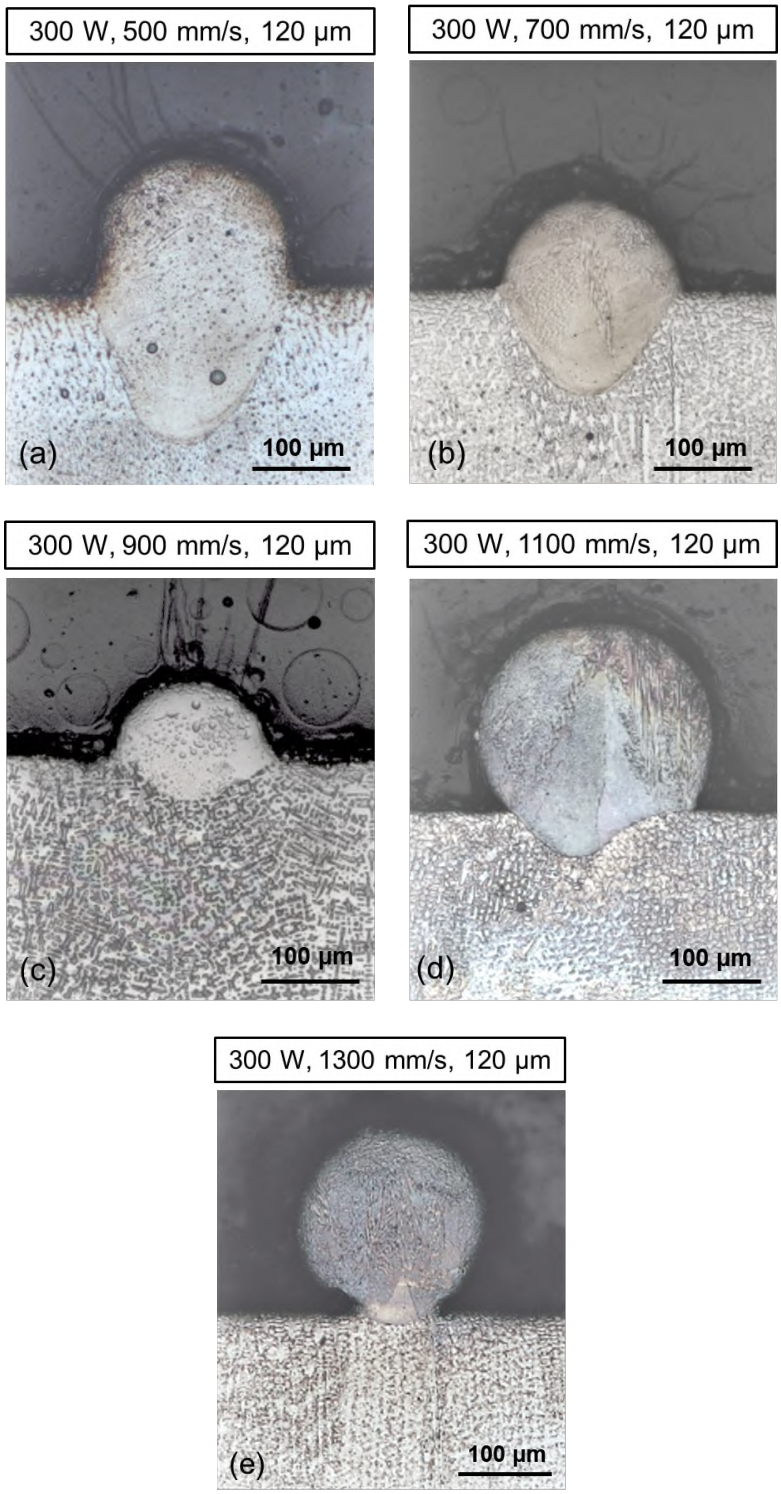

FIGURE 4.15: L-PBF IN625, cross-sections of single tracks printed with $t = 120\ \mu m$, $P = 300\ W$, and $v = 500, 700, 900, 1100, 1300\ mm/s$.

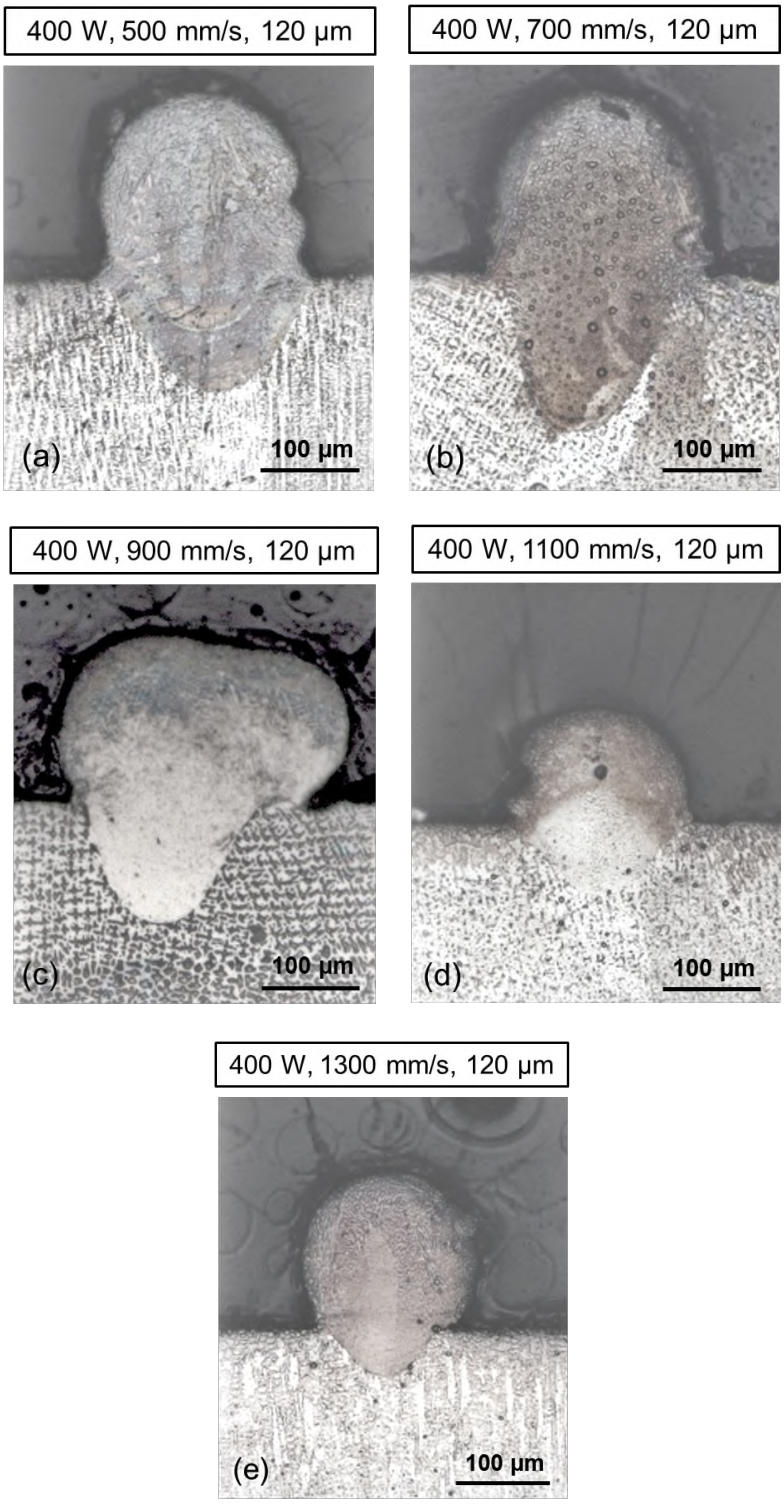

FIGURE 4.16: L-PBF IN625, cross-sections of single tracks printed with $t = 120\ \mu m$, $P = 400\ W$, and $v = 500, 700, 900, 1100, 1300\ mm/s$.

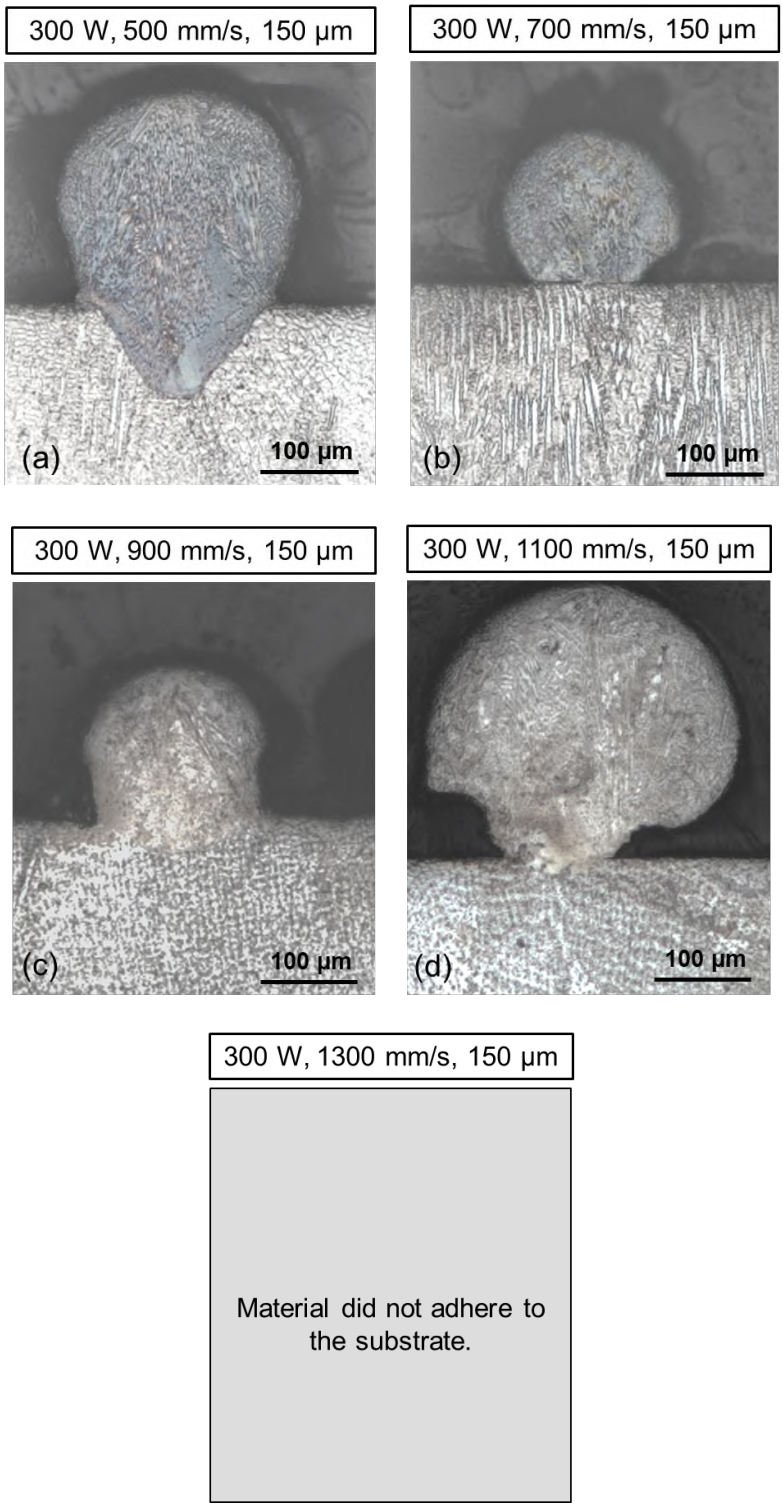

FIGURE 4.17: L-PBF IN625, cross-sections of single tracks printed with $t = 150\ \mu m$, $P = 300\ W$, and $v = 500, 700, 900, 1100, 1300\ mm/s$.

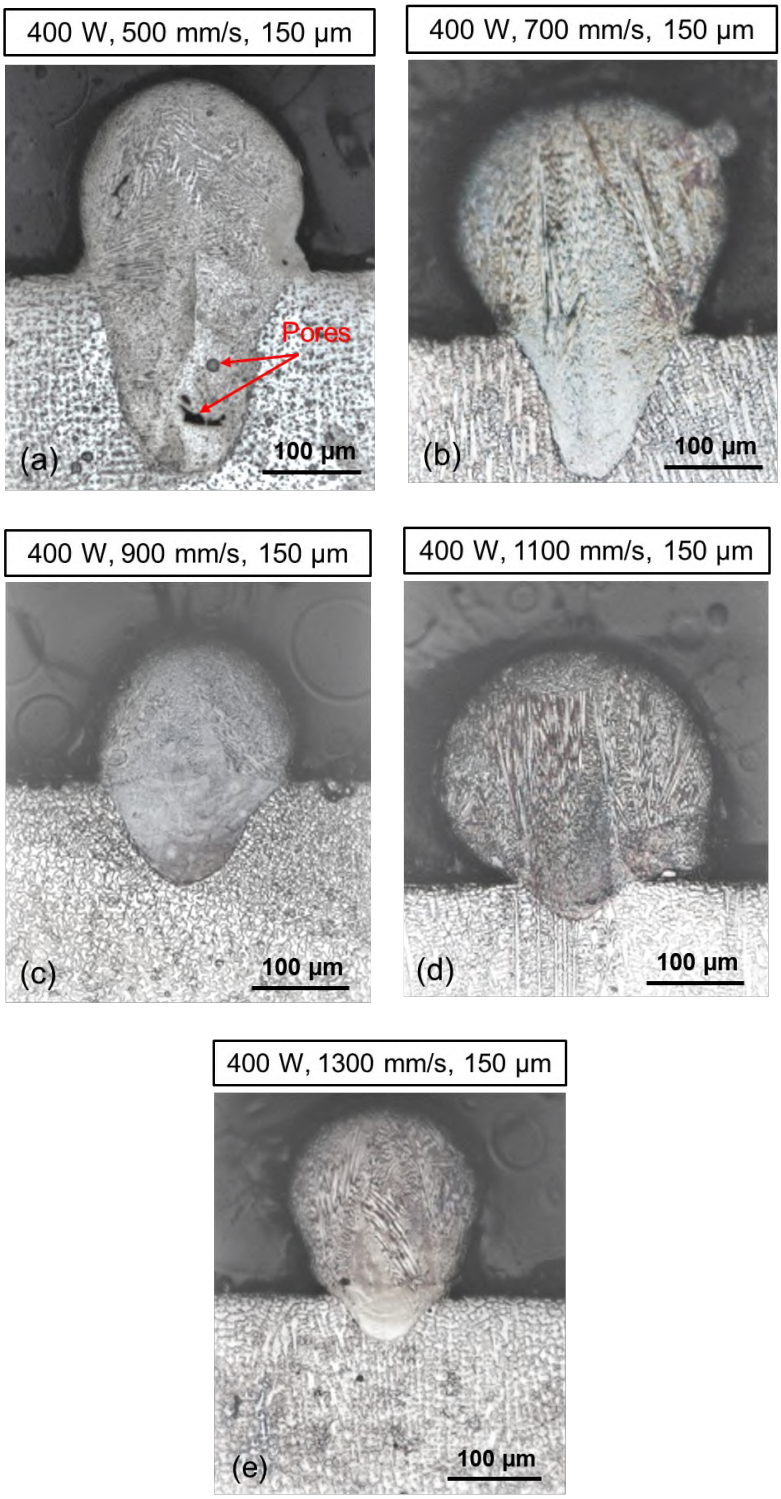

FIGURE 4.18: L-PBF IN625, cross-sections of single tracks printed with $t = 150\ \mu m$, $P = 400\ W$, and $v = 500, 700, 900, 1100, 1300\ mm/s$.

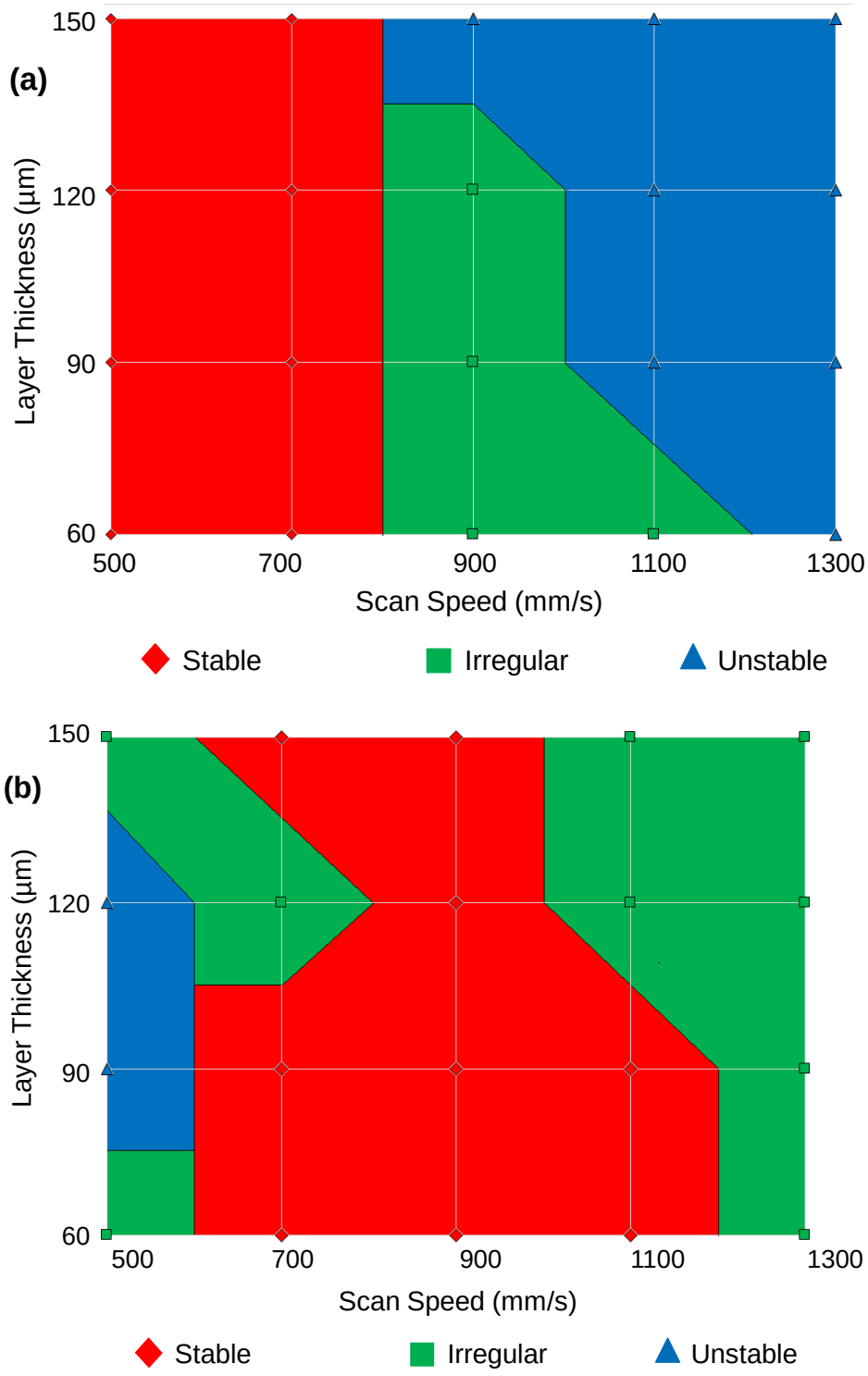

FIGURE 4.19: L-PBF IN625 processing map based on observation of tracks cross-sections to estimate the printing parameters for cubes, (a) $P = 300\ W$ and (b) $P = 400\ W$.

4.1.2.1 Effect of Scan Speed on Melt Pool Width

Figure 4.20 depicts the effect of laser scan speed on melt pool width. When the scan speed is increased, the melt pool width decreases for all layer thicknesses tested. These results are expected because the laser energy density decreases with increasing scan speed. Table 4.1 shows the raw data of melt pool width for different layer thicknesses and scan speeds.

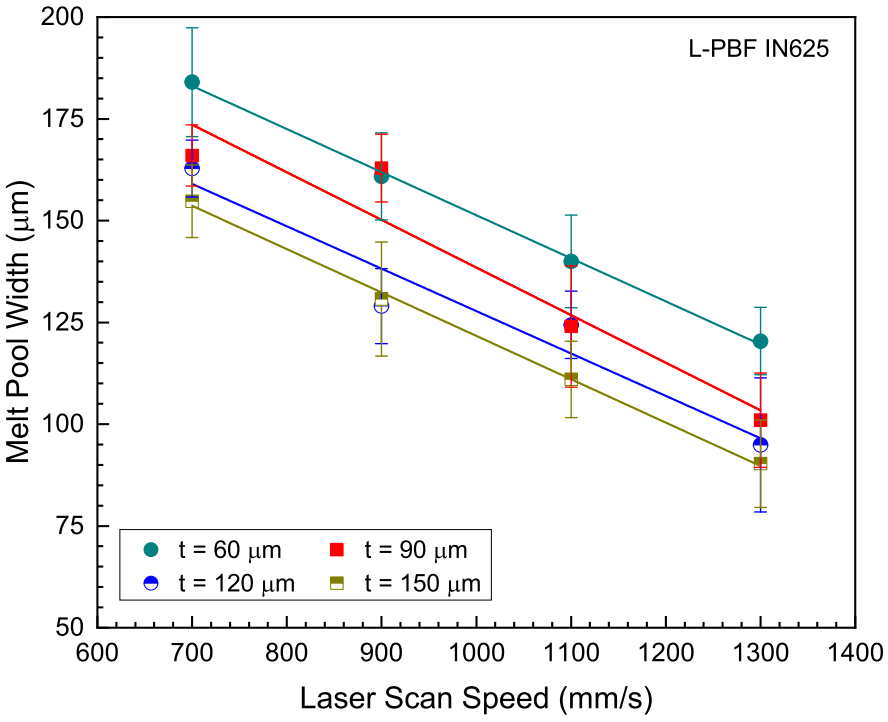

FIGURE 4.20: L-PBF IN625, effect of laser scan speed on the melt pool width for varying powder layer thicknesses at constant laser power of 400 W.

The melt pool width in the figure above is affected by two independent parameters (scan speed and powder layer thickness). Multiple linear regression statistical analysis was used to determine which of these two parameters is the most significant and has the greatest impact on the melt pool width.

TABLE 4.1: L-PBF IN625; raw data of melt pool width, w in μm; layer thickness, t in μm; scan speed, v in mm/s; and laser power, $P = 400\ W$.

t	v	w_1	w_2	w_3	w_4	w_5	w_6	w_7	w_8	w_9	Mean	SD
60	700	179.05	210.11	173.87	179.56	180.92	196.48	163.43	186.66	186.18	184.03	13.36
60	900	147.27	153.72	160.87	156.95	151.81	155.66	173.77	178.29	169.90	160.92	10.68
60	1100	130.02	129.83	150.50	131.82	132.42	158.92	154.38	137.59	135.09	140.06	11.36
60	1300	124.66	111.76	126.60	106.58	116.91	117.55	123.37	121.44	134.35	120.36	8.27
90	700	159.54	165.38	156.32	162.13	154.37	176.98	156.96	167.30	166.00	162.78	7.04
90	900	123.37	138.24	127.24	128.54	122.12	133.78	111.77	133.70	142.12	128.99	9.23
90	1100	119.50	113.03	122.08	119.55	142.78	125.95	129.83	122.72	124.02	124.38	8.33
90	1300	104.00	96.60	109.82	106.60	78.81	104.00	91.73	103.36	58.79	94.86	16.48
120	700	170.52	167.93	169.24	173.75	156.31	163.44	153.72	175.76	164.12	166.09	7.46
120	900	162.13	156.39	150.54	180.87	166.77	162.12	161.51	160.23	165.36	162.89	8.29
120	1100	139.52	156.33	121.44	116.99	114.34	124.02	107.87	115.62	120.80	124.11	14.90
120	1300	93.66	102.70	113.78	106.62	98.82	122.72	93.07	93.02	85.91	101.15	11.63
150	700	136.28	155.66	155.67	160.18	165.39	155.67	160.19	148.57	154.7	154.70	8.32
150	500	186.67	174.4	173.11	187.31	175.05	170.56	172.47	195.10	149.86	176.06	12.96
150	900	126.60	117.56	147.27	155.67	127.89	124.02	111.12	128.53	137.58	130.69	14.03
150	1300	104.64	88.49	81.48	74.95	94.36	93.03	81.41	87.26	107.22	90.32	10.73

Equation 4.1 depicts the best model for describing the melt pool width.

$$w = 262.96 - 0.103\ v - 0.237\ t \tag{4.1}$$

Where w represents the melt pool width in μm, v the scan speed in mm/s, and t represents the powder layer thickness in μm.

Table 4.2 displays the statistical analysis of the estimated model parameters. The table shows that the estimated model parameters (v and t) using ordinary least squares (OLS) are statistically significant at the 0.05 level of significance because the p-values are less than the level of significance.

TABLE 4.2: Statistical analysis of the estimated model parameters.

Parameter	Estimate	Standard Error	t-value	p-value
Intercept	262.9593	14.8306	17.73085	<0.001
v	−0.10284	0.01144	−8.99267	<0.001
t	−0.23751	0.08127	−2.92263	0.01188

The most significant parameter is the powder layer thickness (t), which has a larger factor (-0.23751) than the scan speed (v). The negative sign indicates that increasing layer thickness while maintaining constant scan speed reduces melt pool width. Sun et al. [52] reported similar results for Ti6Al4V samples and Souza et al. [112] for maraging steel 300 built by L-PBF. The model is validated by plotting the predicted and measured melt pool width values, as illustrated in Figure 4.21. The high coefficient of correlation (R^2) indicates that the model proposed is reliable.

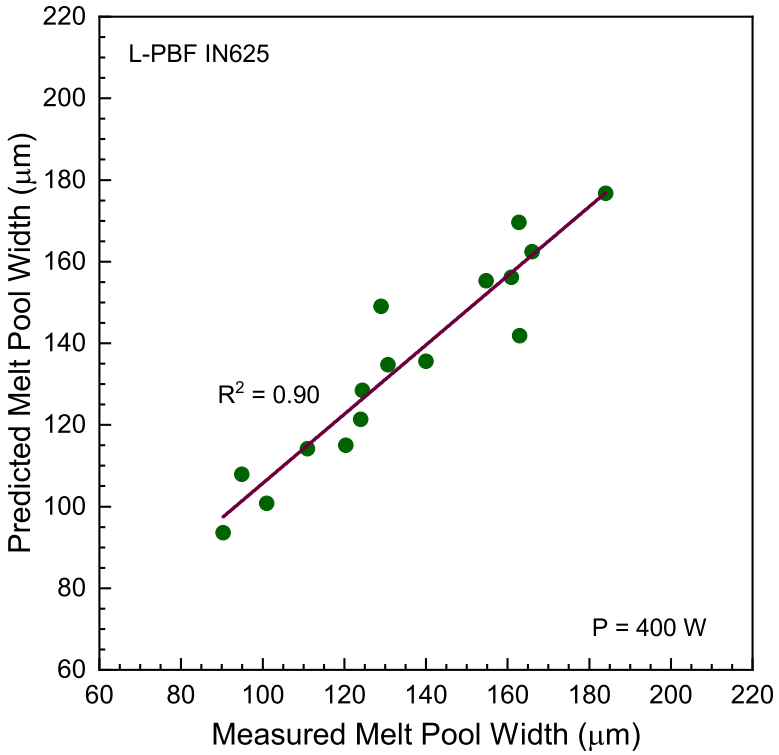

FIGURE 4.21: L-PBF IN625, predicted melt pool width versus measured melt pool width at constant laser power of 400 W.

4.1.2.2 Effect of Energy Density on Melt Pool Width

Figure 4.22 depicts the relationship between melt pool width and surface energy density. Equation 2.3, Section 2.5, Chapter 2, may be used to compute the surface

energy density, which normalizes the effects of laser power, scan speed, and layer thickness. The graph shows that increasing the surface energy density leads to a nonlinear increase in melt pool width. The results are expected because increasing surface energy density reflects in more heat transferred by the laser beam to the powder bed to melt more particles resulting in a larger melt pool.

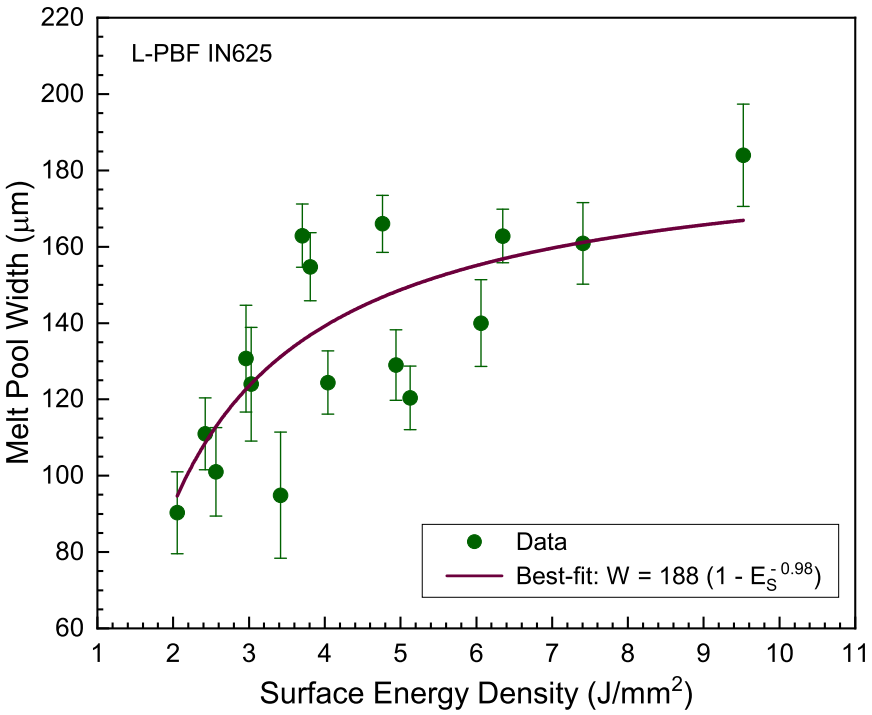

FIGURE 4.22: L-PBF IN625, effect of surface energy density on the melt pool width.

For example, a surface energy density of about 4.9 J/mm^2 ($P = 400\ W$, $v = 900\ mm/s$, and $t = 90\ \mu m$) results in a melt pool width of $129 \pm 9.2\ \mu m$, as shown in Figure 4.14 (c). By reducing the powder layer thickness from 90 to 60 μm while keeping both laser power and scan speed unchanged, the estimated surface energy density of about 7.4 J/mm^2 yields a melt pool width of $161 \pm 10.7\ \mu m$ (about 25% increase in track width), as shown in Figure 4.12 (c).

In addition, a nonlinear regression model, using Levenberg Marquardt iteration algorithm [114, 115], is adapted to define the relationship between melt pool width and surface energy density. The model used to fit the data is shown in Equation 4.2.

$$w = a\ (1 - E_S^{-b}) \tag{4.2}$$

where a and b are model parameters. The nonlinear regression analysis depicts that the best-fit model to the data is displayed in Equation 4.3.

$$w = 187.68\ (1 - E_S^{-0.98}) \tag{4.3}$$

where w represents the melt pool width in μm and E_S represents the surface energy density in J/mm^2.

Table 4.3 lists the statistical analysis of the estimated model parameters. The table shows that the model parameters (a and b), using ordinary least squares (OLS), are statistically significant at the 0.05 level of significance because the p-values are less than the level of significance.

TABLE 4.3: Statistical analysis of the estimated model parameters.

Parameter	Estimate	Standard Error	t-value	p-value
a	187.6788	30.0559	6.24433	<0.001
b	0.97662	0.35155	2.77801	0.0148

4.2 Relative Density

The process window for printing cubes to evaluate the relative density was identified based on the results of single track characterization. Accordingly, 48 cubes were printed using the process parameters listed in Table 4.4 and Figure 4.23 shows the printed cubes. Consequently, the effects of layer thickness, scan speed, surface energy density, and overlap on the relative density of the cubes were discussed in the following sections.

FIGURE 4.23: 48 IN625 cubes ($10 \times 10 \times 10\ mm^3$) printed with $P = 400\ W$, $v = 700, 900, 1100, 1300\ mm/s$, $t = 60, 90, 120, 150\ \mu m$, and overlap = 10, 30, 50%.

TABLE 4.4: L-PBF Process parameters for printing 48 cubes.

Sample No.	Laser Power P (W)	Scan Speed v (mm/s)	Thickness t (μm)	Overlap (%)
1	400	700	60	10
2	400	700	60	30
3	400	700	60	50
4	400	900	60	30
5	400	900	60	10
6	400	900	60	50
7	400	1100	60	10
8	400	1100	60	30
9	400	1100	60	50
10	400	1300	60	50
11	400	1300	60	30
12	400	1300	60	10
13	400	700	90	10
14	400	700	90	30
15	400	700	90	50
16	400	900	90	50
17	400	900	90	10
18	400	900	90	30
19	400	1100	90	30
20	400	1100	90	10
21	400	1100	90	50
22	400	1300	90	50
23	400	1300	90	30
24	400	1300	90	10
25	400	700	120	10
26	400	700	120	30
27	400	700	120	50
28	400	900	120	50
29	400	900	120	30
30	400	900	120	10
31	400	1100	120	50
32	400	1100	120	30
33	400	1100	120	10
34	400	1300	120	10
35	400	1300	120	30
36	400	1300	120	50
37	400	700	150	50
38	400	700	150	30
39	400	700	150	10
40	400	900	150	10
41	400	900	150	30
42	400	900	150	50
43	400	1100	150	50
44	400	1100	150	30
45	400	1100	150	10
46	400	1300	150	10
47	400	1300	150	30
48	400	1300	150	50

4.2.1 Effect of Layer Thickness

Figures 4.24 and 4.25 display in 2D and 3D, respectively, the relationship between relative density and layer thickness for 10% overlap and varying laser scan speeds. To improve visualization of the relative density data, the scaling was not the same for the overlaps used. The relative density scale ranges from 92, 96.8, and 98.8% to 100% for overlaps of 10, 30, and 50%, respectively. For all of the scan speeds and overlaps tested, the average relative density decreases as the layer thickness increases. The spread in relative density caused by the scan speeds decreases as the overlap increases. For 10% overlap, the relative density ranged from 99.58 to 99.16% at $t = 60\ \mu m$ and from 97.84 to 93.80% at 150 μm when the scan speed increased from 700 to 1300 mm/s, as shown in Figure 4.24.

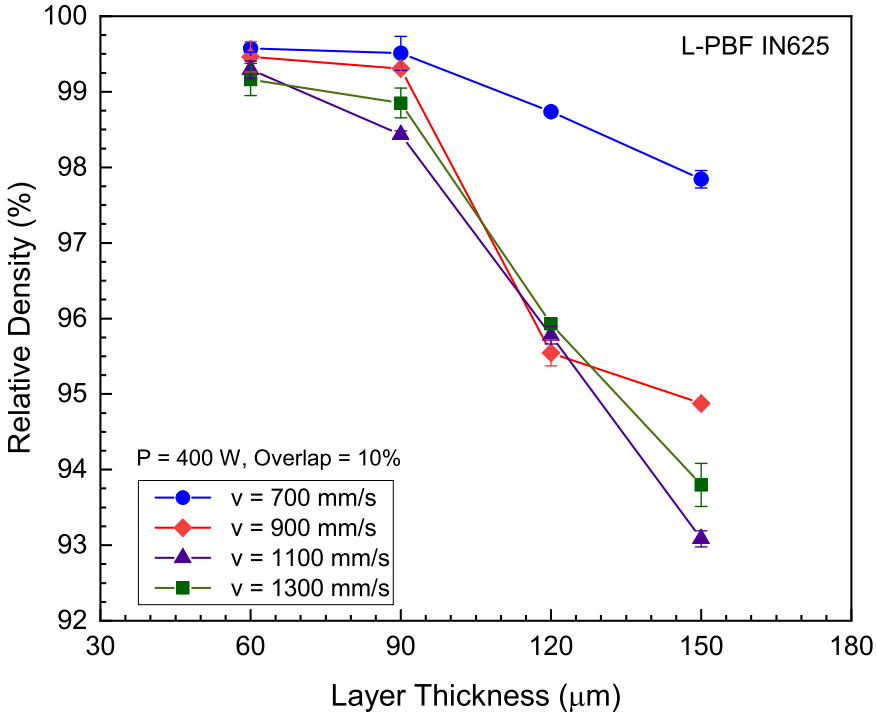

FIGURE 4.24: Relative density of L-PBF IN625 as a function of layer thickness for $v = 700$, 900, 1100, and 1300 mm/s, $P = 400\ W$, and 10% overlap.

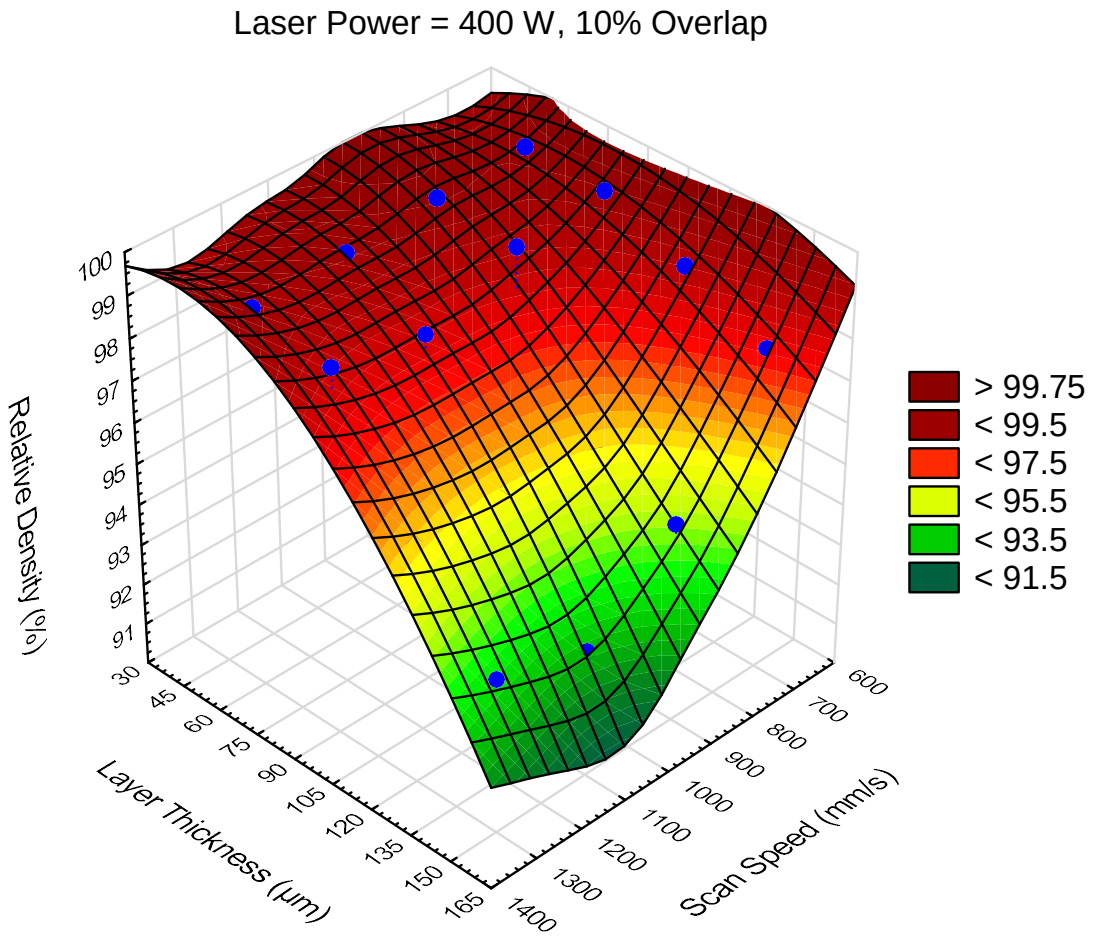

FIGURE 4.25: 3D surface plot of relative density of L-PBF IN625 against scan speed and layer thickness, $P = 400\ W$, 10% overlap.

Furthermore, the values of estimated surface energy density at $t = 60\ \mu m$ are 9.5 and 5.13 J/mm^2 for $v = 700$ and 1300 mm/s, respectively, whereas those at $t = 150\ \mu m$ are 3.8 and 2.1 J/mm^2. As a result, it can be expected that the heat delivered to the powder at 150 μm is not sufficient to melt the powder completely leaving voids and pores in the printed samples and resulting in a lower density compared to that at 60 μm. The processing parameters set of $P = 400\ W$, $v = 700\ mm/s$, and $t = 60\ \mu m$ results in the greatest relative density (99.57%) for 10%

overlap, as shown in Figure 4.24. Kempen et al. [51] found similar results as they studied the effect of increasing layer thickness from 30 to 60 μm on the relative density of maraging steel built by L-PBF.

Similar trends can be seen in Figures 4.26 and 4.27 for 30% overlap and in Figures 4.28 and 4.29 for 50% overlap. However, all the relative density values obtained for overlaps of 30 and 50% are much better than those for 10% overlap (Figure 4.24). In addition, the spreads in relative density caused by the effect of increasing scan speed are smaller for all layer thicknesses tested; the smallest spread was found with overlap of 50%.

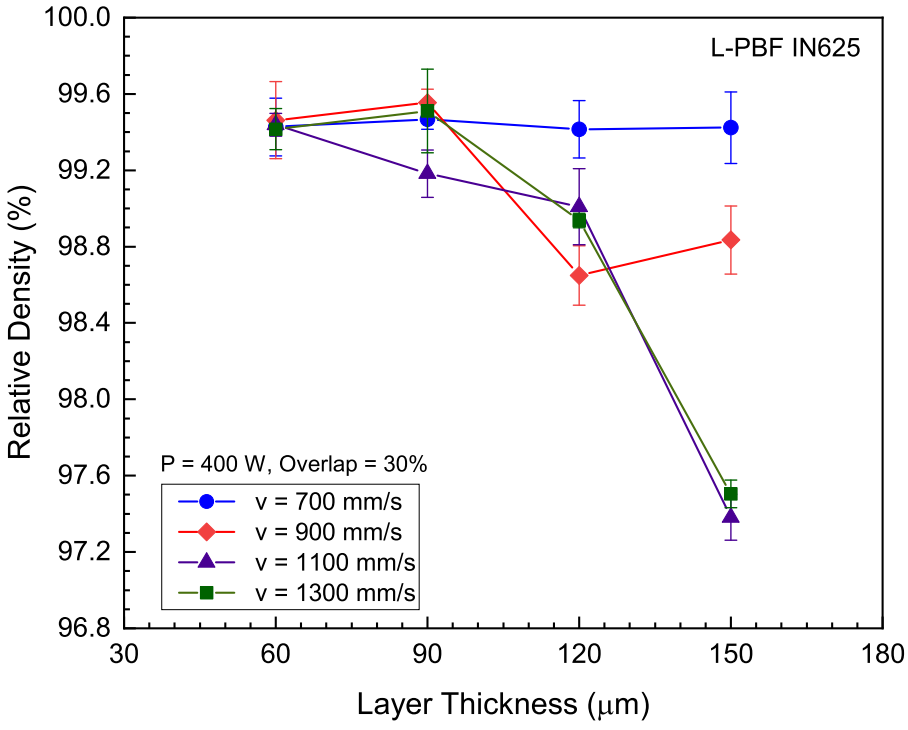

FIGURE 4.26: Relative density of L-PBF IN625 as a function of layer thickness for v = 700, 900, 1100, and 1300 mm/s, P = 400 W, and 30% overlap.

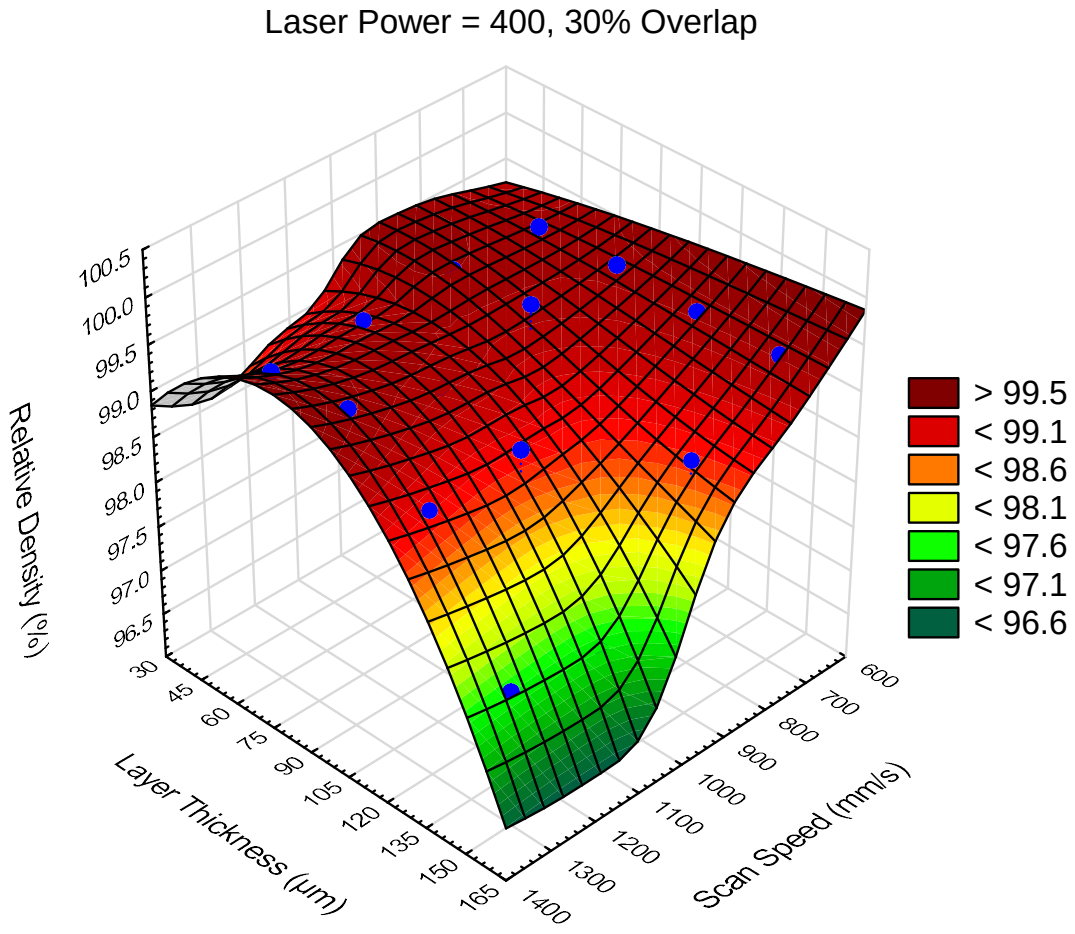

FIGURE 4.27: 3D surface plot of relative density of L-PBF IN625 against scan speed and layer thickness, $P = 400\ W$, 30% overlap.

The processing parameters set: $P = 400\ W$, $v = 900\ mm/s$, and $t = 90\ \mu m$ results in the best relative density (99.55%) for 30% overlap (Figure 4.26), whereas the set of $P = 400\ W$, $v = 700\ mm/$s, and $t = 60\ \mu m$ gives the best relative density (99.57%) for 50% overlap (Figure 4.28).

This behaviour clearly demonstrates the significance of selecting the proper overlap when printing the parts. As the overlap is reduced from 50% to 10%, the hatch distance increases (i.e. increasing the distance between the centres of

adjacent scan tracks). The large hatch distance leads to a lack of fusion because of poor bonding between the scan tracks, lowering the relative density of printed parts. Similar outcomes can be found in [49].

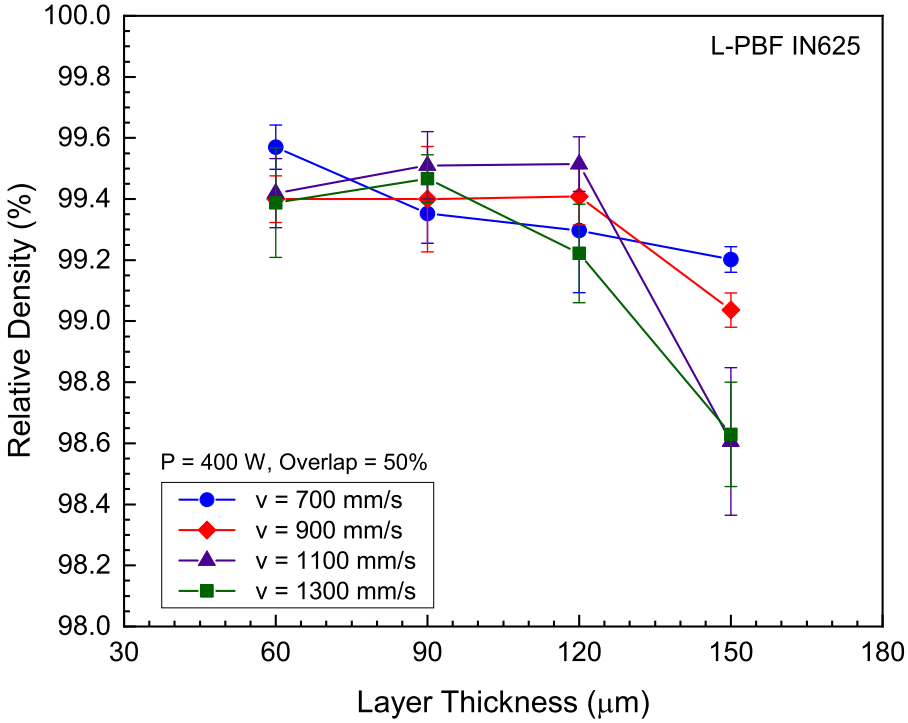

FIGURE 4.28: Relative density of L-PBF IN625 as a function of layer thickness for v = 700, 900, 1100, and 1300 mm/s, P = 400 W and, 50% overlap.

The relative density in Figures 4.24, 4.26, and 4.28 is influenced by two independent parameters (v and t) for a constant overlap. Therefore, multiple linear regression analysis was conducted on the relative density data to identify which of these two parameters has the greatest impact on it.

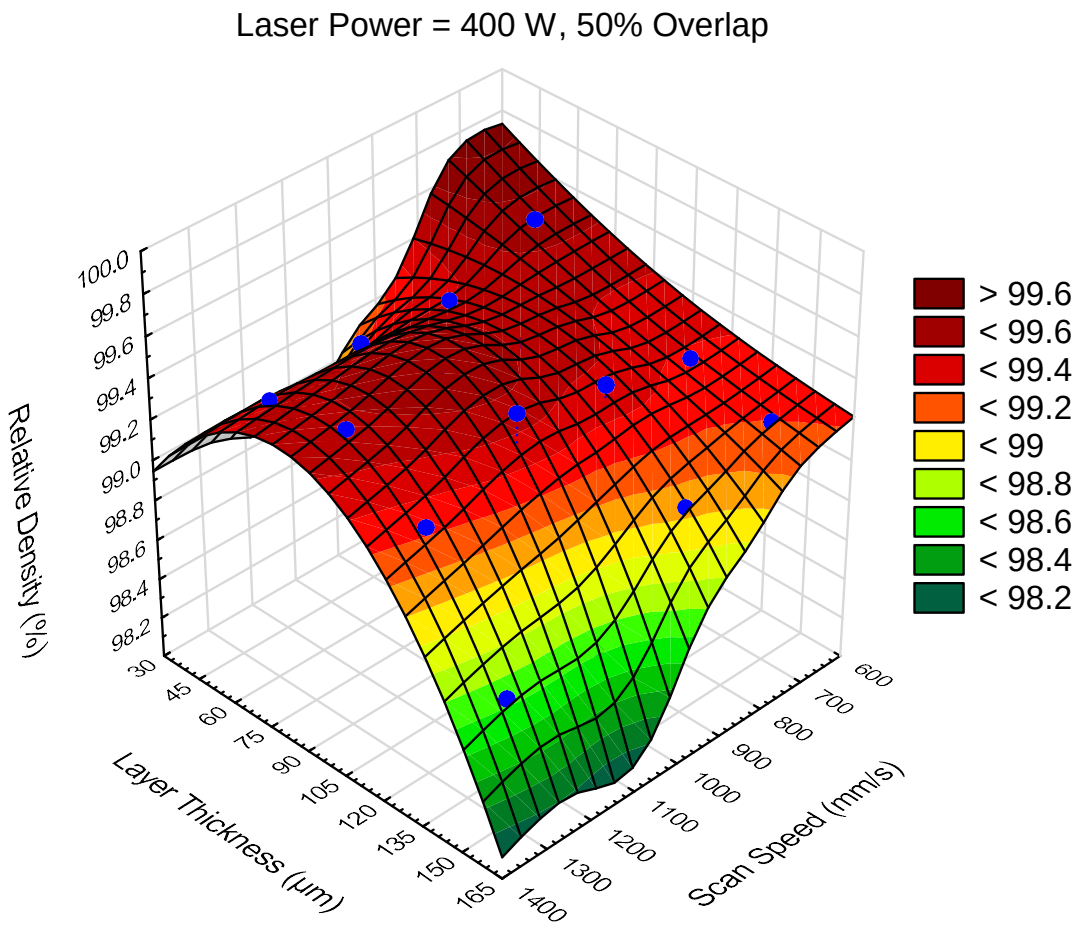

FIGURE 4.29: 3D surface plot of relative density of L-PBF IN625 against scan speed and layer thickness, $P = 400\ W$, 30% overlap.

The statistical analysis results in the following three formulas for overlaps of 10, 30, and 50%, respectively:

$$RD = 108.06 - 0.0033\ v - 0.2375\ t \qquad \textit{for 10\% overlap} \tag{4.4}$$

$$RD = 101.26 - 0.00064\ v - 0.0149\ t \qquad \textit{for 30\% overlap} \tag{4.5}$$

$$RD = 99.87 - 0.000089\ v - 0.00527\ t \qquad \textit{for 50\% overlap} \tag{4.6}$$

Where RD represents the relative density (%), v the scan speed in mm/s, and t the powder layer thickness in μm.

Table 4.5, for example, displays the estimated parameters (v and t) of the model linking relative density with scan speed and layer thickness for 10% overlap. The table shows that the layer thickness (t) has the greatest effect on the relative density because its factor (-0.2375) is much bigger than that of scan speed (-0.00333). The minus sign indicates that increasing v or t causes a decrease in relative density, but that caused by a layer thickness is much greater.

TABLE 4.5: Estimated parameters of the model that relates relative density with scan speed and layer thickness, 10% overlap.

Parameter	Estimate	Standard Error	t-value	p-value
Intercept	108.0643	1.54179	70.09014	<0.001
v	−0.00333	0.0016	−2.08152	0.05771
t	−0.23751	0.08127	−2.92263	0.01188

For overlaps of 30% and 50%, Equations 4.5 and 4.6 also show that the layer thickness has a greater influence on the relative density than the scan speed.

4.2.2 Effect of Surface Energy

The influence of surface energy density on the relative density of L-PBF IN625 samples is seen in Figures 4.30, 4.31, and 4.32 for overlaps of 10%, 30%, and 50%, respectively. The relative density increases rapidly with increasing the energy density for all overlaps tested until a certain limit of surface energy density, after which it remains nearly unchanged. For overlaps of 10, 30, and 50%, these limits

are 5, 4.2, and 3.6 J/mm^2, respectively. Narvan et al. [34] discovered similar results when they investigated the effect of energy density on the relative density of H13 tool steel manufactured by L-PBF.

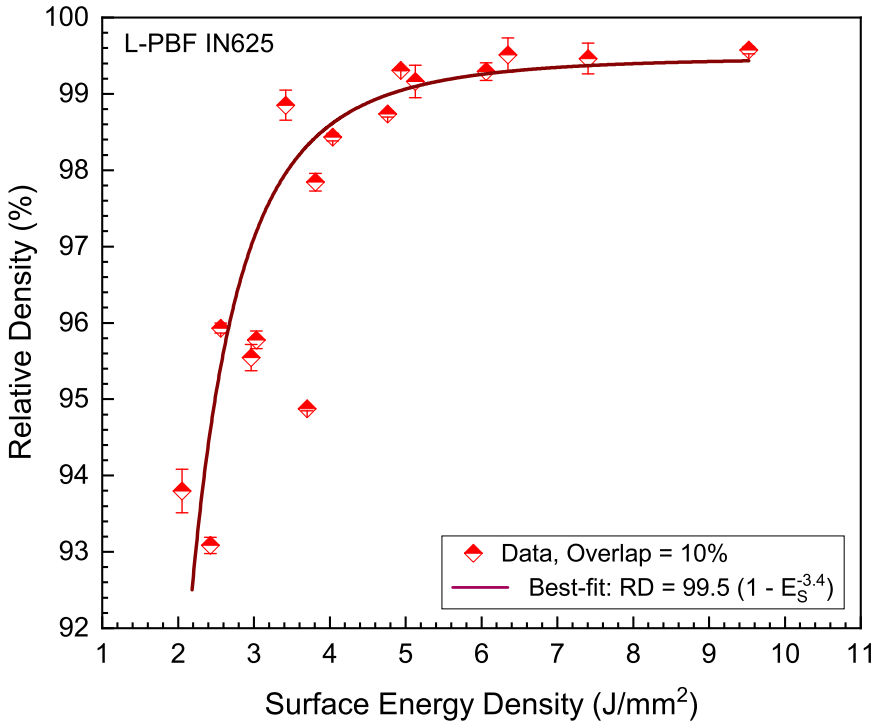

FIGURE 4.30: Relative density of L-PBF IN625 as a function of surface energy density. $P = 400\ W$ and overlap = 10%.

This behaviour can be attributed to the hatch distance which is the greatest at 10% overlap compared to that for 30% overlap or 50%. When all other processing parameters remain constant, the greatest hatch distance results in the least amount of energy. As a result, this energy should be increased to the point where the relative density approaches its steady state. The same discussion holds true when comparing 30% overlap to 50%.

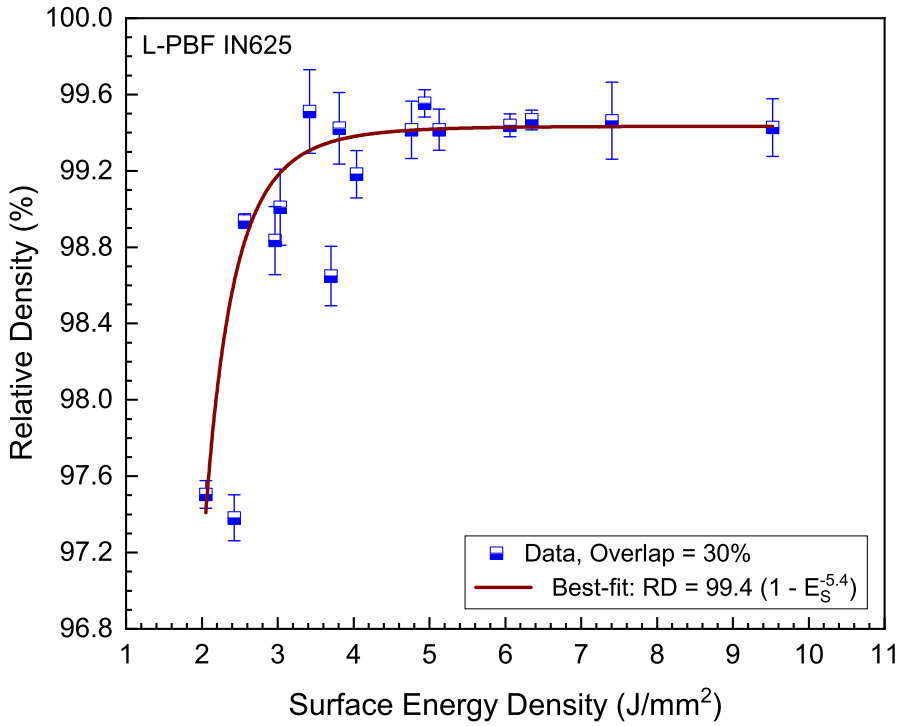

FIGURE 4.31: Relative density of L-PBF IN625 as a function of surface energy density. $P = 400\ W$ and overlap = 30%.

Furthermore, a nonlinear regression modelling using the Levenberg Marquardt iteration algorithm [114, 115] was performed to define the behaviour of relative density in terms of surface energy density. The proposed model to fit the data is shown in Equation 4.7, which was chosen from among several models tested.

$$RD = a\ (1 - E_S^{-b}) \tag{4.7}$$

where RD is the relative density (%), a and b are model parameters.

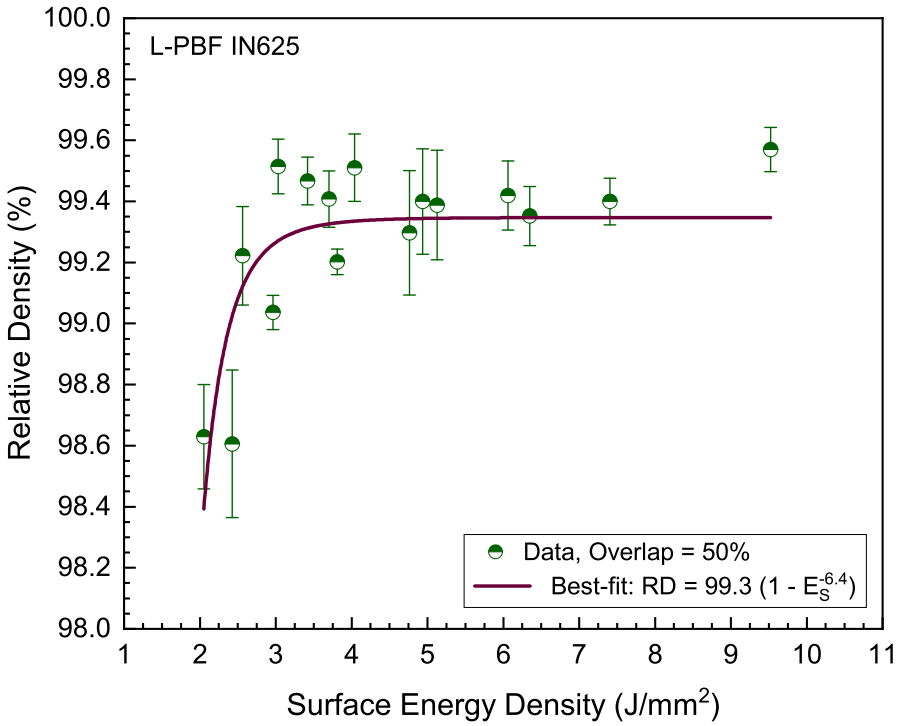

FIGURE 4.32: Relative density of L-PBF IN625 as a function of surface energy density. $P = 400\ W$ and overlap = 50%.

The nonlinear regression analysis suggests the following best-fit models displayed in Equations 4.8, 4.9, and 4.10 for 10%, 30%, and 50% overlap, respectively.

$$RD = 99.5\ (1 - E_S^{-3.4}) \qquad \textit{for 10\% overlap} \tag{4.8}$$

$$RD = 99.4\ (1 - E_S^{-5.4}) \qquad \textit{for 30\% overlap} \tag{4.9}$$

$$RD = 99.3\ (1 - E_S^{-6.4}) \qquad \textit{for 50\% overlap} \tag{4.10}$$

where RD represents the relative density (%) and E_S the surface energy in J/mm^2.

Table 4.6, for example, lists the estimated model parameters of relative density for 30% overlap. The table shows that the model parameters (a and b), using ordinary least squares (OLS), are statistically significant at the 0.05 level of significance because the p-values are less than the level of significance.

TABLE 4.6: Estimated model parameters of relative density for 30% overlap.

Parameter	Estimate	Standard Error	t-value	p-value
a	99.43403	0.08869	1121.18384	<0.0001
b	5.41992	0.16057	33.75394	<0.0001

4.2.2.1 Effect of Overlap and Surface Energy Density

A 3D surface plot shown in Figure 4.33 exhibits the effects of surface energy density and overlap on relative density. The plot clearly indicates that the relative density increases as the overlap or surface energy density increases.

The high overlap results in better bonding with adjacent tracks or previous layer due to the remelting process during the new track or layer scan, enhancing wettability, minimizing voids and pores, and therefore increasing the relative density. In addition, as the surface energy is raised by lowering scan speed, layer thickness, or both, the heat input delivered to the powder increases. As a result, the powder will melt more efficiently, thus reducing voids and accordingly increasing the relative density of the printed parts.

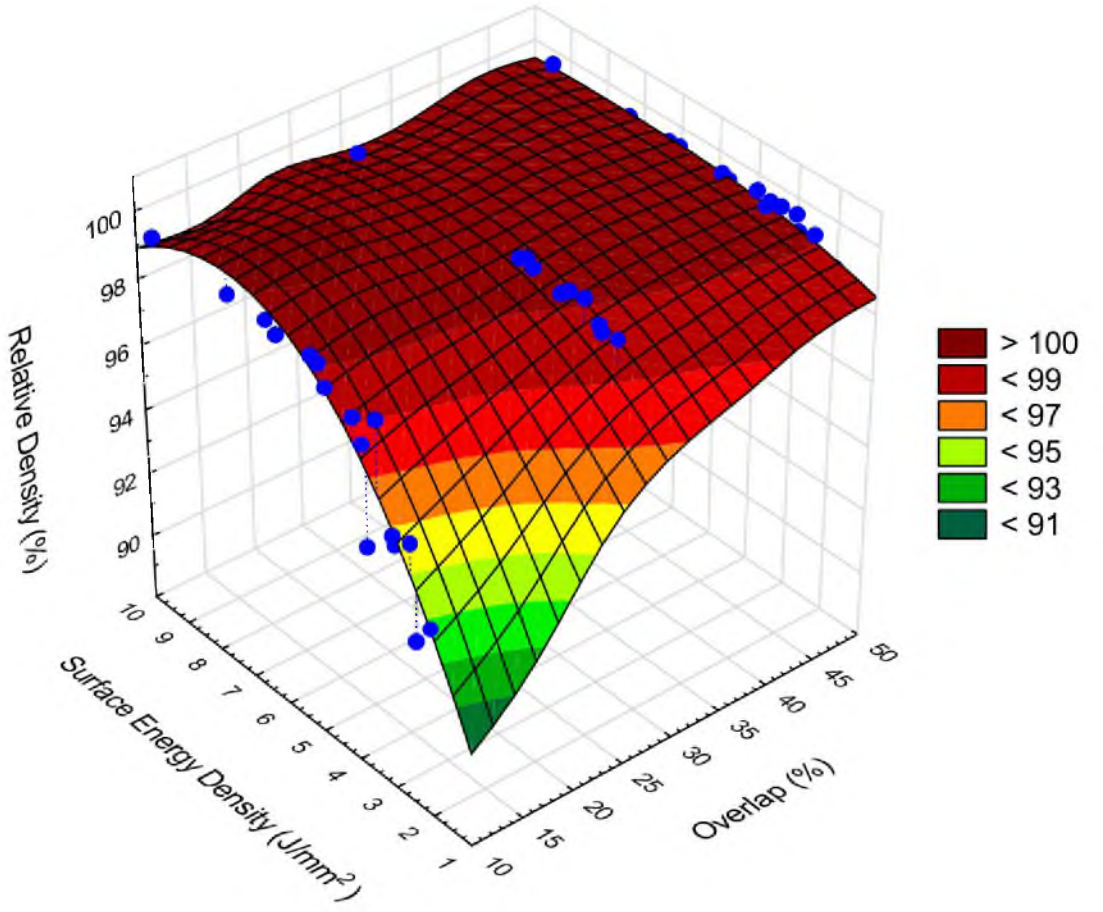

FIGURE 4.33: 3D surface plot of relative density of L-PBF IN625 against surface energy density and overlap percent, $P = 400\ W$.

4.2.3 Statistical Modelling

The aim of statistical modelling is to establish a set of processing parameters for optimizing relative density and productivity of L-PBF IN625. Therefore, multiple regression analysis was carried out on the relative density data considering the effects of scan speed, layer thickness, and overlapping.

The model examined is shown in Equation 4.11.

$$RD = a_0 + a_1\ v + a_2\ t + a_3\ x \tag{4.11}$$

Where RD represents the relative density (%), v the scan speed in mm/s, t the powder layer thickness in μm, and x is the overlap (%).

Table 4.7 displays the model parameters estimated using ordinary least squares (OLS). Since p-values are less than 0.05, the parameters are statistically significant at the 0.05 significance level. The statistical analysis reveals at a constant laser power of 400 W that the overlap (%) compared with scan speed and layer thickness has the greatest effect on relative density because of its biggest factor (0.04568). The positive sign of overlap indicates that the relative density increases with increasing overlap.

TABLE 4.7: Estimated parameters of relative density model in terms of scan speed, layer thickness, and overlap (%).

Parameter	Estimate	Standard Error	t-value	p-value
Intercept	101.23479	0.91932	110.11876	<0.00001
v	−0.00155	7.03281E-4	−2.20114	0.03302
t	−0.02354	0.00469	−5.02117	<0.00001
x	0.04568	0.00963	4.74325	<0.00001

Furthermore, layer thickness is the second most crucial parameter influencing relative density, while scan speed has the least impact. The best fit model is shown in Equation 4.12.

$$RD = 101.235 - 0.0015\ v - 0.0235\ t + 0.0457\ x \tag{4.12}$$

In addition to the multiple regression analysis, 3D surface and contour plotting analysis was performed on all data of relative density for 10, 30, and 50% overlaps to define new sets of processing parameters for maximizing density and productivity. Figures 4.34 and 4.35 illustrate the effects of scan speed and layer thickness on relative density.

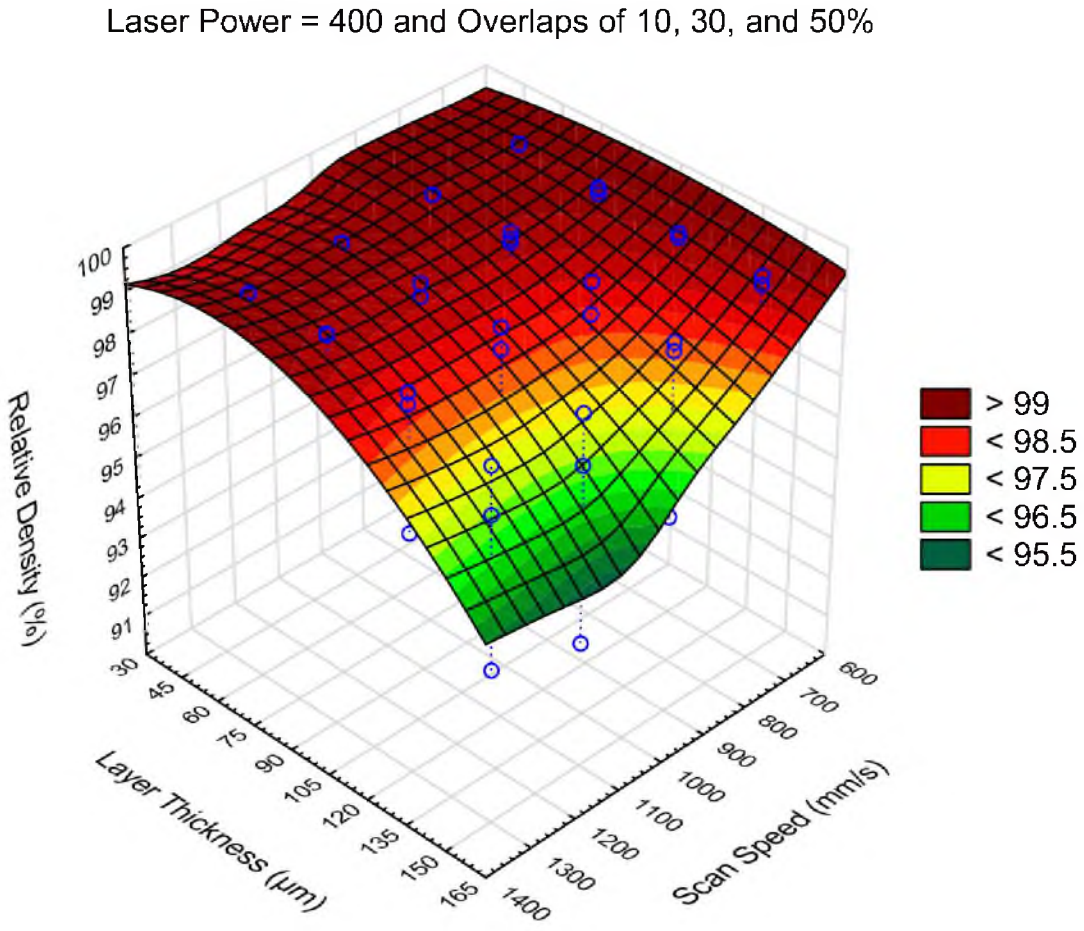

FIGURE 4.34: 3D surface plot showing relative density of L-PBF IN625 as a function of scan speed and layer thickness, $P = 400\ W$.

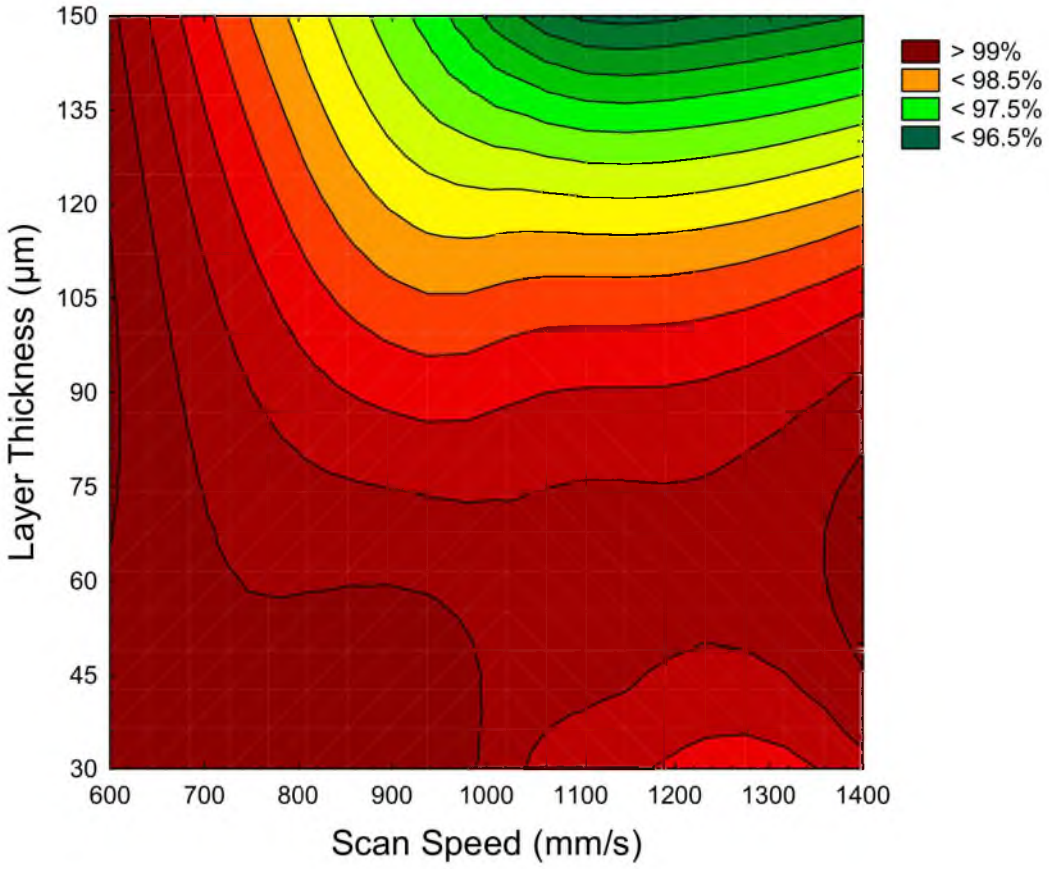

FIGURE 4.35: 3D contour plot showing relative density of L-PBF IN625 against scan speed and layer thickness, $P = 400\ W$.

4.3 Trade-off between Density and Productivity

Based on the multiple regression analysis and 3D surface and contour plotting analysis, four new sets of processing parameters were chosen to print 24 cubes, six replicas for each set. The four sets are shown in Table 4.8, and the manufactured cubes are displayed in Figure 4.36.

TABLE 4.8: Processing parameters sets for printing additional 24 cubes.

Set No.	P (W)	v (mm/s)	t (μm)	x (%)	h (μm)	VED (J/mm^3)
1	400	1300	60	30	84	61.05
2	400	1200	90	50	56	65.55
3	400	700	120	50	83	57.37
4	400	700	150	50	77	49.15

FIGURE 4.36: 24 IN625 cubes printed with $P = 400\ W$. (i) Cubes 1–6 printed with $v = 1300\ mm/s$, $t = 60\ \mu m$, 30% overlap, and $h = 84\ \mu m$. (ii) Cubes 7–12 printed with $v = 1200\ mm/s$, $t = 90\ \mu m$, 50% overlap, and $h = 56\ \mu m$. (iii) Cubes 13–18 printed with $v = 700\ mm/s$, $t = 120\ \mu m$, 50% overlap, and $h = 83\ \mu m$. (iv) Cubes 19–24 printed with $v = 700\ mm/s$, $t = 150\ \mu m$, 50% overlap, and $h = 77\ \mu m$.

4.3.1 Relative Density

Archimedes and image analysis methods were used to determine the density of the cubes. For the Archimedes principle, the density of each cube was measured at least three times, a total of 18 measurements for each processing parameters set, as shown in Table 4.9.

TABLE 4.9: Density measurements of new samples, Archimedes method.

Set No.	Sample No.	Run 1	Run 2	Run 3	Mean (%)	SD (%)	Set Mean (%)	Set SD (%)
	1	99.9644	99.8341	99.7749	99.8578	0.0970		
	2	99.7156	99.5853	99.4550	99.5853	0.1303		
Set 1	3	99.6445	99.4076	99.0521	99.3681	0.2982	99.5162	0.2536
	4	99.5024	99.3720	99.1114	99.3286	0.1991		
	5	99.2772	99.4668	99.7867	99.5103	0.2575		
	6	99.3483	99.2891	99.7038	99.4471	0.2243		
	7	99.4076	99.4550	99.7393	99.5340	0.1794		
	8	99.9763	99.5024	99.3009	99.5932	0.3467		
Set 2	9	99.3957	99.4431	99.5261	99.4550	0.0660	99.4043	0.2405
	10	99.3483	99.3602	99.0166	99.2417	0.1950		
	11	99.1825	99.3246	98.8863	99.1311	0.2237		
	12	99.5498	99.4668	99.3957	99.4708	0.0771		
	13	99.6564	99.1943	98.9455	99.2654	0.3607		
	14	99.2299	99.2536	99.6564	99.3799	0.2397		
Set 3	15	99.2417	99.1114	99.1232	99.1588	0.0721	99.2582	0.1901
	16	99.1469	99.1114	99.4194	99.2259	0.1685		
	17	99.2654	99.1469	99.1706	99.1943	0.0627		
	18	99.52607	99.2062	99.2417	99.3246	0.1753		
	19	99.45498	99.2773	99.3720	99.3681	0.0889		
	20	99.44313	99.2180	99.0995	99.2536	0.1745		
Set 4	21	99.6564	99.0877	99.0166	99.2536	0.3507	99.3102	0.1831
	22	99.36019	99.4905	99.2417	99.3641	0.1245		
	23	99.12322	99.1114	99.3483	99.1943	0.1335		
	24	99.49052	99.2299	99.5616	99.4273	0.1747		

In addition, Figure 4.37 depicts a box plot showing the variation in relative density for each set. Set 1 had the highest density, which gradually decreased until set 3 and then increased with set 4. The difference in means between sets 1 and 4 was calculated to be 0.21%.

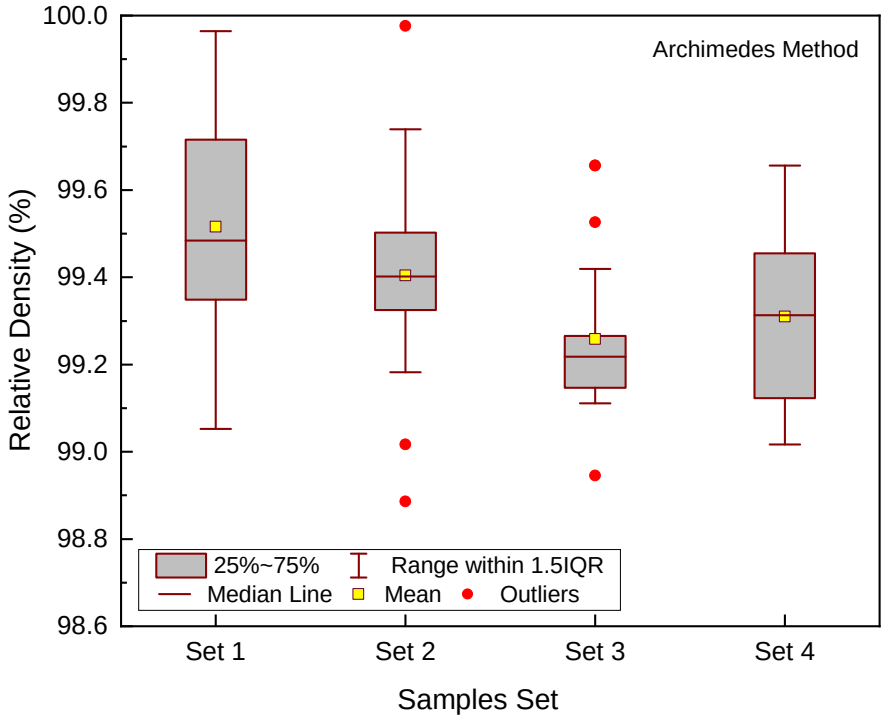

FIGURE 4.37: Box plot showing the variation in relative density (Archimedes method) of new sets of L-PBF IN625, P = 400 W.

Another method that has been adapted to measure the density of printed cubes is image analysis. After being cross-sectioned along the build direction, the samples were ground and polished. Porosity was measured using an optical microscope (Zeiss Axio Imager M2m) and image software (Axio Vision SE64 V4.9), which counts the number of black dots (pores) as a function of the base image colour

(white, for example). For each sample, at least 25 different images were examined at 100x magnification. Three samples from each set were analyzed (i.e., at least 75 images from each set were taken.), and the density of these samples was averaged.

The mean values of relative density of the samples for each set are listed in Table 4.10 and presented as mean ± standard deviation in Figure 4.38. The samples printed under set 2 processing parameters had the highest relative density (99.94%), while the samples printed under set 4 processing parameters had the lowest (99.82%). The difference in relative density mean between sets 2 and 4 was calculated to be 0.12%, which is extremely small. This difference may be justified by inspecting the cross-sections of the samples to evaluate the porosity, as shown in Figure 4.39.

TABLE 4.10: Relative density (%) of the new samples measured by image analysis method.

Set No.	Sample No.	Object Count	Porosity (%)	Density Mean (%)	Set Mean (%)	Set SD (%)
	1	2239	0.05	99.95		
Set 1	3	3843	0.06	99.94	99.92	0.03786
	5	8611	0.12	99.88		
	7	2090	0.06	99.94		
Set 2	9	1337	0.06	99.94	99.94	0.00577
	11	4643	0.07	99.93		
	13	1454	0.17	99.83		
Set 3	15	1945	0.18	99.82	99.84	0.02646
	17	2187	0.13	99.87		
	19	5238	0.16	99.84		
Set 4	21	2234	0.25	99.75	99.82	0.05859
	23	2040	0.14	99.86		

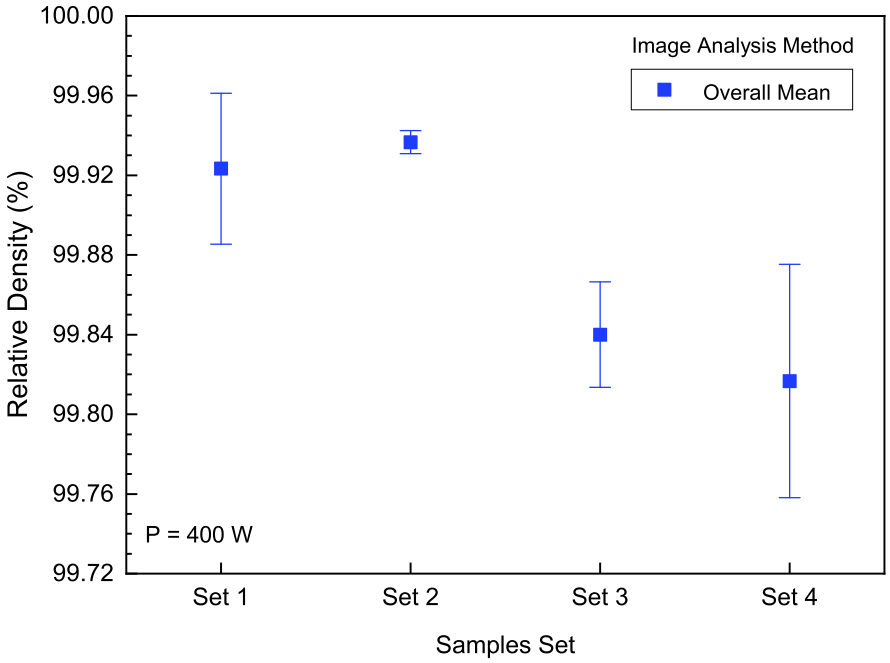

FIGURE 4.38: Relative density interval plot of L-PBF IN625 new sets measured by image analysis method, $P = 400\ W$.

Figure 4.40 depicts the relative density of L-PBF IN625 determined by Archimedes and image analysis methods as a function of volumetric energy density. There are differences in relative density values obtained by these techniques, in which the values calculated by Archimedes principle are inferior to those by the image analysis method. One Way Analysis of Variance (One Way ANOVA) statistical method was performed on the relative density data collected by both methods. It shows that the differences in mean values among the treatment sets are statistically significant at the 0.05 level of significance.

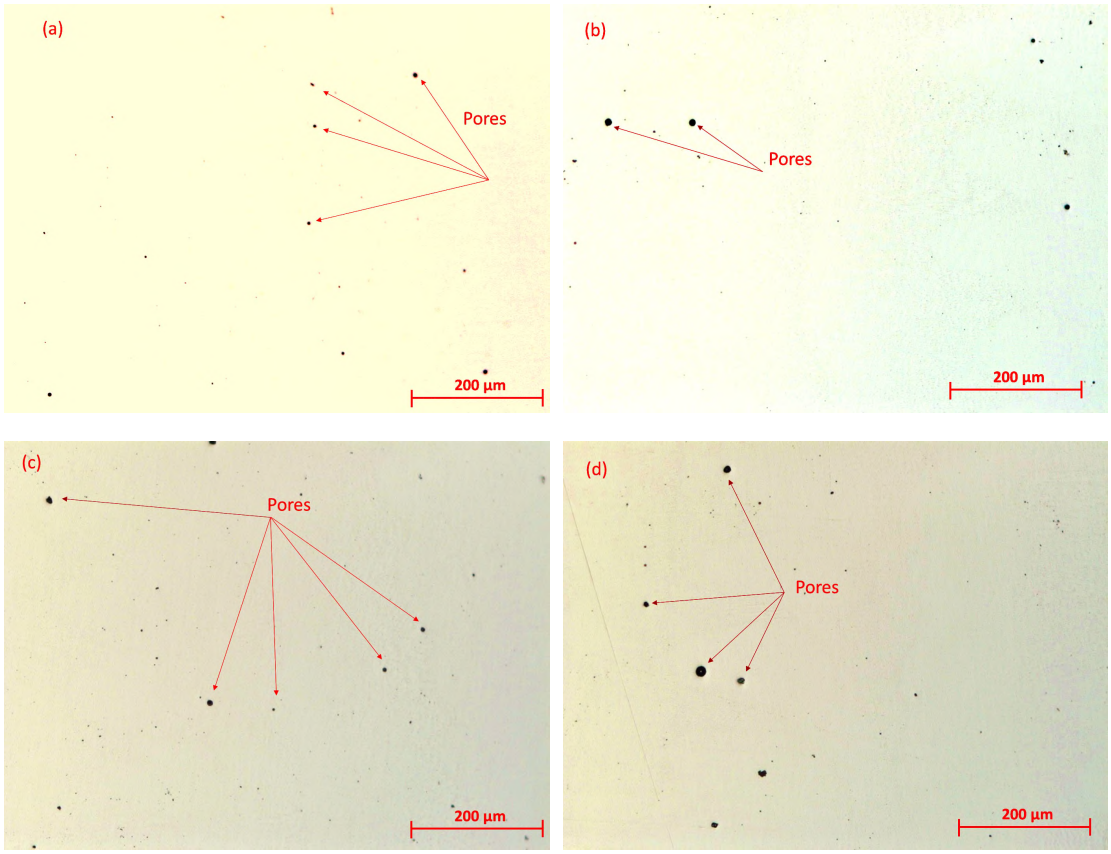

FIGURE 4.39: Optical images of cross-sections along build direction (Z-direction) showing the porosity developed in L-PBF IN625 for (a & b) set 2 processing parameters and (c & d) set 4 processing parameters.

Nonetheless, it can be agreed that the relative density calculated by the Archimedes principle is more reliable since the entire volume of the sample is considered in density measurement. Whereas, the image analysis method deals with a cross-section, which may not reflect the total porosity of the sample.

Figure 4.40 also shows that the energy density values of 61 J/mm^3 (set 1) and 65.5 J/mm^3 (set 2) result in the best density of 99.52 and 99.40%, respectively, obtained by Archimedes principle. On the other hand, the laser energy values

above are linked with relative density of 99.92 and 99.94% determined by the image analysis method.

When these density measurement techniques are compared, it can be concluded that the Archimedes method is more reliable, repeatable, non-destructive, fast, and cheap method. On the other hand, the image analysis technique aids in gaining insight into the shape of pores and their distribution within the cross section of the part.

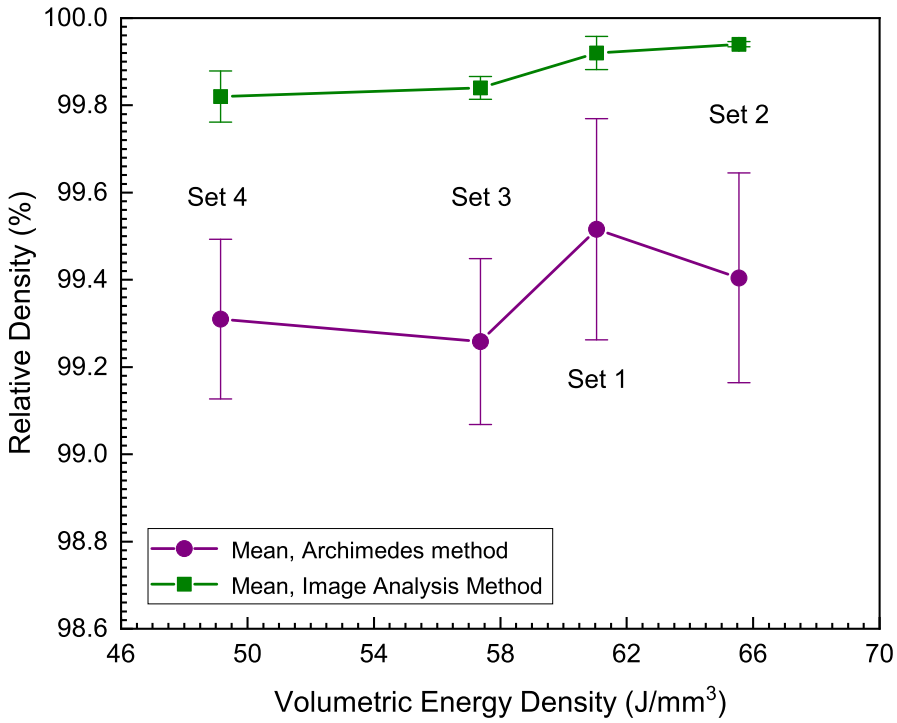

FIGURE 4.40: Relative density of L-PBF IN625 as a function of volumetric energy density, $P = 400\ W$.

4.3.2 Hardness

Hardness measurements were carried out on the cross-section along the build direction. Before measuring, the cross-sections of the cubes were prepared according to the standard metallographic techniques described in Section 3.5, Chapter 3. Hardness testing was conducted under a load of 0.5 kg_f for a dwell time of 15 sec. Figure 4.41 depicts the variation in hardness of the printed IN625 according to the processing parameter sets listed in Table 4.8, Section 4.3.

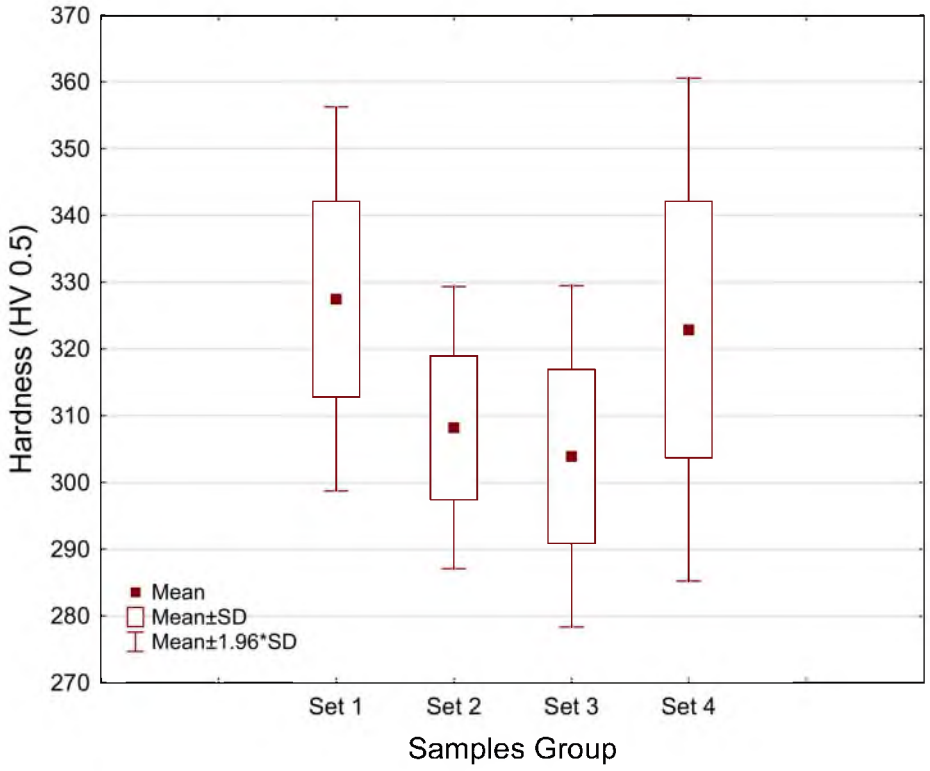

FIGURE 4.41: Hardness (HV 0.5) of L-PBF IN625 new sets, $P = 400\ W$.

To identify possible outliers in hardness data for each set, Grubbs statistical test was performed on the data [117]. As a result, no significant outlier was identified at the 0.05 level. Table 4.11 depicts the hardness descriptive statistics of each set.

TABLE 4.11: L-PBF IN625, hardness descriptive statistics, $P = 400\ W$.

Set No.	N total	Mean	SD	Minimum	Maximum
Set 1	30	327.48	14.674	304	356
Set 2	10	308.20	10.778	291	326
Set 3	10	303.90	13.042	279	326
Set 4	30	322.89	19.216	283	362

As shown in the table, the samples from set 1 had the highest hardness values, followed by those from set 4. When a One Way ANOVA statistical analysis is performed on the hardness data of set 1 ($t = 60\ \mu m$) and set 4 ($t = 150\ \mu m$), the population means of both sets are not significantly different at the 0.05 level. These findings are essential because IN625 parts can be printed with a high layer thickness, resulting in higher productivity (fewer slices to print) while maintaining similar mechanical properties.

Balbaa et al. [13] tested the microhardness (HV 0.1) of IN625 printed with $P = 270\ W$, $v = 600\ mm/s$, $h = 0.1\ mm$, and $t = 0.04\ mm$, with a load of 100 g. A mean hardness of about 320 HV 0.1 was measured. The outcome of hardness testing is well known to be highly dependent on the applied load: the lower the load, the higher the hardness value. If hardness testing was carried out with a load of 500 g, as was done in this study, the hardness results in [13] may be slightly lower than those obtained with a load of 100 g. Although the load used in this study was higher than that used by Balbaa et al., the average hardness of set 4 (323 HV 0.5) samples is consistent with that found in [13].

Nguejio et al. [107] printed IN625 samples with the optimal L-PBF processing parameters: $P = 247\ W$, $v = 1000\ mm/s$, $h = 0.08\ mm$, and $t = 0.02\ mm$. The mean hardness obtained in the plane XZ parallel to the build direction was 313 HV

0.5. Yan et al. [108] measured a hardness of 322 HV 0.2 with optimal processing parameters of $P = 280\ W$, $v = 950\ mm/s$, $h = 0.11\ mm$, and $t = 0.03\ mm$.

In summary, the hardness results found by Balbaa et al. [13], Nguejio et al. [107], and Yan et al. [108] are consistent with those found in this study for set 4 samples. However, the productivity of this work ($v \times t \times h$) is significantly higher.

4.3.3 Microstructure

The microstructure of a sample printed with set 4 processing parameters of thickest powder layer is presented in Figure 4.42. The microstructure of L-BPF IN 625 alloy differs significantly from that of conventionally processed alloy. Due to extremely high cooling rates of about $10^6\ K/s$ [97], the as-built L-BPF IN625 alloy shows a non-equilibrium microstructure with very fine cellular and columnar dendritic features compared to conventionally manufactured alloy [7, 98]. Diffusion process to generate precipitates is hampered by the rapid cooling, leaving the Ni matrix with the bulk of strengthening elements such as Mo and Nb [73].

Melt pools generated during the laser beam scanning are visible, with depths nearly greater than two layers ($> 300\ \mu m$), as shown in Figure 4.42. The melt pools have similar V-like shapes due to the Gaussian distribution of the laser energy, with the greatest value focused on the centre of laser beam [79]. It can also be seen grains elongation along the build direction (Z-direction), with non-uniform crystallographic orientations. Owing to the direction of heat flux during the melt pool solidification, the grains grow epitaxially along the build direction (nearly perpendicular to the substrate), intersecting multiple melt pools. Furthermore, the

structure of the previous layer influences the columnar dendritic growth in the new layer. Similar features were reported in [73, 79, 105, 118].

FIGURE 4.42: Optical micrograph showing the microstructure of L-PBF IN625 printed with set 4 processing parameters.

Although the grain growth mechanism is complicated and controlled by several factors, the direction of local heat conduction, influenced by scan speed and scanning strategy, is found to be critical in determining grain orientation and hence microstructural texture [83, 105, 118]. During subsequent laser scanning, large sections of laser tracks remelt due to overlap applied. In addition, coarse cellular structures developed in the inter-melt-pool regions are expected because these regions are less overlapping and less heat affected [83]. Due to gas entrapment, some round pores are visible.

4.3.4 Productivity

Productivity for printing parts by L-PBF process can be calculated using the following equation:

$$\mathring{P} = v \times t \times h \tag{4.13}$$

where $\mathring{P}$ is the productivity in mm^3/s, v scan speed in mm/s, t layer thickness in mm, and h is the hatch distance in mm. The productivity can also be given in mm^3/min, as shown in Table 4.12. The highest productivity of 485.10 mm^3/min is calculated with set 4.

TABLE 4.12: Processing parameters sets and productivity of IN625 printed by L-PBF.

Set No.	P (W)	v (mm/s)	t (μm)	x $(\%)$	h (μm)	$\mathring{P}$ (mm^3/min)
1	400	1300	60	30	84	393.12
2	400	1200	90	50	56	362.88
3	400	700	120	50	83	418.32
4	400	700	150	50	77	485.10

Productivity can be increased by increasing one or more of the following parameters: scan speed, layer thickness, and hatch distance. However, increasing one of these parameters while holding the others constant reduces the energy density or heat supplied to the powder, resulting in a decrease in the density and mechanical properties of the printed part. As a result, any changes to these parameters to enhance productivity should be made with caution, while keeping the part properties almost unchanged.

Balbaa et al. [13] measured the relative density and hardness of IN625 printed at $P = 270\ W$, $v = 600\ mm/s$, $h = 0.1$, and $t = 0.04\ mm$. Under these processing parameters, the relative density, hardness, and productivity were reported as 99.3%, 319 HV 0.1, and 144 mm^3/min, respectively. The relative density, hardness, and productivity of the samples printed under set 4 ($t = 150\ \mu m$) processing parameters are 99.310 ± 0.183% (Archimedes principle), 99.82 ± 0.058% (image analysis), (322.89 ± 19.216) HV 0.5, and 485.10 mm^3/min. When the results are compared, they agree with those reported in [13]. However, the productivity of this study is more than three times (factor of 3.369) greater than that of [13] while maintaining comparable physical and mechanical properties.

Table 4.13 depicts a comparison of the layer thickness, relative density, hardness, and productivity of this study (TS) with those published in the literature. Furthermore, Figure 4.43 depicts the normalized data obtained by dividing the literature data by the present data.

TABLE 4.13: Comparison of the presented L-PBF IN625 results with those published in the literature.

P (W)	v (mm/s)	h (μm)	t (μm)	$\mathring{P}$ (mm^3/min)	RD (%)	Mean Hardness, HV	Ref.
270	600	100	40	144	99.3	319 HV 0.1	[13]
270	700	120	40	201.6	98.5	327 HV 0.1	
180	1000	100	40	240	NA	304 HV 0.3	[16]
160	500	60	20	36	NA	343 HV 0.5	[73]
120	590	90	25	79.65	99.36	265 HV 1	[103]
120	100	100	50	30	98.3	298 HV 0.3	[104]
120	200	100	50	60	92.5	334 HV 0.3	
247	1000	80	20	96	NA	313 HV 0.5	[107]
280	950	110	30	188.1	NA	322 HV 0.2	[108]
400	700	77	150	485.1	99.31	323 HV 0.5	[TS]

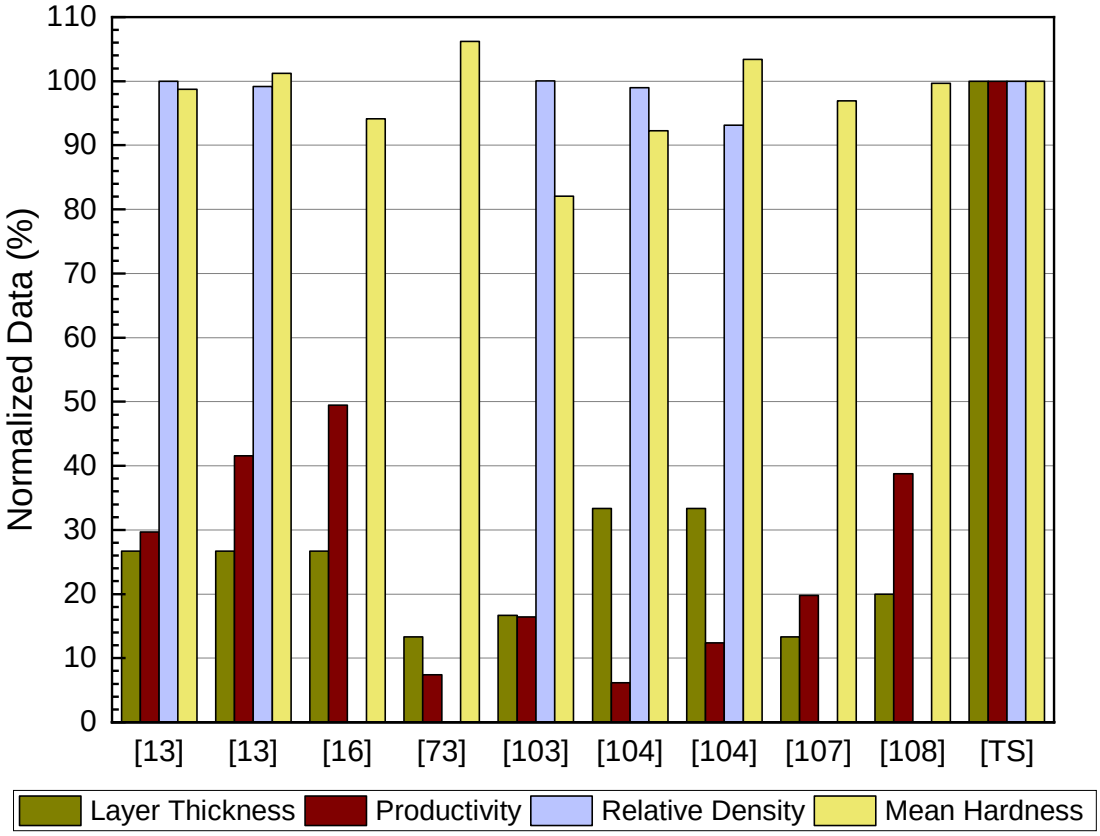

FIGURE 4.43: Comparison of L-PBF IN625 results of this study with those published in the literature using normalization.

Finally, it can be concluded from Table 4.13 and Figure 4.43 that the findings of this study are significant because IN625 parts can be printed with higher layer thicknesses while retaining material properties comparable to those printed with typical layer thicknesses of 20–50 μm. Reduced production time due to optimized processing parameters can result in substantial energy and cost savings.

Chapter 5

CONCLUSIONS AND FUTURE WORK

5.1 Conclusions

Laser Powder Bed Fusion (L-PBF) is a metal additive manufacturing process that allows for the creation of new geometries and complex internal structures with improved properties. However, the main drawbacks of the L-PBF process are its high costs and lengthy production time. As a result, reducing the manufacturing process while maintaining comparable properties is extremely advantageous. Inconel 625 (IN625) alloy is used in a variety of industries, including aerospace. The properties of IN625 components produced by casting or forging, on the other hand, are hard to control. Furthermore, the IN625 alloy is difficult to machine. Because of its excellent weldability, IN625 alloy appears to be a promising candidate for additive manufacturing.

This thesis presents an experimentally focused investigation on optimizing L-PBF processing parameters in IN625 superalloy to significantly boost process productivity while retaining material density and hardness comparable to those produced with typical powder layer thicknesses of 20 to 40 μm. Increasing powder layer thickness while optimizing the input energy by changing laser power, scan speed, and hatch distance to guarantee sufficient heat is provided to the powder bed for creating stable melt pools is one approach for increasing production rate.

Powder layer thicknesses used with L-PBF IN625 alloy ranged from 20 to 60 μm, according to a literature review. Furthermore, no systematic studies on the effects of increasing layer thickness on the quality and productivity of printed parts have been identified. The majority of the research focused on producing parts with thinner powder layers and evaluating their qualities, rather than on the production rate. As a result, the objective of this research was to increase productivity by greatly thickening the powder bed while optimizing laser power, scan speed, and hatch distance to obtain high material density and hardness.

To achieve this goal, powder layer thicknesses of 30, 60, 90, 120, and 150 μm, higher laser powers of 300 and 400 W, five levels of scan speed ranging from 500 to 1300 mm/s, and three levels of overlapping of 10, 30, and 50% were investigated. A layer thickness of 30 μm was used as a baseline for comparison. Single tracks and cubes were printed and characterized. Multiple linear regression analysis, non-linear modelling, as well as 3D surface and contour plots were performed. Relative density, hardness, microstructure, and productivity were all evaluated.

The following are the main findings of this study:

1. The optimized processing parameters obtained by statistical analysis methods that resulted in the highest production rate of 485.1 mm^3/min were as follows:
   layer thickness = 150 μm, laser power = 400 W, scan speed = 700 mm/s, and hatch distance = 77 μm.
   The volumetric energy density was calculated to be 49.15 J/mm^3.

2. The average relative density of the samples printed with the optimized parameters listed in the first conclusion was 99.31% ± 0.1831% obtained by Archimedes approach and 99.82 % ± 0.05859% obtained by image analysis technique. Although the production rate in this study is substantially higher than those published by Balbaa et al. [13], Zhang et al. [104], Nguejio et al. [107], and Yan et al. [108] by factors of 3.37, 8.08, 5.05, and 2.58, respectively, the obtained relative density is consistent with their published relative density values.

3. Despite having a significantly higher productivity, the average hardness of the samples printed using the optimized parameters described in the first conclusion was comparable to or better than those found in the literature [13, 16, 103, 104, 107, 108].

4. The as-built IN625 alloy had a non-equilibrium microstructure with very fine cellular and columnar dendritic characteristics due to the extraordinarily high solidification rate. Furthermore, coarse cellular structures are seen in the inter-melt-pool zones, which have less overlapping and are less heat

influenced. Elongation of grains along the build direction (Z-direction) can be noticed. The grains develop epitaxially along the build direction (nearly perpendicular to the substrate) due to the direction of heat flow during melt pool solidification.

5. To show the effects of layer thickness, scan speed, and overlap on the relative density of the samples, a multiple linear regression model was suggested. In comparison to scan speed and layer thickness, the model revealed that the overlap percent had the biggest impact on relative density. With greater overlapping, the relative density increased considerably.

6. A nonlinear regression model, $RD = a\ (1 - E_S^{-b})$, was presented to correlate the relative density (RD) to surface energy density (E_S), where a, and b are model parameters. For all overlaps examined with this model, the relative density grew rapidly as the surface energy density increased until a certain point, after which it remained almost unchanged. These limits are 5, 4.2, and 3.6 J/mm^2 for overlaps of 10, 30, and 50%, respectively.

7. The findings of this research are significant because IN625 parts can be manufactured with higher powder layer thicknesses (increased productivity) while retaining material properties similar to those printed with usual thin powder layers of 20–40 μm. Reduced production time due to optimized processing parameters can result in substantial energy and cost savings.

5.2 Future Work

This study looked at how to improve the productivity of L-PBF IN625 by increasing the powder layer thickness and optimizing other processing parameters to produce dense, crack-free parts. The relative density, hardness, microstructure, and productivity of the samples printed under optimized conditions were evaluated. However, the following are some interesting topics to consider for future work:

1. Investigating and comparing the tensile mechanical properties of samples produced with the thickest powder layer of 150 μm to those obtained with a standard powder layer of 30 μm.

2. Investigating high-cycle fatigue and fatigue crack propagation in samples made with the thickest powder layer of 150 μm and comparing them to those made with a standard powder layer of 30 μm.

3. Analyzing the behaviour of IN625 samples printed with powder layers thicker than 150 μm.

4. Evaluating the effects of increasing powder layer thickness and laser beam diameter on density, hardness, microstructure, and productivity.

5. Studying the impact of using multiple laser sources on the quality and productivity of L-PBF IN625 parts.

6. Evaluating the quality and productivity of L-PBF printed samples using thicker powder layers, bigger laser beam diameters, and multiple laser sources.

Chapter 6

REFERENCES

[1] A.P. Mouritz. Introduction to Aerospace Materials. Elsevier, 2012.

[2] J.T. Winowlin Jappes, A. Ajithram, M. Adamkhan, D. Reena. Welding on Ni based super alloys – A review. *Materials Today: Proceedings, 2022.*

[3] X. Tang, S. Wang, L. Qian, Y. Li, Z. Lin, D. Xu. Corrosion behavior of nickel base alloys, stainless steel and titanium alloy in supercritical water containing chloride, phosphate and oxygen. *Chemical Engineering Research and Design 100 (2015) 530–541.*

[4] S. Khorsand, A. Sheikhi, K. Raeissi, M.A. Golozar. Hot corrosion behavior of Inconel 625 superalloy in eutectic molten nitrate salts. *Oxidation of Metals 90 (2018) 169–186.*

[5] X. Liu, J. Fan, Y. Song, P. Zhang, F. Chen, R. Yuan, J. Wang, B. Tang, H. Kou, J. Li. High-temperature tensile and creep behaviour of Inconel 625 superalloy sheet and its associated deformation-failure micromechanisms. *Materials Science and Engineering: A 829 (2022) 142152.*

[6] C. Tan, F. Weng, S. Sui, Y. Chew, G. Bi. Progress and perspectives in laser additive manufacturing of key aeroengine materials. *International Journal of Machine Tools and Manufacture 170 (2021) 103804.*

[7] K.B.S.R. Vani Shankar, S.L. Mannan. Microstructure and mechanical properties of Inconel 625 superalloy. *Journal of Nuclear Materials 288 (2001) 222–232.*

[8] A.K. Parida, K. Maity. Comparison the machinability of Inconel 718, Inconel 625 and Monel 400 in hot turning operation. *Engineering Science and Technology, an International Journal 21(3) (2018) 364–370.*

[9] E. Liu, W. An, Z. Xu, H. Zhang. Experimental study of cutting-parameter and tool life reliability optimization in Inconel 625 machining based on wear map approach. *Journal of Manufacturing Processes 53 (2020) 34–42.*

[10] M.Q. Saleem, S. Mumtaz. Face milling of Inconel 625 via wiper inserts: Evaluation of tool life and workpiece surface integrity. *Journal of Manufacturing Processes 56 (2020) 322–336.*

[11] J.C. Lippold, S.D. Kiser, J.N. DuPont. Welding Metallurgy and Weldability of Nickel-Base Alloys. John Wiley & Sons, 2011.

[12] J.L. Caron, J.W. Sowards. Weldability of nickel-base alloys. *Comprehensive Materials Processing (2014) 151-179.*

[13] M. Balbaa, M. Elbestawi, J. McIsaac. An experimental investigation of surface integrity in selective laser melting of Inconel 625. *The International Journal of Advanced Manufacturing Technology 104(9) (2019) 3511–3529.*

[14] J. Gonzalez, J. Mireles, S. Stafford, M. Perez, C. Terrazas, R. Wicker. Characterization of Inconel 625 fabricated using powder-bed-based additive

manufacturing technologies. *Journal of Materials Processing Technology 264 (2019) 200–210.*

[15] Z. Tian, C. Zhang, D. Wang, W. Liu, X. Fang, D. Wellmann, Y. Zhao, Y. Tian. A review on laser powder bed fusion of Inconel 625 nickel-based alloy. *Applied Sciences 10(1) (2020) 81.*

[16] A. Gamon, E. Arrieta, P.R. Gradl, C. Katsarelis, L.E. Murr, R.B. Wicker, F. Medina. Microstructure and hardness comparison of as-built inconel 625 alloy following various additive manufacturing processes. *Results in Materials 12 (2021) 100239.*

[17] ASTM Standard. ASTM F42.91. F2792-12a: Standard Terminology for Additive Manufacturing Technologies, ASTM International, West Conshohocken, 2012.

[18] J.O. Milewski. Additive Manufacturing of Metals. Springer, 2017.

[19] M. Brandt. Laser Additive Manufacturing: Materials, Design, Technologies, and Applications. Elsevier, 2017.

[20] J. Allen. An Investigation into the Comparative Costs of Additive Manufacture vs. Machine from Solid for Eero Engine Parts. Rolls-Royce Plc Derby, UK, 2006.

[21] T. Wohlers. Wohlers Report 2017: 3D Printing and Additive Manufacturing State of the Industry Annual Worldwide Progress Report. Wohlers Associates, Fort Collins, 2017.

[22] J. Watson, K. Taminger. A decision-support model for selecting additive manufacturing versus subtractive manufacturing based on energy consumption. *Journal of Cleaner Production 176 (2018) 1316–1322.*

[23] EOS. Future Ariane propulsion module: Simplified by additive manufacturing, 2018.
https://www.eos.info/press/case_studies/future-ariane-propulsion-module-simplified-with-3d-printing

[24] S. Kumar. Selective laser sintering/melting. *Comprehensive Materials Processing 10 (2014) 93–134.*

[25] A. Simchi, H. Pohl. Effects of laser sintering processing parameters on the microstructure and densification of iron powder. *Materials Science and Engineering: A 359 (2003) 119–128.*

[26] U.S. Bertoli, A.J. Wolfer, M.J. Matthews, J.-P.R. Delplanque, J.M. Schoenung. On the limitations of volumetric energy density as a design parameter for selective laser melting. *Materials & Design 113 (2017) 331–340.*

[27] G. Marchese, E. Bassini, S. Parizia, D. Manfredi, D. Ugues, M. Lombardi, P. Fino, S. Biamino. Role of the chemical homogenization on the microstructural and mechanical evolution of prolonged heat-treated laser powder bed fused Inconel 625. *Materials Science and Engineering: A 796 (2020) 140007.*

[28] J.P. Oliveira, A.D. LaLonde, J. Ma. Processing parameters in laser powder bed fusion metal additive manufacturing. *Materials & Design 193 (2020) 108762.*

[29] M. Salarian, H. Asgari, M. Vlasea. Pore space characteristics and corresponding effect on tensile properties of Inconel 625 fabricated via laser powder bed fusion. *Materials Science and Engineering: A 769 (2020).*

[30] J.R. Poulin, A. Kreitcberg, V. Brailovski. Effect of hot isostatic pressing of laser powder bed fused Inconel 625 with purposely induced defects

on the residual porosity and fatigue crack propagation behavior. *Additive Manufacturing 47 (2021) 102324.*

[31] H. Soni, M. Gor, G. Singh Rajput, P. Sahlot. A comprehensive review on effect of process parameters and heat treatment on tensile strength of additively manufactured Inconel-625. *Materials Today: Proceedings 47 (2021) 4866-4871.*

[32] M. Tomlin, J. Meyer. Topology optimization of an additive layer manufactured (ALM) aerospace part. In *Proceeding of the 7th Altair CAE technology conference, 1–9, 2011.*

[33] D. Bourell, J.P. Kruth, M. Leu, G. Levy, D. Rosen, A.M. Beese, A. Clare. Materials for additive manufacturing. *CIRP Annals 66 (2017) 659-681.*

[34] M. Narvan, K.S. Al-Rubaie, M. Elbestawi. Process-Structure-Property Relationships of AISI H13 Tool Steel Processed with Selective Laser Melting. *Materials (Basel) 12(14) (2019).*

[35] K.S. Al-Rubaie, S. Melotti, A. Rabelo, J.M. Paiva, M.A. Elbestawi, S.C. Veldhuis. Machinability of SLM-produced Ti6Al4V titanium alloy parts. *Journal of Manufacturing Processes 57 (2020) 768-786.*

[36] D. Mahmoud, K.S. Al-Rubaie, M.A. Elbestawi. The influence of selective laser melting defects on the fatigue properties of Ti6Al4V porosity graded gyroids for bone implants. *International Journal of Mechanical Sciences 193 (2021) 106180.*

[37] B. Blakey-Milner, P. Gradl, G. Snedden, M. Brooks, J. Pitot, E. Lopez, M. Leary, F. Berto, A. du Plessis. Metal additive manufacturing in aerospace: A review. *Materials & Design 209 (2021) 110008.*

[38] T.S. Srivatsan, T.S. Sudarshan. Additive Manufacturing: Innovations, Aadvances, and Applications. CRC Press, 2015.

[39] A. Gebhardt, J.-S. Hötter. Additive Manufacturing: 3D Printing for Prototyping and Mmanufacturing. Carl Hanser Verlag GmbH Co KG, 2016.

[40] W.E. Frazier. Metal additive manufacturing: a review. *Journal of Materials Engineering and performance 23, 6 (2014) 1917–1928.*

[41] A. Bandyopadhyay, K.D. Traxel, M. Lang, M. Juhasz, N. Eliaz, S. Bose. Alloy design via additive manufacturing: Advantages, challenges, applications and perspectives. *Materials Today (2022).*

[42] D. Gu. Laser Additive Manufacturing of High-Performance Materials. Springer, 2015.

[43] I. Yadroitsev, I. Yadroitsava, A. Du Plessis, E. MacDonald. Fundamentals of Laser Powder Bed Fusion of Metals. Elsevier, 2021.

[44] D. Buchbinder, H. Schleifenbaum, S. Heidrich, W. Meiners, J. Bültmann. High power selective laser melting (HP SLM) of aluminum parts. *Physics Procedia 12 (2011) 271-278.*

[45] R. Li, J. Liu, Y. Shi, M. Du, Z. Xie. 316L Stainless Steel with Gradient Porosity Fabricated by Selective Laser Melting. *Journal of Materials Engineering and Performance 19(5) (2009) 666–671.*

[46] R. Li, J. Liu, Y. Shi, L. Wang, W. Jiang. Balling behavior of stainless steel and nickel powder during selective laser melting process. *The International Journal of Advanced Manufacturing Technology 59 (2011) 1025–1035.*

[47] Y. Guo, L. Jia, B. Kong, N. Wang, H. Zhang. Single track and single layer formation in selective laser melting of niobium solid solution alloy. *Chinese Journal of Aeronautics 31(4) (2018) 860–866.*

[48] J. Lee, J. Choe, J. Park, J.-H. Yu, S. Kim, I.D. Jung, H. Sung. Microstructural effects on the tensile and fracture behavior of selective laser melted H13 tool steel under varying conditions. *Materials Characterization 155 (2019) 109817.*

[49] N. Ahmed, I. Barsoum, G. Haidemenopoulos, R.K.A. Al-Rub. Process parameter selection and optimization of laser powder bed fusion for 316L stainless steel: A review. *Journal of Manufacturing Processes 75 (2022) 415–434.*

[50] Y.H. Zhou, W.P. Li, L. Zhang, S.Y. Zhou, X. Jia, D.W. Wang, M. Yan. Selective laser melting of Ti–22Al–25Nb intermetallic: Significant effects of hatch distance on microstructural features and mechanical properties. *Journal of Materials Processing Technology 276 (2020).*

[51] K. Kempen, E. Yasa, L. Thijs, J.P. Kruth, J. Van Humbeeck. Microstructure and mechanical properties of Selective Laser Melted 18Ni-300 steel. *Physics Procedia 12 (2011) 255–263.*

[52] J. Sun, Y. Yang, D. Wang. Parametric optimization of selective laser melting for forming Ti6Al4V samples by Taguchi method. *Optics & Laser Technology 49 (2013) 118–124.*

[53] V.S. Sufiiarov, A.A. Popovich, E.V. Borisov, I.A. Polozov, D.V. Masaylo, A.V. Orlov. The effect of layer thickness at selective laser melting. *Procedia Engineering 174 (2017) 126–134.*

[54] T. DebRoy, H.L. Wei, J.S. Zuback, T. Mukherjee, J.W. Elmer, J.O. Milewski, A.M. Beese, A. Wilson-Heid, A. De, W. Zhang. Additive manufacturing of

metallic components – process, structure and properties. *Progress in Materials Science 92 (2018) 112–224.*

[55] J. Dawes, R. Bowerman, R. Trepleton. Introduction to the additive manufacturing powder metallurgy supply chain. *Johnson Matthey Technology Review 59(3) (2015) 243-256.*

[56] S.D. Dobson, T.L. Starr. Powder characterization and part density for powder bed fusion of 17-4 PH stainless steel. *Rapid Prototyping Journal 27(1) (2021) 53–58.*

[57] S. Diener, A. Zocca, J. Günster. Literature review: Methods for achieving high powder bed densities in ceramic powder bed based additive manufacturing. *Open Ceramics 8 (2021) 100191.*

[58] T. Delacroix, F. Lomello, F. Schuster, H. Maskrot, J.-P. Garandet. Influence of powder recycling on 316L stainless steel feedstocks and printed parts in laser powder bed fusion. *Additive Manufacturing 50 (2022) 102553.*

[59] P. Avrampos, G.-C. Vosniakos. A review of powder deposition in additive manufacturing by powder bed fusion. *Journal of Manufacturing Processes 74 (2022) 332–352.*

[60] A.B. Spiering , N. Herres , G. Levy. Influence of the particle size distribution on surface quality and mechanical properties in AM steel parts. *Rapid Prototyping Journal 17(3) (2011) 195–202.*

[61] S.E. Brika, M. Letenneur, C.A. Dion, V. Brailovski. Influence of particle morphology and size distribution on the powder flowability and laser powder bed fusion manufacturability of Ti-6Al-4V alloy. *Additive Manufacturing 31 (2020) 100929.*

[62] W.E. King, A.T. Anderson, R.M. Ferencz, N.E. Hodge, C. Kamath, S.A. Khairallah, A.M. Rubenchik. Laser powder bed fusion additive manufacturing of metals; physics, computational, and materials challenges. *Applied Physics Reviews 2(4) (2015) 041304.*

[63] N.P. Karapatis, G. Egger, P.-E. Gygax, R. Glardon. Optimization of powder layer density in selective laser sintering. *Proceedings of the 9th Annual International Solid Freeform Fabrication Symposium. Austin, Texas, 1999, pp. 255–263.*

[64] A.B. Spierings, G. Levy. Comparison of density of stainless steel 316L parts produced with selective laser melting using different powder grades. *Proceedings of the SFF Symposium. Austin, Texas, 2009, pp. 1–12.*

[65] Y. Lu, S. Wu, Y. Gan, T. Huang, C. Yang, L. Junjie, J. Lin. Study on the microstructure, mechanical property and residual stress of SLM Inconel-718 alloy manufactured by differing island scanning strategy. *Optics & Laser Technology 75 (2015) 197–206.*

[66] J. Jhabvala, E. Boillat, T. Antignac, R. Glardon. On the effect of scanning strategies in the selective laser melting process. *Virtual and Physical Prototyping 5(2) (2010) 99–109.*

[67] M. Guo, Y. Ye, X. Jiang, L. Wang, Microstructure. Mechanical Properties and Residual Stress of Selective Laser Melted AlSi10Mg. *Journal of Materials Engineering and Performance 28(11) (2019) 6753–6760.*

[68] L. Thijs, K. Kempen, J.-P. Kruth, J. Van Humbeeck. Fine-structured aluminium products with controllable texture by selective laser melting of pre-alloyed AlSi10Mg powder. *Acta Materialia 61(5) (2013) 1809–1819.*

[69] L.N. Carter, C. Martin, P.J. Withers, M.M. Attallah. The influence of the laser scan strategy on grain structure and cracking behaviour in SLM powder-bed fabricated nickel superalloy. *Journal of Alloys and Compounds 615 (2014) 338–347.*

[70] Y. Tian, D. Tomus, P. Rometsch, X. Wu. Influences of processing parameters on surface roughness of Hastelloy X produced by selective laser melting. *Additive Manufacturing 13 (2017) 103–112.*

[71] Y.M. Arısoy, L.E. Criales, T. Özel, B. Lane, S. Moylan, A. Donmez. Influence of scan strategy and process parameters on microstructure and its optimization in additively manufactured nickel alloy 625 via laser powder bed fusion. *The International Journal of Advanced Manufacturing Technology 90(5-8) (2016) 1393–1417.*

[72] B. AlMangour, D. Grzesiak, J.-M. Yang. Scanning strategies for texture and anisotropy tailoring during selective laser melting of TiC/316L stainless steel nanocomposites. *Journal of Alloys and Compounds 728 (2017) 424–435.*

[73] S. Li, Q. Wei, Y. Shi, Z. Zhu, D. Zhang. Microstructure characteristics of Inconel 625 superalloy manufactured by selective laser melting. *Journal of Materials Science & Technology 31(9) (2015) 946–952.*

[74] T. Özel, Y.M. Arısoy, L.E. Criales. Computational simulation of thermal and spattering phenomena and microstructure in selective laser melting of Inconel 625. *Physics Procedia 83 (2016) 1435–1443.*

[75] L.E. Criales, Y.M. Arısoy, B. Lane, S. Moylan, A. Donmez, T. Özel. Laser powder bed fusion of nickel alloy 625: Experimental investigations of effects of process parameters on melt pool size and shape with spatter analysis. *International Journal of Machine Tools and Manufacture 121 (2017) 22–36.*

[76] J.R. Poulin, V. Brailovski, P. Terriault. Long fatigue crack propagation behavior of Inconel 625 processed by laser powder bed fusion: Influence of build orientation and post-processing conditions. *International Journal of Fatigue 116 (2018) 634–647.*

[77] C. Pleass, S. Jothi. Influence of powder characteristics and additive manufacturing process parameters on the microstructure and mechanical behaviour of Inconel 625 fabricated by selective laser melting. *Additive Manufacturing 24 (2018) 419-431.*

[78] H.L.-H. Pavan Bhavsar, Rajesh K. Ananda-Kumar, Viswanathan Madhavan, Wilfredo Moscoso-Kingsley. Adiabatic shear banding behavior of additively manufactured superalloy IN 625. *Procedia Manufacturing 34 (2019) 722-730.*

[79] G. Marchese, M. Lorusso, S. Parizia, E. Bassini, J.-W. Lee, F. Calignano, D. Manfredi, M. Terner, H.-U. Hong, D. Ugues, M. Lombardi, S. Biamino. Influence of heat treatments on microstructure evolution and mechanical properties of Inconel 625 processed by laser powder bed fusion. *Materials Science and Engineering: A 729 (2018) 64–75.*

[80] G. Marchese, S. Parizia, M. Rashidi, A. Saboori, D. Manfredi, D. Ugues, M. Lombardi, E. Hryha, S. Biamino. The role of texturing and microstructure evolution on the tensile behavior of heat-treated Inconel 625 produced via laser powder bed fusion. *Materials Science and Engineering: A 769 (2020).*

[81] S. Parizia, G. Marchese, M. Rashidi, M. Lorusso, E. Hryha, D. Manfredi, S. Biamino. Effect of heat treatment on microstructure and oxidation properties of Inconel 625 processed by LPBF. *Journal of Alloys and Compounds 846 (2020).*

[82] U. Ali, H. Fayazfar, F. Ahmed, E. Toyserkani. Internal surface roughness enhancement of parts made by laser powder-bed fusion additive manufacturing. *Vacuum 177 (2020).*

[83] Y. Sun, L. Chen, L. Li, X. Ren. High-temperature oxidation behavior and mechanism of Inconel 625 super-alloy fabricated by selective laser melting. *Optics & Laser Technology 132 (2020).*

[84] S. Qin, T.C. Novak, M.K. Vailhe, Z.-K. Liu, A.M. Beese. Plasticity and fracture behavior of Inconel 625 manufactured by laser powder bed fusion: Comparison between as-built and stress relieved conditions. *Materials Science and Engineering: A 806 (2021).*

[85] S.A. Khairallah, A.T. Anderson, A. Rubenchik, W.E. King. Laser powder-bed fusion additive manufacturing: Physics of complex melt flow and formation mechanisms of pores, spatter, and denudation zones. *Acta Materialia 108 (2016) 36–45.*

[86] K.C. Mills, E.D. Hondros, M. McLean, K.C. Mills, B.J. Keene, R.F. Brooks, A. Shirali. Marangoni effects in welding. *Philosophical Transactions of the Royal Society of London. Series A: Mathematical, Physical and Engineering Sciences 356(1739) (1998) 911–925.*

[87] Y.L. Xu, Z.B. Dong, Y.H. Wei, C.L. Yang. Marangoni convection and weld shape variation in A-TIG welding process. *Theoretical and Applied Fracture Mechanics 48(2) (2007) 178–186.*

[88] M. Xia, D. Gu, G. Yu, D. Dai, H. Chen, Q. Shi. Porosity evolution and its thermodynamic mechanism of randomly packed powder-bed during selective laser melting of Inconel 718 alloy. *International Journal of Machine Tools and Manufacture 116 (2017) 96–06.*

[89] Z. Chen, Y. Xiang, Z. Wei, P. Wei, B. Lu, L. Zhang, J. Du. Thermal dynamic behavior during selective laser melting of K418 superalloy: numerical simulation and experimental verification. *Applied Physics A 124(4) (2018) 313.*

[90] W.E. King, H.D. Barth, V.M. Castillo, G.F. Gallegos, J.W. Gibbs, D.E. Hahn, C. Kamath, A.M. Rubenchik. Observation of keyhole-mode laser melting in laser powder-bed fusion additive manufacturing. *Journal of Materials Processing Technology 214(12) (2014) 2915–2925.*

[91] W. Xu, Direct additive manufacturing techniques for metal parts: SLM, EBM, laser metal deposition. *Encyclopedia of Materials: Metals and Alloys, 2022, pp. 290–318.*

[92] Y. Liu, Y. Yang, S. Mai, D. Wang, C. Song. Investigation into spatter behavior during selective laser melting of AISI 316L stainless steel powder. *Materials & Design 87 (2015) 797–806.*

[93] H. Gong, K. Rafi, H. Gu, T. Starr, B. Stucker, Analysis of defect generation in Ti–6Al–4V parts made using powder bed fusion additive manufacturing processes, *Additive Manufacturing 1-4 (2014) 87–98.*

[94] J. Han, J. Yang, H. Yu, J. Yin, M. Gao, Z. Wang, X. Zeng. Microstructure and mechanical property of selective laser melted Ti6Al4V dependence on laser energy density. *Rapid Prototyping Journal 23(2) (2017) 217–226.*

[95] R.C. Reed. The Superalloys: Fundamentals and Applications. *Cambridge University Press, 2008.*

[96] B. Geddes, H. Leon, X. Huang. Superalloys: Alloying and Performance.*ASM International, 2010.*

[97] X. Wang, L.N. Carter, B. Pang, M.M. Attallah, M.H. Loretto. Microstructure and yield strength of SLM-fabricated CM247LC Ni-Superalloy. *Acta Materialia 128 (2017) 87–95.*

[98] S. Pratheesh Kumar, S. Elangovan, R. Mohanraj, J.R. Ramakrishna. A review on properties of Inconel 625 and Inconel 718 fabricated using direct energy deposition. *Materials Today: Proceedings 46 (2021) 7892–7906.*

[99] F. Zhang, L.E. Levine, A.J. Allen, M.R. Stoudt, G. Lindwall, E.A. Lass, M.E. Williams, Y. Idell, C.E. Campbell. Effect of heat treatment on the microstructural evolution of a nickel-based superalloy additive-manufactured by laser powder bed fusion. *Acta Materialia 152 (2018) 200–214.*

[100] A. Kreitcberg, V. Brailovski, S. Turenne. Elevated temperature mechanical behavior of IN625 alloy processed by laser powder-bed fusion, Materials Science and Engineering: A 700 (2017) 540–553.

[101] J.W.D. Callister, D.G. Rethwisch. Materials Science and Engineering – An Introduction. 9th Edition, John Wiley & Sons, 2013.

[102] R. Abbaschian, R. Abbaschian, R.E. Reed-Hill. Physical Metallurgy Principles. 4th Edition, Cengage Learning, 2009.

[103] M.Z. Ghodsi, S. Khademzadeh, E. Marzbanrad, M.H. Razmpoosh, N. De Marchi, E. Toyserkani. Development of Yttria-stabilized zirconia reinforced Inconel 625 metal matrix composite by laser powder bed fusion. *Materials Science and Engineering: A 827 (2021) 142037.*

[104] B. Zhang, G. Bi, S. Nai, C.-n. Sun, J. Wei. Microhardness and microstructure evolution of TiB2 reinforced Inconel 625/TiB2 composite produced by selective laser melting. *Optics & Laser Technology 80 (2016) 186–195.*

[105] C. Li, R. White, X.Y. Fang, M. Weaver, Y.B. Guo. Microstructure evolution characteristics of Inconel 625 alloy from selective laser melting to heat treatment. *Materials Science and Engineering: A 705 (2017) 20–31.*

[106] H. Wong, K. Dawson, G.A. Ravi, L. Howlett, R.O. Jones, C.J. Sutcliffe. Multi-laser powder bed fusion benchmarking—Initial trials with Inconel 625. *The International Journal of Advanced Manufacturing Technology 105 (7-8) (2019) 2891–2906.*

[107] J. Nguejio, F. Szmytka, S. Hallais, A. Tanguy, S. Nardone, M. Godino Martinez. Comparison of microstructure features and mechanical properties for additive manufactured and wrought nickel alloys 625. *Materials Science and Engineering: A 764 (2019) 138214.*

[108] X. Yan, S. Gao, C. Chang, J. Huang, K. Khanlari, D. Dong, W. Ma, N. Fenineche, H. Liao, M. Liu. Effect of building directions on the surface roughness, microstructure, and tribological properties of selective laser melted Inconel 625. *Journal of Materials Processing Technology 288 (2021) 116878.*

[109] A.B. Spierings, M. Schneider, R. Eggenberger. Comparison of density measurement techniques for additive manufactured metallic parts. *Rapid Prototyping Journal 17(5) (2011) 380–386.*

[110] ASTM Standard. ASTM E384–11: Standard Test Method for Knoop and Vickers Hardness of Materials, ASTM International, West Conshohocken, USA, 2011. ASTM, USA, 2011.

[111] M. Balbaa, S. Mekhiel, M. Elbestawi, J. McIsaac. On selective laser melting of Inconel 718: Densification, surface roughness, and residual stresses. *Materials & Design 193 (2020) 108818.*

[112] A.F. de Souza, K.S. Al-Rubaie, S. Marques, B. Zluhan, E.C. Santos. Effect of laser speed, layer thickness, and part position on the mechanical properties of maraging 300 parts manufactured by selective laser melting. *Materials Science and Engineering: A 767 (2019) 138425.*

[113] R. Cunningham, C. Zhao, N. Parab, C. Kantzos, J. Pauza, K. Fezzaa, T. Sun, A.D. Rollett. Keyhole threshold and morphology in laser melting revealed by ultrahigh-speed x-ray imaging. *Science 363 (2019) 849–852.*

[114] D. Bates, D. Watts. Nonlinear Regression Analysis and its Applications. John Wiley & Sons, Inc., 1988.

[115] R.R. Rhinehart. Nonlinear Regression Modeling for Engineering Applications: Modeling, Model Validation, and Enabling Design of Experiments. Wiley-ASME Press, 2016.

[116] K. Kempen. Expanding the Materials Palette for Selective Laser Melting of Metals. PhD Thesis, University of Leuven, 2015.

[117] N.N.R. Ranga Suri, Narasimha Murty M, G. Athithan. Outlier Detection: Techniques and Applications, A Data Mining Perspective. Springer Nature Switzerland AG, 2019.

[118] X.Y. Fang, H.Q. Li, M. Wang, C. Li, Y.B. Guo. Characterization of texture and grain boundary character distributions of selective laser melted Inconel 625 alloy. *Materials Characterization 143 (2018) 182–190.*